

Detection of Anomalies in Texture Images
Using Multi-Resolution Features

Lior Shadhan

Detection of Anomalies in Texture Images Using Multi-Resolution Features

Research Thesis

Submitted in Partial Fulfillment of the Requirements
For the Degree of Master of Science
in Electrical Engineering

Lior Shadhan

Submitted to the Senate of the Technion — Israel Institute of Technology

SHEBAT 5767

HAIFA

JANUARY 2007

The Research Thesis Was Done Under The Supervision of Prof. Israel Cohen in the
Electrical Engineering Department

Acknowledgment

I wish to express my gratitude to my advisor, Prof. Israel Cohen, for his devoted supervision and his professional guidance throughout the research.

I would like to thank the examiners of this thesis, Dr. Moshe Porat and Prof. Amir Averbuch, for their constructive comments and helpful suggestions.

I would also like to thank my colleagues at Elbit System Ltd. for their patience and support.

Special thanks to my family and to my beloved Keren for their ongoing encouragement throughout the research.

The generous financial help of The Technion is gratefully acknowledged

Contents

Abstract	1
List of Symbols and Abbreviations	3
1 Introduction	13
1.1 Motivation and Goals	13
1.2 Overview of the Thesis	16
1.3 Organization	18
2 Background	21
2.1 Introduction	21
2.2 Texture Modeling	22
2.2.1 The Non-Casual GMRF Model	22
2.2.2 The GSM Statistical Model	25
2.3 Texture Segmentation and Classification	27
2.3.1 Texture Classification	27
2.3.2 Unsupervised Texture Segmentation	29
2.4 Anomaly Detection	30
2.4.1 Single Hypothesis Test	31

2.4.2	Matched Subspace Detection	33
2.4.3	Overview of Algorithms	36
2.5	Summary	40
3	Anomaly Detection Using MR Gaussian Textural Features	41
3.1	Introduction	41
3.2	Problem Formulation - Detached Anomaly	42
3.3	Anomaly Detection Algorithm	43
3.4	Anomaly Detection Experimental Results	47
3.4.1	Performance Analysis	47
3.4.2	Anomaly Detection Examples	48
3.5	Application to Texture Classification	53
3.6	Texture Classification Experimental Results	53
3.7	Enhancement of Detection	55
3.8	Summary	58
4	Anomaly Subspace Detection Using MR Textural Features	61
4.1	Introduction	61
4.2	Problem Formulation - Additive Anomaly	64
4.3	Statistical Model Formulation	65
4.3.1	Segregation Enhancement	65
4.3.2	Single Layer 2-D Random Field Model	67
4.3.3	Multi-Resolution Feature Space	71
4.4	Anomaly Detection Algorithm	73
4.5	Anomaly Detection Experimental Results	82
4.5.1	Performance Analysis	83

4.5.2	Anomaly Detection Examples	93
4.6	Image Scaling for Reduced Prediction Error	94
4.7	SNR Criterion for Improved Performance	96
4.8	Summary	98
5	Conclusion	99
5.1	Summary	99
5.2	Future Research	100
	References	102

List of Figures

1.1	A comparison between detection methods. (a) Background natural texture of a stone. (b) Same texture but with an additive squared shaped synthetic anomaly in its center. The synthetic anomaly was created using image chips taken from a texture of metal, not having evident visual resemblance to the stone texture. The anomaly was scaled to achieve $\text{SNR} = 30[\text{dB}]$. Anomaly detection results using various methods: (c) Proposed algorithm (Chapter 4). (d) Goldman and Cohen [22]. (e) Proposed algorithm (Chapter 3). (f) Mittelman and Porat segmentation algorithm [35]. The white target mark is attached only to the highest value in each detection image.	20
2.1	MSD performance. Detection rate vs. SNR for various values of the target subspace rank r . Performance is given at false alarm rate of 10^{-4} .	36
3.1	Block diagram of the proposed anomaly detection algorithm.	44
3.2	Mahalanobis distance calculation using a background clutter image and an anomaly image, both Brodatz like, for various values of M	48

3.3	Calculated ROC curves using various values of M for: (a) Background and anomaly textures with no evident visual resemblance, presented in Figure 3.4. (b) Background and anomaly textures with evident visual resemblance, presented in Figure 3.5.	49
3.4	Background and anomaly textures with no evident visual resemblance. (a) Background texture. (b) Texture for anomaly. (c) Typical texture with anomaly. The anomaly is placed at the center of the background texture.	50
3.5	Background and anomaly textures with evident visual resemblance. (a) Background texture. (b) Texture for anomaly. (c) Typical texture with anomaly. The anomaly is placed at the center of the background texture.	50
3.6	Mahalanobis distance under hypothesis H_1 for various values of the averaging window dimension M . The anomaly size is 15×15 pixels. .	51
3.7	Anomaly detection examples. (a) Synthesized image with anomaly in its center, using textures not having evident visual resemblance. (b) Synthesized image with anomaly in its center, using textures having evident visual resemblance. (c) Real sonar image containing a sea-mine. (d)-(f) Corresponding detection results using $m = 10$, $N = 3$, $M = 15$. The white target mark is attached only to the highest value in each detection image.	52
3.8	Block diagram of the proposed texture classification algorithm.	54

3.9	Mahalanobis distance calculation using a background clutter image and an anomaly image. The anomaly image is a scaled version of the background image with a scale factor of $\delta = 2$. (a) Without normalization; The scaled background image is regarded as an anomaly. (b) With normalization; The scaled background image is not regarded as an anomaly. Calculation was preformed using $m = 10$, $N = 3$, $M = 15$.	57
3.10	The Brodatz like textures that were used in our experiments.	59
4.1	Innovations covariance example. GMRF (left column) vs. actual (right column). (a-b) Derived directly from the background texture. (c-d) Derived from a layer of wavelet coefficients. (e-f) Derived from the same layer of wavelet coefficients after applying the squaring non-linearity.	69
4.2	Block diagram of the proposed anomaly detection algorithm.	74
4.3	Image chips used for the target subspace. Each chip has 16×16 pixels.	84
4.4	ROC curves of the proposed algorithm for various values of p - number of layers after KLT, averaged over a set of 40 Brodatz like textures. Results are given for various SNR values: (a) 16[dB]. (b) 18[dB]. (c) 20[dB].	86
4.5	GLR non-centrality parameter vs. the sum of RDWT layers SNR values, given for hypothesis H_1 . Results are averaged over a set of 40 Brodatz like textures.	88
4.6	MSD performance. Proposed algorithm vs. competing algorithm [22] and theoretical results with equal target subspace dimensionality, averaged over a set of 40 Brodatz like textures. Results are given for various false alarm values: (a) 10^{-2} . (b) 10^{-3} . (c) 10^{-4}	90

4.7	ROC curves of the proposed algorithm vs. competing algorithms [22, 55], averaged over a set of 40 Brodatz like textures. Results are given for various SNR values: (a) 16[dB]. (b) 18[dB]. (c) 20[dB].	91
4.8	An example of detection improvement in low SNER environment using a background natural texture of a stone with an additive squared shaped synthetic anomaly in its center. The synthetic anomaly was created using image chips taken from a texture of metal, not having evident visual resemblance to the stone texture. The anomaly was scaled to achieve: (a) SNR = 24[dB]. (b) SNR = 30[dB]. Corresponding anomaly detection results using various methods: (c-d) Proposed algorithm (Section 4). (e-f) Goldman and Cohen [22]. In both methods the detection was performed using a target subspace which was created from the same image chips that were used for synthesizing the anomaly. The white target mark is attached only to the highest value in each detection image.	92
4.9	GLR distribution example using the stone texture from Figure 1.1-(a).	93
4.10	Side scan sonar images [2, 3] and corresponding anomaly detection results. (a) Cessna airplane. (b) Small boat. (c) The "Isaac M. Scott" freighter. (d) Tree trunk. (e)-(h) Corresponding detection results. The white target mark is attached only to the highest value in each GLR image.	95
4.11	Image chips used for the target subspace in the sonar detection examples. Each chip has 16×16 pixels.	96

List of Tables

3.1	Comparison of texture classification results	55
-----	--	----

Abstract

Anomaly target detection is the process of locating elements in a scene which are unlikely to be a part of it. This is a challenging problem, mainly due to the large variability of the scene's background clutter and the appearance of the anomalous elements. The detection process is generally performed with respect to a predefined probabilistic model and an appropriate feature space, in which a clear segregation between the anomalous elements and the rest of the background clutter in the scene is possible. Anomaly detectors often use Bayesian classifiers, utilizing available knowledge of *a priori* and *a posteriori* statistics of both background clutter and anomalous targets. Texture segmentation is the process of segmenting different textures in a scene based on a texture classification scheme. Texture classification is generally performed with respect to a characterizing feature space and a distance measure between textures. Since images of the same underlying texture can vary significantly, textural features must be invariant to image variations and at the same time sensitive to intrinsic spatial structures that define textures. Furthermore, the distance measure must be robust to these variations in order to avoid classification errors. As a result, texture segmentation algorithms perform poorly when used for the purpose of detecting anomalous targets in a given scene.

In this work, we integrate texture classification features with properly formulated anomaly detection classifiers, achieving improved performance in both realms. We introduce a multi-resolution feature space which follows the Gaussian distribution and corresponding algorithms for anomaly detection and texture classification. The proposed feature space is based on a multi-resolution representation of the image, obtained using the redundant discrete wavelet transform (RDWT), followed by estimation of Gaussian Scale Mixture (GSM) hidden multipliers and certain non-linearities which were reported to improve texture classification performance. Detection and classification are then performed using a single hypothesis test classifier. In addition, we introduce a multi-resolution random field model (RFM) and a corresponding anomaly subspace detection algorithm designated to detect additive anomalies in harsh environments where signal to noise energy ratio values are very small. The proposed model is based on a multi-resolution representation of the image, obtained using the RDWT, followed by a squaring non-linearity. Each layer is modeled as an RFM with different sets of parameters. Detection is then performed using a matched subspace detector (MSD) classifier. The MSD is formulated for detecting subspace signals in RFM innovations of the background clutter, taking into consideration the introduced squaring non-linearity. The proposed algorithms are shown to have improved performance compared to those reported recently in the literature. The results demonstrate the robustness and flexibility of the algorithms in adverse environments.

List of Symbols and Abbreviations

Symbols:

General Symbols

$E[\cdot]$	Expectancy
H_0	Hypothesis which indicates the absence of a target signal
H_1	Hypothesis which indicates the presence of a target signal
\mathbf{I}	The identity matrix
$P(\cdot)$	pdf
$P(\cdot \cdot)$	Conditional pdf
P_D	Probability of detection - detection rate
P_{FA}	Probability of false-alarms - false alarm rate
\mathbb{R}	Set of reals
$\ell^2(\mathbb{Z})$	ℓ^2 space
$1 - \epsilon_1$	Lower bound for P_D
ϵ_2	Upper bound for P_{FA}
$\chi_a^2(b)$	Chi-square distribution with a degrees of freedom and non-centrality parameter b
$\mathbf{0}$	A vector of zeros
$\widehat{(\cdot)}$	Estimate

$(\cdot)^T$	Transpose
$[\cdot]_i$	The vector element in the i th row
$[\cdot]_{i,j}$	The matrix element in the i th row and the j th column
$\text{col}[\cdot]$	Column stack representation
$ \cdot $	Number of elements in group
$\ \cdot\ ^2$	Squared l^2 norm

Chapter 2 Symbols

$\mathcal{H}_1, \mathcal{H}_2$	Histograms of marginal distributions
\mathcal{R}	Set of indices representing the neighborhood of a pixel
$\mathbf{B}(\boldsymbol{\theta})$	The GMRF resulting block-circulant matrix
L	GLR
d	Mahalanobis distance
$\mathbf{r} = (r_1, r_2)$	Indices in \mathcal{R}
$\mathbf{v} = (v_1, v_2)$	Indices of a pixel in an image with support Ω
$\mathbf{w}(\mathbf{v})$	Observation of an image in the neighbor set \mathcal{R} around pixel \mathbf{v}
\mathbf{y}	Column stack representations of $y(\mathbf{v})$
$y(\mathbf{v})$	Stationary image with zero mean
z	GSM hidden multiplier
Ω	Support lattice, $M \times M$
$\boldsymbol{\varepsilon}$	Column stack representations of $\varepsilon(\mathbf{v})$
$\varepsilon(\mathbf{v})$	GMRF innovations
$\boldsymbol{\theta}$	Column stack representation of $\theta(\mathbf{r})$
$\theta(\mathbf{r})$	Weight coefficient of a neighbor $\mathbf{r} \in \mathcal{R}$
ρ^2	GMRF innovations variance

$\chi^2(\mathcal{H}_1, \mathcal{H}_2)$ χ^2 statistic between spectral histograms

Chapter 3 Symbols

\mathcal{R}_1	A set of indices representing the $N \times N$ local neighborhood of a pixel
\mathcal{R}_2	A set of indices representing the $M \times M$ local neighborhood of a pixel
$d(\mathbf{s})$	Mahalanobis distance
$n(\mathbf{s})$	Anomalous target signal
$\mathbf{q}(\mathbf{s})$	Normalized multi-resolution feature space vector
$\mathbf{s} = (s_1, s_2)$	Indices of a pixel in an image with support Ω
$t_j(\mathbf{s})$	The logarithm of the GSM hidden multipliers MLE
$\mathbf{v}(\mathbf{s})$	Multi-resolution feature space vector
$v_j(\mathbf{s})$	The j th layer of the feature space
$x(\mathbf{s})$	Background natural texture
$y(\mathbf{s})$	Observations of an image
$\{y_j(\mathbf{s})\}_{j=1, \dots, m}$	Multi-resolution decomposition of image $y(\mathbf{s})$ with m layers of decomposition
$\mathbf{z}(\mathbf{s})$	Whitened multi-resolution feature space vector
Ω	Support lattice
δ	Scaling factor
η	Decision rule threshold
λ	Non-centrality parameter
μ_0, Σ_0	Feature space statistics of the background image
μ_1, Σ_1	Feature space statistics of the anomalous target signal

Chapter 4 Symbols

$\langle \mathcal{A}_k \rangle$	The k th layer interference subspace
$\langle \mathcal{B}_k \rangle$	The k th layer target subspace
\mathcal{D}_k	Same as $\mathbf{B}(\theta_k(\mathbf{r}))$
\mathcal{R}	A set of indices representing the neighborhood of the RFM field
\mathcal{R}_z	Averaging Window
$\mathbf{B}(\boldsymbol{\theta})$	The RFM resulting block-circulant matrix
$\mathbf{B}(\theta_k(\mathbf{r}))$	The k th layer RFM resulting block-circulant matrix
\mathbf{K}	KLT matrix
$L(\mathbf{v})$	GLR
$L_k(\mathbf{v})$	GLR of the k th layer
$\mathbf{P}_{\mathcal{A}_k}, \mathbf{P}_{\mathcal{A}_k\mathcal{B}_k}$	Subspace projection operators
$\mathbf{P}_{\mathcal{A}_k}^\perp, \mathbf{P}_{\mathcal{A}_k\mathcal{B}_k}^\perp$	Subspace projection operators to the orthogonal complement subspace
$\text{SNR}(k, \mathbf{v})$	The MSD's k th layer SNR
$g(\mathbf{v})$	Additive interfering signal
$g(\mathbf{v}, \mathbf{s})$	Additive interfering signal chip
$\mathbf{g}(\mathbf{v}, \mathbf{s})$	Multi-resolution image chip decomposition of the interfering signal $g(\mathbf{v}, \mathbf{s})$
$\{g^{(l)}(\mathbf{s})\}_{l=1, \dots, u_g}$	Set of orthogonal image chips which span the interfering signals
$\mathbf{g}^{(l)}(\mathbf{s})$	Multi-resolution chip decomposition of $g^{(l)}(\mathbf{s})$
$h(\mathbf{v})$	Additive target signal
$h(\mathbf{v}, \mathbf{s})$	Additive target signal chip

$\mathbf{h}(\mathbf{v})$	The column stack representation of the target chip $h(\mathbf{v}, \mathbf{s})$
$\mathbf{h}(\mathbf{v}, \mathbf{s})$	Multi-resolution image chip decomposition of the target signal $h(\mathbf{v}, \mathbf{s})$
$\{h^{(l)}(\mathbf{s})\}_{l=1, \dots, u_h}$	Set of orthogonal image chips which span the target signals
$\mathbf{h}^{(l)}(\mathbf{s})$	Multi-resolution chip decomposition of $h^{(l)}(\mathbf{s})$
m	Number of multi-resolution layers
$\mathbf{n}_k(\mathbf{v})$	The column stack representation of the chip's k th layer RFM innovations
p	Number of layers after KLT
q	MSD dimensionality
$\mathbf{r} = (r_1, r_2)$	Indices in \mathcal{R}
$\mathbf{s} = (s_1, s_2)$	Indices of a pixel in an image chip with support Ω_0
$\mathbf{t}(\mathbf{v})$	p principle components, derived using the KLT
$\mathbf{t}(\mathbf{x}(\mathbf{v}, \mathbf{s}))$	Principle components of $\mathbf{x}(\mathbf{v}, \mathbf{s})$
$\mathbf{t}(\mathbf{g}(\mathbf{v}, \mathbf{s}))$	Principle components of $\mathbf{g}(\mathbf{v}, \mathbf{s})$
$\mathbf{t}(\mathbf{h}(\mathbf{v}, \mathbf{s}))$	Principle components of $\mathbf{h}(\mathbf{v}, \mathbf{s})$
$t_k(\mathbf{v})$	Principle component, derived using the KLT
u_h	Number of image chips which span the target subspace
u_g	Number of image chips which span the interference subspace
u_x	Number of image chips which span the background subspace
$\mathbf{v} = (v_1, v_2)$	Indices of a pixel in an image with support Ω
$\mathbf{w}(\mathbf{v})$	Observation of an image in the neighbor set \mathcal{R} around pixel \mathbf{v}
$x(\mathbf{v})$	Background natural texture
$x(\mathbf{v}, \mathbf{s})$	Background natural texture chip
$\mathbf{x}(\mathbf{v})$	The column stack representation of the background chip $x(\mathbf{v}, \mathbf{s})$

$\mathbf{x}(\mathbf{v}, \mathbf{s})$	Multi-resolution image chip decomposition of the background clutter $x(\mathbf{v}, \mathbf{s})$
$\left\{x_j^{(l)}(\mathbf{s})\right\}_{l=1, \dots, u_x}$	Set of image chips which characterize the j th layer of the background natural texture multi-resolution decomposition
$\mathbf{x}^{(l)}(\mathbf{s})$	All layers of $x_j^{(l)}(\mathbf{s})$
$y(\mathbf{v})$	Observations of an image
\mathbf{y}	Column stack representation of $y(\mathbf{v})$
$\mathbf{y}(\mathbf{v})$	Multi-resolution decomposition of image $y(\mathbf{v})$ with m layers of decomposition
$y(\mathbf{v}, \mathbf{s})$	Observations of an image chip
$\mathbf{y}(\mathbf{v}, \mathbf{s})$	Multi-resolution image chip decomposition of $y(\mathbf{v}, \mathbf{s})$
$y_j(\mathbf{v})$	RDWT layer of image $y(\mathbf{v})$
$\mathbf{z}(\mathbf{v})$	Local energy measures
$z_k(\mathbf{v})$	Local energy measures in the k th layer
$z_k(\mathbf{v}, \mathbf{s})$	The chip's k th layer local energy measures
$\mathbf{z}_k(\mathbf{v})$	The column stack representation of $z_k(\mathbf{v}, \mathbf{s})$
Γ	The background clutter covariance of a background image chip
$\Theta(\mathbf{r})$	A diagonal matrix with the weight coefficients of all layers
Λ	Innovations covariance
Λ_k	The covariance of $\mathbf{n}_k(\mathbf{v})$
Σ	Image covariance
Ω	Support lattice, $M \times M$
Ω_0	Support lattice for image chip, $N \times N$
$\gamma_k(\mathbf{v})$	The whitened measurements, derived from $\mathbf{n}_k(\mathbf{v})$

δ	Scaling adjustment factor
$\varepsilon(\mathbf{v})$	Innovations process
$\boldsymbol{\varepsilon}$	Column stack representation of $\varepsilon(\mathbf{v})$
$\varepsilon_k(\mathbf{v})$	Innovations process in the k th layer
$\boldsymbol{\varepsilon}(\mathbf{v})$	Multi-resolution RFM innovations
$\boldsymbol{\varepsilon}_k(\mathbf{v})$	The whitened RFM innovations which are derived from the chip's background texture
$\widehat{\boldsymbol{\varepsilon}}_k^{H_0}(\mathbf{v})$	MLE of $\boldsymbol{\varepsilon}_k(\mathbf{v})$ under hypothesis H_0
$\widehat{\boldsymbol{\varepsilon}}_k^{H_1}(\mathbf{v})$	MLE of $\boldsymbol{\varepsilon}_k(\mathbf{v})$ under hypothesis H_1
η	GLRT threshold
$\boldsymbol{\theta}(\mathbf{r})$	RFM weight coefficients
$\boldsymbol{\theta}$	Column stack representation of $\boldsymbol{\theta}(\mathbf{r})$
$\boldsymbol{\theta}_k(\mathbf{r})$	RFM weight coefficients in the k th layer
$\lambda(\mathbf{v}, \boldsymbol{\theta})$	The eigenvalues of matrix $\mathbf{B}(\boldsymbol{\theta})$
$\boldsymbol{\mu}$	Expectancy of $\mathbf{z}(\mathbf{v})$
μ_{z_k}	Expectancy of $z_k(\mathbf{v})$
$\mu_{z_k}(\mathbf{v})$	Non-stationary local mean of $z_k(\mathbf{v})$
ρ	SNR adjustment factor
$\boldsymbol{\phi}_k(\mathbf{v})$	The coordinates of the interference signal components with respect to subspace \mathcal{A}_k
$\boldsymbol{\psi}_k(\mathbf{v})$	The coordinates of the target signal components with respect to subspace \mathcal{B}_k

Abbreviations:

ASD	Adaptive Subspace Detector
-----	----------------------------

CFAR	Constant False Alarm Rate
CM	Conditional Markov
DW	Dual Window
DWT	Discrete Wavelet Transform
EST	Eigen Separation Transform
FGM	Finite Gaussian Mixture
FLD	Fisher Linear Discriminant
GLR	Generalized Likelihood Ratio
GLRT	Generalized Likelihood Ratio Test
GMRF	Gaussian Markov Random Field
GPR	Ground-Penetrating Radar
GSM	Gaussian Scale Mixture
IWR	Inner Window Region
KLT	Karhunen-Loéve Transform
LMS	Least Mean Square
LR	Likelihood Ratio
LRT	Likelihood Ratio Test
LS	Least Squares
LSE	Least Squares Estimate
MAP	Maximum <i>a posteriori</i>
MR	Multi-Resolution
ML	Maximum Likelihood
MLE	Maximum Likelihood Estimate
MRF	Markov Random Field
MSD	Matched Subspace Detector

OWR	Outer Window Region
PCA	Principal Component Analysis
pdf	Probability Density Function
RDWT	Redundant Discrete Wavelet Transform
RFM	Random Field Model
ROC	Receiver Operating Characteristics
RX	Reed & Xiaoli detection algorithm
SAR	Simultaneous Auto-Regressive
SHT	Single Hypothesis Testing
SNER	Signal to Noise Energy Ratio
SNR	Signal to Noise Ratio

Chapter 1

Introduction

1.1 Motivation and Goals

Anomaly target detection is the process of locating elements in a scene which are unlikely to be a part of it. Anomaly detection techniques are useful in numerous applications, both civilian and military, such as detection of targets in multi-spectral and hyper-spectral images [4, 5, 8, 25, 29, 32, 47, 49, 53, 54, 59], detection of sea-mine targets in side-scan sonar images [15, 21, 34, 48], detection of land-mine targets in ground penetrating radar images [19, 57, 62, 63], detection of surface targets in synthetic aperture radar images [7, 40], detection of tumorous areas in medical imaging [61] and other signal processing and image analysis applications. The type of the scene and the type of the anomalous targets are application dependent. The detection process is generally performed with respect to a predefined probabilistic model and an appropriate feature space, in which a clear segregation between the anomalous elements and the rest of the background clutter in the scene is possible.

Anomaly detectors often use Bayesian classifiers, utilizing available *a priori* knowledge and *a posteriori* parametric statistics of both background clutter and anomalous targets. The probabilistic models which are used are usually Gaussian based, mainly due to the mathematical traceability of this distribution. Common classifiers are: the single hypothesis test (SHT) classifier [18], often employed in detection problems with a wide variety of potential targets which do not necessarily conform to a uniform model or even a characterizing subspace; the matched signal detector classifier, which can be employed when *a priori* typical signature of the target is available; the matched subspace detector (MSD) [22, 32, 42, 52, 59] and the adaptive subspace detector (ASD) [28] classifiers which are used when partial information about the targets allows the definition of *a priori* subspace in which the targets reside, leading to better detection results.

Random field models (RFM), such as the Simultaneous Auto-Regressive (SAR) and the Gaussian Markov Random Field (GMRF), have been applied extensively for spatial analysis of textural features in texture synthesis [10, 16], image segmentation [12, 25, 27, 37, 51], texture classification [13, 58] and target detection [6, 22, 25, 48, 54] algorithms. Single resolution spatial analysis introduces high false alarms in semi-homogenous background textures due to deviations from the RFM. To overcome this, Goldman and Cohen have proposed in [22] a multi-resolution GMRF model and a corresponding anomaly detection algorithm using an MSD classifier, achieving better detection results when compared to single resolution spatial analysis detection algorithms. However, the SAR and the GMRF models are highly affected by the choice of their neighbor set [9, 10, 26]. Different neighbor sets account for different textural patterns. Inappropriate choice of a neighbor set increases the prediction error

and causes the incorrect estimation of the innovations covariance, resulting in higher false alarms due to SNR degradation. Multi-resolution decompositions, such as the wavelet transform, are often used for feature extraction. These decompositions use a set of multi-scale bandpass oriented filters for decomposing the image, a process which is effective at decoupling high-order statistical features of natural images. In addition, it efficiently represents the visually relevant features of images [44], roughly de-correlating them while preserving spatial resolution [35]. However, wavelet based multi-resolution decompositions have two common phenomena [39]: heavy tails of the marginal probability density function of the features (known as excess kurtosis) and volatility clustering (a characteristics in which large changes tend to follow large changes and small changes tend to follow small changes). The first phenomena leads to potentially higher false alarms in Gaussian based classifiers due to the inadequacy between the model and the data and therefore calls for an alternative scheme that utilizes suitable distributions which can account for non-Gaussian marginal statistics, such as the Gaussian Scale Mixture (GSM). The second phenomena leads to deviations of the clutter image from its RFM, resulting in higher false alarms due to SNR degradation.

In this work we aim to formulate anomaly detectors which overcome the mentioned weaknesses, designated to detect anomalous targets in harsh environments where signal to noise energy ratio is very low, utilizing both the spatial and spectral multi-resolution structures of background clutter images.

1.2 Overview of the Thesis

In this thesis, we propose an unsupervised anomaly detection scheme which does not rely on the exhaustive statistical model of the targets, but rather on the local multi-resolution statistics of the background clutter and possibly on some *a priori* information of the minimal expected size of the targets (Chapter 3). Our choice of a feature space is motivated by previous work on the enhancement of texture segmentation by Unser and Eden [65] and texture classification by Mittelman and Porat [36]. We utilize the RDWT for the purpose of generating a multi-resolution feature space. We calculate from the resulting wavelet coefficients their local second moment estimates (corresponding to the GSM hidden multipliers maximum likelihood estimates), followed by the logarithmic transformation. The use of the logarithmic transformation was reported to have the effect of variance equalization which yields better segmentation results [65]. The resulting feature space, when derived from natural textures, was shown to follow the Gaussian distribution [35, 43], hence making it suitable for use with Bayesian classifiers. We then employ additional smoothing to the resulting feature channels. This final averaging reduces the feature component variances and results in clusters in feature space that are more compact and easier to distinguish. We show that increasing the size of the averaging window yields better detection results, as long as the window size does not exceed the anomalous target size. Our choice of a classifier is motivated by previous work on anomaly detection by Goldman and Cohen [21], where the SHT was used. Applying the SHT on the proposed feature space yields an anomaly detection algorithm with constant false alarm rate (CFAR) regardless of the background clutter and anomaly type, depending only on the feature space dimensionality. The proposed scheme can be applied to texture classification,

achieving improved classification results.

In addition, we introduce a multi-resolution non-casual RFM along with a corresponding unsupervised anomaly subspace detection algorithm (Chapter 4). The proposed multi-resolution RFM is less susceptible to its choice of neighbors, thus achieving fewer false alarms. We utilize the RDWT for the purpose of generating a multi-resolution feature space. We then employ the squaring non-linearity on the derived features. Each layer is modeled as a non-casual RFM with different sets of parameters, taking into consideration introduced correlation between pixels which are not accounted for in the GMRF model. This moderates the need for a proper choice of a neighborhood for each background texture. The field of the RFM at any point in the image is influenced by the field in all directions around it and there is no preferred direction of dependence. This is an important property which is intrinsic to most spatial phenomenon [54]. The squaring non-linearity enhances anomaly segregation and at the same time reduces RFM prediction error, resulting in improved SNR and consequently in improved detection results. We then perform anomaly detection using a multi-resolution MSD classifier. The MSD is formulated for detecting additive subspace target signals in a background multi-resolution RFM noise environment with possible additive subspace interference signals. The proposed MSD takes into consideration the introduced interaction between the background image and the *a priori* subspaces, while preserving target subspace dimensionality. The MSD utilizes the correlation both within and between layers, allowing the detection process to be based on feature space data from adjacent layers of the multi-resolution representation. We show that the proposed algorithm is closer in achieving theoretical detection results when compared to recently published MSD based anomaly detector [22].

We have implemented the proposed algorithms and tested them with various scenes, containing Brodatz-like background textures [1] and target anomalies. Typical detection performance with comparison to recently published detection and segmentation methods is given in Figure 1.1. The proposed algorithms mimics the detection mechanism of the human eye, utilizing both spatial and spectral correlations for their advantage, achieving outstanding detection results even when using textures with significant visual resemblance between the anomalous target and the background clutter. The results demonstrate the robustness and flexibility of the proposed algorithms in adverse environments.

1.3 Organization

The organization of this thesis is as follows. In Chapter 2, we review texture statistical models which are relevant to our work. We discuss recently published texture segmentation and classification approaches and their possible application to anomaly detection. We then review common classifiers which are used for anomaly detection and give a brief overview of recently published anomaly detection algorithms. In Chapter 3, we introduce a multi-resolution feature space which follows the Gaussian distribution and corresponding algorithms for unsupervised anomaly detection and texture classification. We analyze the performance of the proposed algorithms and compare the classification results to those obtained by using competing methods. We demonstrate the application of the proposed detection algorithm to automatic target detection in both synthesized and real imagery. In Chapter 4, we introduce a multi-resolution non-casual RFM along with a corresponding unsupervised anomaly subspace detection algorithm. We analyze the performance of the proposed algorithm

and compare the detection results to those obtained by using competing methods. We define scaling requirements for enhanced performance. We demonstrate the application of the proposed algorithm to automatic target detection in both synthesized and real imagery. Finally, in Chapter 5 we conclude with a summary and discussion on future research directions.

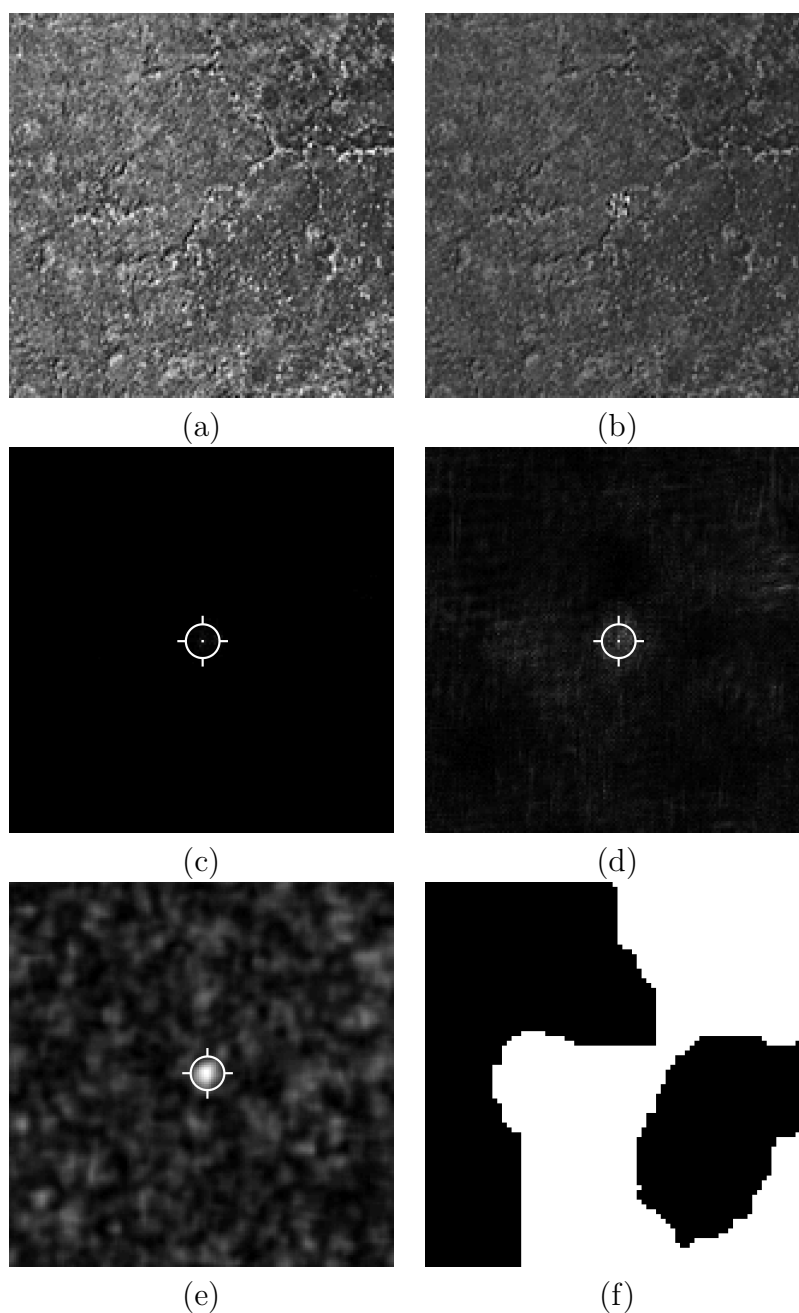


Figure 1.1: A comparison between detection methods. (a) Background natural texture of a stone. (b) Same texture but with an additive squared shaped synthetic anomaly in its center. The synthetic anomaly was created using image chips taken from a texture of metal, not having evident visual resemblance to the stone texture. The anomaly was scaled to achieve $\text{SNR} = 30[\text{dB}]$. Anomaly detection results using various methods: (c) Proposed algorithm (Chapter 4). (d) Goldman and Cohen [22]. (e) Proposed algorithm (Chapter 3). (f) Mittelman and Porat segmentation algorithm [35]. The white target mark is attached only to the highest value in each detection image.

Chapter 2

Background

2.1 Introduction

Anomaly detection, image segmentation and texture classification schemes usually rely on statistical characterization of the underlying data, often using similar textural features. Each of these schemes addresses a different problem and performs poorly when applied outside of its domain. In this chapter we review the main building blocks of these schemes, focusing on anomaly target detection.

The organization of this chapter is as follows. In Section 2.2, we review the GMRF and the GSM statistical models. In Section 2.3, we discuss recently published texture segmentation and classification approaches and their possible application to anomaly detection. In Section 2.4, we review the SHT and the MSD classifiers along with their theoretical statistical behavior when applied on multivariate Gaussian features. We then give a brief overview of recently published anomaly detection algorithms.

2.2 Texture Modeling

Anomaly detection is generally performed with respect to a predefined probabilistic model and an appropriate feature space in which a clear segregation between the anomalous elements and the rest of the background clutter in the scene is possible. The assumed probabilistic model of the derived feature space enables the formulation of proper classifiers and allows to evaluate their theoretical detection performance. Statistical texture modeling therefor assumes that the feature space of a given texture is characterized a by certain statistical model. Texture modeling can be obtained either by deriving statistical features directly from the texture image or by fitting the image into a class of models known as spatial interaction models [9]. The fundamental difference between these two approaches is the ability to synthesize the originating texture from its model. Spatial interaction models allow to synthesize an approximation of the originating texture from the estimated model parameters whereas textural features which are derived directly from the texture in general do not. Either way, the model is required to capture the highly correlated spatial nature of the background clutter in textures. In this section we give a brief overview on statistical textural models which are relevant to our work.

2.2.1 The Non-Casual GMRF Model

The Gaussian Markov Random Field (GMRF) model, referred also as the conditional Markov (CM) model, belongs to the class of spatial interaction models. The model represents each pixel in a given image as a weighted sum of pixels at nearby locations and an additive prediction error. The additive prediction error is often referred as the innovations process. The GMRF possesses two important properties that are

intrinsic to most spatial phenomenon: non-causality and Markovianity [54]. Non-causality refers to the notion that the field at any pixel is influenced by the field in all directions around it; there is no preferred direction of dependence. Markovianity is the statistical formalization of the notion of locality, *i.e.*, that the field at a pixel is regressed on the values of the field at neighboring pixels.

The infinite lattice GMRF model for a stationary image $\{y(\mathbf{v})\}$ is given by:

$$y(\mathbf{v}) = \sum_{\mathbf{r} \in \mathcal{R}} \theta(\mathbf{r})y(\mathbf{v} + \mathbf{r}) + \varepsilon(\mathbf{v}), \quad (2.1)$$

where \mathcal{R} denotes a given set of indices representing the neighborhood of a pixel, $\theta(\mathbf{r})$ denotes the weight coefficient of a neighbor $\mathbf{r} \in \mathcal{R}$, $\varepsilon(\mathbf{v})$ is an additive spatially correlated Gaussian noise sequence with zero mean and variance ρ^2 and $E[y(\mathbf{v})] = 0$. The weight coefficients $\{\theta(\mathbf{r})\}_{\mathbf{r} \in \mathcal{R}}$ and the innovations variance ρ^2 are unknown parameters that need to be estimated. Following the Markovian assumption, the conditional probability of $y(\mathbf{v})$ given all the other values of $y(\cdot)$ depends only upon a finite group of neighboring pixels $\{y(\mathbf{v} + \mathbf{r}) | \mathbf{r} \in \mathcal{R}\}$. As such, the innovations process of a GMRF is spatially correlated with covariance given by [68]:

$$E\{\varepsilon(\mathbf{v})\varepsilon(\mathbf{v} + \mathbf{r})\} = \begin{cases} \rho^2 & , \text{if } \mathbf{r} = (0, 0) \\ -\theta(\mathbf{r})\rho^2 & , \text{if } \mathbf{r} \in \mathcal{R} \\ 0 & , \text{otherwise} \end{cases}, \quad (2.2)$$

where $\rho^2 = E\{\varepsilon^2(\mathbf{v})\}$ and $E\{\varepsilon(\mathbf{v})\} = 0$. This correlation structure imposes symmetry on the neighborhood set \mathcal{R} which necessitate that $\theta(\mathbf{r}) = \theta(-\mathbf{r})$ for $\mathbf{r} \in \mathcal{R}$ [26]. The symmetric neighborhood \mathcal{R} can be arbitrary as long as $(0, 0) \notin \mathcal{R}$.

Given a finite stationary image $\{y(\mathbf{v})\}_{\mathbf{v} \in \Omega}$ defined on a $M \times M$ toroidal lattice Ω ,

equation (2.1) can be rewritten using \mathbf{y} and $\boldsymbol{\varepsilon}$ as the column stack representations of $y(\mathbf{v})$ and $\varepsilon(\mathbf{v})$ respectively, as:

$$\mathbf{B}(\boldsymbol{\theta})\mathbf{y} = \boldsymbol{\varepsilon}, \quad (2.3)$$

where $\mathbf{B}(\boldsymbol{\theta})$ is a block-circulant matrix, $\boldsymbol{\theta} = \text{col}[\theta(\mathbf{r}), \mathbf{r} \in \mathcal{R}]$ and the innovations follow: $\boldsymbol{\varepsilon} \sim \mathcal{N}(\mathbf{0}, \rho^2 \mathbf{B}(\boldsymbol{\theta}))$. Since the neighborhood \mathcal{R} is symmetric, the matrix $\mathbf{B}(\boldsymbol{\theta})$ is symmetric as well. The toroidal lattice determines the boundaries of the image such $y(\mathbf{v} + (M, M)) = y(\mathbf{v})$. The block-circulant matrix $\mathbf{B}(\boldsymbol{\theta})$ is required to be positive definite. A necessary and sufficient condition on the weight coefficients to ensure this requirement is given by:

$$\lambda(\mathbf{v}, \boldsymbol{\theta}) = 1 - \sum_{\mathbf{r} \in \mathcal{R}} \theta(\mathbf{r}) \cos\left(r_1 \frac{2\pi v_1}{M} + r_2 \frac{2\pi v_2}{M}\right) > 0, \quad \forall \mathbf{v} \in \Omega \quad (2.4)$$

where $\mathbf{v} = (v_1, v_2)$ and $\mathbf{r} = (r_1, r_2)$.

The problem of estimating the GMRF model parameters was previously addressed in the literature [24–26, 35, 53] and various solutions were proposed. The ML estimation method yields asymptotically consistent and efficient estimates. However, this method requires numerical optimizations and is known to be computationally unattractive. Smirnov and Anselin suggested in [56] a new scheme for fast ML estimation that may fit the problem at hand. Kashyap and Chellappa presented in [26] a computationally efficient method for estimating the parameters of the GMRF model using LS estimation. They have also shown the asymptotic consistency of this approach and proposed a method for choosing the appropriate neighborhood \mathcal{R} that best models a given texture. Following [26, 53], the LS estimates for $\boldsymbol{\theta}$ and ρ^2 are

given by:

$$\hat{\boldsymbol{\theta}} = \left[\sum_{\mathbf{v} \in \Omega} \mathbf{w}(\mathbf{v}) \mathbf{w}(\mathbf{v})^T \right]^{-1} \left[\sum_{\mathbf{v} \in \Omega} y(\mathbf{v}) \mathbf{w}(\mathbf{v}) \right], \quad (2.5)$$

$$\hat{\rho}^2 = \frac{1}{M^2} \sum_{\mathbf{v} \in \Omega} \left(y(\mathbf{v}) - \hat{\boldsymbol{\theta}}^T \mathbf{w}(\mathbf{v}) \right)^2, \quad (2.6)$$

where $\mathbf{w}(\mathbf{v}) = \text{col}[y(\mathbf{v} + \mathbf{r}), \mathbf{r} \in \mathcal{R}]$. This estimation scheme for the GMRF model parameters was previously used in the work of Hazel [25] and Goldman and Cohen [22], among others.

2.2.2 The GSM Statistical Model

The Gaussian Scale Mixture (GSM) is a statistical model which can account for both marginal and joint distribution properties of local neighborhoods of wavelet coefficients that are derived from natural images [35, 43, 44, 60].

A random vector $\mathbf{x} \in \mathbb{R}^{N \times 1}$ follows the GSM model if $\mathbf{x} = \sqrt{z} \mathbf{u}$, where z is a positive scalar random variable called the hidden multiplier and $\mathbf{u} \sim \mathcal{N}(\mathbf{0}, \mathbf{C}_{\mathbf{u}})$ is a Gaussian random vector. The random variable z and the random vector \mathbf{u} are statistically independent. Therefore, the pdf of a random vector which follows the GSM model is of the form:

$$P(\mathbf{x}) = \int_0^{\infty} P(\mathbf{x}|z) P_z(z) dz, \quad (2.7)$$

where:

$$(\mathbf{x}|z) \sim \mathcal{N}(\mathbf{0}, z \mathbf{C}_{\mathbf{u}}). \quad (2.8)$$

For the case where $N = 1$, the GSM model corresponds to a Finite Gaussian Mixture (FGM) model with infinite Gaussian random variables. Thus, the model is more general compared to the FGM. In general, there is no explicit form for $P_z(z)$ and as a result, spectral histograms of the hidden multiplier are often being used [35,36]. The ML estimator of the GSM hidden multiplier, derived from equation (2.8), is given by:

$$\hat{z}(\mathbf{x}) = \frac{1}{N} \mathbf{x}^T \mathbf{C}_{\mathbf{u}}^{-1} \mathbf{x}. \quad (2.9)$$

When considering the local environment of wavelet transform coefficients, under the assumption that the wavelet transform coefficients are roughly de-correlated, the covariance matrix of \mathbf{u} is of the form $\mathbf{C}_{\mathbf{u}} \approx \sigma_u^2 \mathbf{I}$. Although this assumption disregards existing spatial correlation in the multi-resolution decomposition layers, it simplifies the estimation of the hidden multipliers and sustains spatial correlation in the estimated data when using small local neighborhoods for the estimation. The variance σ_u^2 in equation (2.9) is a proportionality constant and setting its value to one results in:

$$\hat{z}(\mathbf{x}) = \frac{1}{N} \mathbf{x}^T \mathbf{x}, \quad (2.10)$$

where N is the number of coefficients within the local neighborhood. The hidden multiplier's estimate therefore corresponds to the local second moment estimate.

Mittelman and Porat have shown in [36] that classification algorithms which are based on spectral histogram of the GSM hidden multipliers estimates require a logarithmic scale for the histogram bin centers. The distribution of the hidden multipliers in multi-resolution decompositions of natural images was shown empirically to be closely modeled by a Gaussian density function on a logarithmic scale [35,43,44]. As

such, the GSM can be used in a Bayesian framework. This characteristic is important and we shall use it in Chapter 3.

2.3 Texture Segmentation and Classification

In this section we give a brief overview on texture segmentation and texture classification, along with possible applications of recently published methods to anomaly target detection.

2.3.1 Texture Classification

Texture classification is a fundamental problem in computer vision with a wide variety of applications. Two fundamental issues in texture classification are how to characterize textures using derived features and how to define a robust distance/similarity measure between textures so that the distance between images of the same texture is small and that among images from different textures is large. Because images of the same underlying texture can vary significantly, textural features must be invariant to large image variations and at the same time sensitive to intrinsic spatial structures that define textures [30].

A common framework for extracting textural features is composed of several consecutive stages [45]. The first stage produces a multi-resolution decomposition of the texture image using a bank of filters and is motivated by studies on the human visual system [66]. The use of a bank of filters provide efficient ways of extracting spatial structures at different orientations and frequencies. The marginal distributions of responses of a bank of filters were shown to be sufficient for characterizing the

joint distributions which are implicitly defined by a texture image [30]. However, the choice of filters affects the classification performance and was shown to be texture dependent [45], thus requiring the selection of appropriate filters to be used with a given data set. The second stage employs a nonlinearity on the initial features. This has the effect of converting variance disparities into mean values differences. The features are then spatially smoothed using rectangular or Gaussian filters to produce texture energy measures, characterizing certain local texture properties of the neighborhood of a given pixel. In practice, squaring followed by a spatial smoothing using a rectangular filter produce the MLE of the GSM hidden multipliers estimates, as given in equation (2.10). The last stage employs a normalizing nonlinearity on the derived features, having the effect of variance equalization. The combination of the squaring operator as the first nonlinearity and the logarithm normalization as the second nonlinearity was reported to perform best [65].

The marginal distributions of the filters responses are insensitive to the precise locations of textures elements in a texture image and therefore no-alignment of images is required prior to classification. Recently published classification schemes have used the χ^2 statistic between spectral histograms of the marginal distributions as a distance measure between textures [30, 36]. This distance measure is defined as follows:

$$\chi^2(\mathcal{H}_1, \mathcal{H}_2) = \sum_{i=1}^N \frac{(\mathcal{H}_1(i) - \mathcal{H}_2(i))^2}{\mathcal{H}_1(i) + \mathcal{H}_2(i)}, \quad (2.11)$$

where \mathcal{H}_1 and \mathcal{H}_2 are two histograms of marginal distributions with N bins each. The χ^2 statistic between spectral histograms was reported to exhibit nonlinearity which is consistent with the human texture perception, providing a robust distance measure for comparing textures [30]. This distance measure can be used for locating elements in a

scene which present different marginal distributions properties than the background clutter. However, this heuristic detection scheme requires a supervised selection of a proper threshold to be used with the distance measure along with enough information for producing spectral histograms of the anomaly.

2.3.2 Unsupervised Texture Segmentation

Algorithms of unsupervised texture segmentation aim to segment a given image scene into its constituent texture classes, utilizing *a priori* information regarding the number of classes in the scene. In global anomaly detection approaches [54], the image scene is first segmented into its constituent classes using an unsupervised texture segmentation algorithm and then detection is achieved by determining the outliers of these classes. The majority of global anomaly detectors employ 2-D Markov random field (MRF) modeling in order to incorporate spatial features into the segmentation process.

In [37], Mittelman and Porat proposed an unsupervised texture segmentation scheme, utilizing a multi-resolution observation field and a class label field. The multi-resolution observation field was derived using the logarithm of the local second moment estimates of the DWT coefficients and was assumed to follow the GMRF model. The class label field was assumed to follow the MRF model. Segmentation was performed using MAP estimation of the distribution of the class label field given the multi-resolution observation field, utilizing the Gibbs distribution. The MAP estimation was performed in an iterative fashion, constantly updating the GMRF model parameters of the different classes, until a stopping criteria was met. Initial

segmentation was performed utilizing k -mean clustering of logarithmically scaled histograms of the local second moment estimates. Similar single resolution approach, where the image itself was assumed to follow the GMRF model, was presented in [12].

These algorithms perform well in scenes where segregation between the various classes is visually evident. However, when considering a scene which contains a single background natural texture and sparsely placed small anomalies, detection often fails and the algorithm converges to a segmentation of the background clutter itself rather than the background clutter and the anomalies. We demonstrate this in Figure 1.1 (f). These schemes can be used for segmenting a given scene into several texture classes prior to anomaly detection which is then performed in each class separately (as in global anomaly detection approaches).

2.4 Anomaly Detection

Algorithms of anomaly detection in images aim to locate elements in a scene which are unlikely to be a part of it. This is a challenging task, mainly due to the large variability of the scene's background clutter and the appearance of the anomalous elements. There is no single best model for anomaly detection and the success depends not only on the type of method which is being used but also on the statistical properties of the data [33]. Statistical approaches for anomaly detection are mostly based on modeling data using its statistical properties and using this information to estimate whether a test pattern (*i.e.*, feature vector) comes from the same distribution or not. A simple yet powerful approach for anomaly detection is the statistical hypothesis

testing. Under this approach, a test pattern follows different distributions corresponding with different predefined hypotheses, allowing the formulation of a decision rule with known detection rate and false alarm probabilities. The distributions' pdf can be derived from the training data by either parametric or non-parametric approaches. Parametric approaches assume that the pdf belongs to a family of known models and certain parameters are calculated to fit the model of choice. Non-Parametric approaches often use histogram analysis and therefore give greater flexibility in general systems. Parametric hypothesis testing is applied extensively in the field of anomaly detection and can appear in the form of single hypothesis testing (SHT), matched signal detector or matched subspace detector (MSD). In this section we give a brief overview on anomaly detectors that are being used in our work, followed by a brief overview of recently published anomaly detection algorithms which have been reported to perform well in various applications.

2.4.1 Single Hypothesis Test

Detection problems that include a wide variety of potential targets which do not necessarily conform to a uniform model or even a characterizing subspace render the study of the distributions of all possible targets before a decision rule is designed impossible. SHT schemes are useful for situations in which one class is well defined (the background clutter) and the others are not (the potential targets). The simplest SHT approach can be based on constructing a density function for data of a known class, representing the background clutter in the image, and then computing the probability of a test pattern of belonging to that class. The probability estimate can then be compared to a threshold for anomaly detection. Another simple model can be based on the distance of a test pattern from a class mean, representing the background

clutter in the image, in terms of standard deviation. The distance measure itself can be Mahalanobis or some other probabilistic distance [14, 18, 67].

Let \mathbf{y} denote a multivariate feature vector with m variables. Let hypothesis H_0 denote the case where the feature vector belongs to the background clutter. Let hypothesis H_1 denote the case where the feature vector does not belong to the background clutter and as such, regarded as an anomaly. Let $P(\mathbf{y}|H_0)$ denote the pdf of a feature vector which is derived from the background clutter. The decision rule under the SHT scheme is then given by:

$$P(\mathbf{y}|H_0) \underset{H_1}{\overset{H_0}{\gtrless}} \xi, \quad (2.12)$$

where ξ is the threshold that determines if the feature vector is regarded as an anomaly or background clutter. When considering a feature space which follows the multivariate Gaussian distribution, $\mathbf{y}|_{H_0} \sim \mathcal{N}(\boldsymbol{\mu}, \boldsymbol{\Sigma})$, the decision rule in equation (2.12) becomes:

$$d = (\mathbf{y} - \boldsymbol{\mu})^T \boldsymbol{\Sigma}^{-1} (\mathbf{y} - \boldsymbol{\mu}) \underset{H_0}{\overset{H_1}{\gtrless}} \eta, \quad (2.13)$$

where η is the threshold that determines if the feature vector is regarded as an anomaly or background clutter and d is the Mahalanobis distance of the feature vector \mathbf{y} from $\boldsymbol{\mu}$. The decision rule in equation (2.13) does not rely on any information about the anomalous targets but rather on an estimated model of the background clutter. Based on equation (2.13) and the Gaussian assumption, the Mahalanobis distance under hypothesis H_0 is chi-square distributed with m degrees of freedom, regardless of the background clutter:

$$d|_{H_0} \sim \chi_m^2(0). \quad (2.14)$$

The false alarm is then given by:

$$P_{FA} = P(H_1|H_0) = 1 - P(\chi_m^2(0) \leq \eta), \quad (2.15)$$

yielding an CFAR detection scheme. The detection rate $P_D = P(H_1|H_1)$ depends on the statistics of $d|_{H_1}$ which characterize different types of anomalous targets with respect to the background clutter.

2.4.2 Matched Subspace Detection

In many detection problems, some *a priori* information about target and interfering signals is available. This information may include details about the exact nature of the target signals or may be more general. Incorporating this information into the detection scheme should improve detection performance. A matched signal detector can be employed when a typical signature of a target is available. Yet, in practical detection problems the information about targets is partial, allowing to define a subspace in which targets reside. The matched subspace detector (MSD) is a Bayesian classifier which assumes a multivariate normal distribution model. Although given various formulations in the literature (Scharf and Friedlander [52], Kraut *et al.* [28], Manolakis and Shaw [32], Stein *et al.* [59], Goldman and Cohen [22], Noiboar and Cohen [39]), its concept remains the same, allowing for the detection of additive subspace target signals in a background Gaussian noise environment with possible additive subspace interference signals.

Let $\mathcal{A}\phi$ denote an interfering signal within an interference signal subspace $\langle \mathcal{A} \rangle$, where ϕ is a vector of coefficients and the interference subspace $\langle \mathcal{A} \rangle$ is spanned by the columns of matrix \mathcal{A} . Let $\mathcal{B}\psi$ denote a target signal within a target signal subspace

$\langle \mathcal{B} \rangle$, where $\boldsymbol{\psi}$ is a vector of coefficients and the target subspace $\langle \mathcal{B} \rangle$ is spanned by the columns of matrix \mathcal{B} . Let \mathbf{y} denote a feature vector of observations. We define two possible hypotheses for each feature vector:

$$\begin{aligned} H_0 &: \mathbf{y} = \mathcal{A} \boldsymbol{\phi} + \mathbf{n}, \\ H_1 &: \mathbf{y} = \mathcal{B} \boldsymbol{\psi} + \mathcal{A} \boldsymbol{\phi} + \mathbf{n}, \end{aligned} \quad (2.16)$$

where H_0 and H_1 represent the absence and presence of anomalous target signal in the image respectively and \mathbf{n} is a multivariate white Gaussian noise such $\mathbf{n} \sim \mathcal{N}(\mathbf{0}, \mathbf{I})$. The detection problem can be formulated as a Bayes Likelihood Ratio Test (LRT) between hypotheses H_0 and H_1 , given by [18]:

$$P(H_1)P(\mathbf{y}|H_1) \underset{H_0}{\overset{H_1}{\geq}} P(H_0)P(\mathbf{y}|H_0), \quad (2.17)$$

which is the same as:

$$P(H_1)P(\mathbf{n}|H_1) \underset{H_0}{\overset{H_1}{\geq}} P(H_0)P(\mathbf{n}|H_0). \quad (2.18)$$

Let $\mathbf{P}_{\mathcal{A}}$ and $\mathbf{P}_{\mathcal{AB}}$ denote the projection operators onto subspaces $\langle \mathcal{A} \rangle$ and $\langle \mathcal{A}, \mathcal{B} \rangle$ respectively. Subspace $\langle \mathcal{A} \rangle$ is spanned by the columns of matrix \mathcal{A} and subspace $\langle \mathcal{A}, \mathcal{B} \rangle$ is spanned by the columns of the concatenated matrix $[\mathcal{A}, \mathcal{B}]$. The projection operator $\mathbf{P}_{\mathcal{A}}$ is given by [32, 52]:

$$\mathbf{P}_{\mathcal{A}} = \mathcal{A} (\mathcal{A}^T \mathcal{A})^{-1} \mathcal{A}^T. \quad (2.19)$$

The projection operator $\mathbf{P}_{\mathcal{AB}}$ is defined the same using $[\mathcal{A}, \mathcal{B}]$. Let $\widehat{\mathbf{n}}^{H_0}$ and $\widehat{\mathbf{n}}^{H_1}$ denote the ML estimates of the noise \mathbf{n} under hypotheses H_0 and H_1 respectively. These estimates are obtained by subtracting the components which lie in the target and interference derived subspaces from the sample vector \mathbf{y} as follows:

$$\begin{aligned} \widehat{\mathbf{n}}^{H_0} &= (\mathbf{I} - \mathbf{P}_{\mathcal{A}}) \mathbf{y} \triangleq \mathbf{P}_{\mathcal{A}}^\perp \mathbf{y}, \\ \widehat{\mathbf{n}}^{H_1} &= (\mathbf{I} - \mathbf{P}_{\mathcal{AB}}) \mathbf{y} \triangleq \mathbf{P}_{\mathcal{AB}}^\perp \mathbf{y}, \end{aligned} \quad (2.20)$$

where \perp denotes the projection operator to the orthogonal complement subspace, *i.e.*, $(\mathbf{P}_{\mathcal{A}}\mathbf{y})^T (\mathbf{P}_{\mathcal{A}_k}^\perp \mathbf{y}) = 0$. The Generalized Likelihood Ratio (GLR) is derived using the ML estimates of the noise \mathbf{n} under hypotheses H_0 and H_1 and is given by:

$$\begin{aligned} L &= 2 \log \frac{P(\mathbf{n}|H_1)}{P(\mathbf{n}|H_0)}, \\ &= \|\widehat{\mathbf{n}}^{H_0}\|^2 - \|\widehat{\mathbf{n}}^{H_1}\|^2, \\ &= \mathbf{y}^T (\mathbf{P}_{\mathcal{A}}^\perp - \mathbf{P}_{\mathcal{AB}}^\perp) \mathbf{y}, \\ &= \mathbf{y}^T (\mathbf{P}_{\mathcal{AB}} - \mathbf{P}_{\mathcal{A}}) \mathbf{y}. \end{aligned} \tag{2.21}$$

The quadratic form of the GLR may be thought of as the norm-squared of $(\mathbf{P}_{\mathcal{AB}} - \mathbf{P}_{\mathcal{A}})\mathbf{y}$. Therefor, L is chi-square distributed with r degrees of freedom [32, 41, 52]:

$$L \sim \begin{cases} \chi_r^2(0) & , \text{ under } H_0 \\ \chi_r^2 \left(\|\mathbf{P}_{\mathcal{A}}^\perp \mathcal{B} \boldsymbol{\psi}\|^2 \right) & , \text{ under } H_1 \end{cases}, \tag{2.22}$$

where r is the rank of the target subspace $\langle \mathcal{B} \rangle$ and $\|\mathbf{P}_{\mathcal{A}}^\perp \mathcal{B} \boldsymbol{\psi}\|^2$ is defined as the MSD SNR. The GLRT is given by:

$$L \underset{H_0}{\overset{H_1}{\geq}} \eta, \tag{2.23}$$

resulting in the following detection rate and false alarm probabilities:

$$\begin{aligned} P_D &= P(H_1|H_1) = 1 - P \left(\chi_r^2 \left(\|\mathbf{P}_{\mathcal{A}}^\perp \mathcal{B} \boldsymbol{\psi}\|^2 \right) \leq \eta \right), \\ P_{FA} &= P(H_1|H_0) = 1 - P \left(\chi_r^2(0) \leq \eta \right). \end{aligned} \tag{2.24}$$

The detection performance of the MSD is highly affected by two main parameters: the target subspace dimensionality r and the SNR. The detection performance of the MSD improves with an increasing SNR and a decreasing subspace dimensionality. This is demonstrated in Figure 2.1. The subspace projection operators can be also regarded as a subspace right multiplied by its pseudo-inverse. The pseudo-inverse

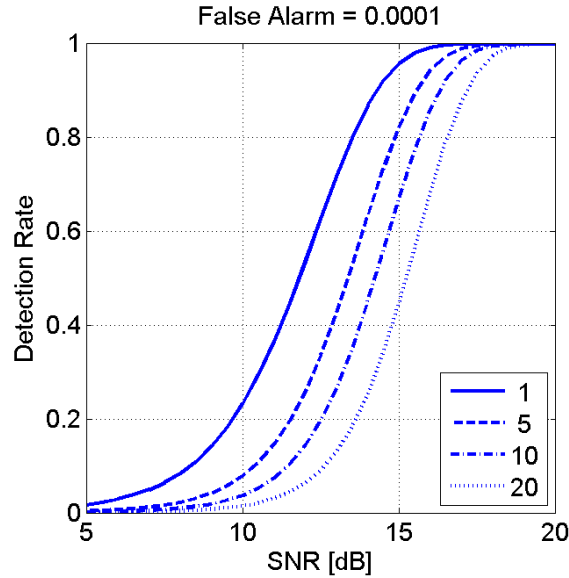


Figure 2.1: MSD performance. Detection rate vs. SNR for various values of the target subspace rank r . Performance is given at false alarm rate of 10^{-4} .

detector was reported to be the most robust detector for the purpose of detecting a signal mismatch in additive white noise [42]. The signal mismatch is defined in [42] as the difference between the target signal and its projection to a given target signal subspace (*i.e.*, a projection residual which lies in the orthogonal complement of the target signal subspace).

2.4.3 Overview of Algorithms

Goldman and Cohen, 2005

Goldman and Cohen have formulated in [22] a multi-resolution GMRF model and a corresponding anomaly detection algorithm. The algorithm was developed for target detection in cluttered images which follow the proposed model, which is based on a multi-resolution representation of the image and the KLT. They generated a multi-layer representation with independent layers from a given image and assumed that

these independent layers can be modeled as GMRFs with different sets of parameters. The detection was subsequently carried out by applying a modification of the MSD to be used with the innovations process (prediction error) of the multi-resolution GMRF. The MSD incorporated the available *a priori* information about the targets into the detection process and thus improved the detection performance. Experimental results have shown the ability to detect sea-mines in side scan sonar images. However, this method suffers from high false alarms, mainly due to inconsistency between the feature space distribution and the classifier's Gaussian assumption and the inappropriate choice of neighbor set to be used with the GMRF. We shall use this detection method as a benchmark to evaluate our work.

Schweizer and Moura, 2001

Schweizer and Moura have formulated in [54] two 3-D GMRF anomaly detectors for natural clutter backgrounds in hyper-spectral imagery, utilizing the GMRF model for capturing the high levels of spatial and spectral correlation that exist in the data. Detection was performed using hypothesis testing techniques applied to the resulting innovations, attempting to locate anything that displays different spatial and/or spectral characteristics from its surroundings. The GMRF was derived using a first order 3-D field in which the intensity of a pixel is described in terms of its six nearest neighbors: four spatial and two spectral neighbors, assuming that the Gaussian process describing the dominant image background has a slowly varying covariance structure. Yet, this method might produce high false alarms because of the same reasons as in [22]: inconsistency between the feature space distribution and the classifier's Gaussian assumption and the inappropriate choice of neighbor set to be used with the GMRF. However, the notion of incorporating a 3-D field into

the detection process is worthwhile and should be studied in future research which integrates both hyper-spectral and multi-resolution decomposition data.

Kwon *et.al.*, 2003

Kwon *et.al.* have formulated in [29] a set of adaptive anomaly detectors intended to find materials in hyper-spectral images whose spectral characteristics are substantially different from those of the surrounding materials. They used a dual rectangular window, separating the local area into two regions - an Inner Window Region (IWR) and an Outer Window Region (OWR). The statistical spectral differences between the IWR and OWR were exploited by generating subspace projection vectors onto which the IWR and OWR vectors are projected. Anomalies were detected if the projection separation between the IWR and OWR vectors was greater than a predefined threshold. Four different methods were used to produce the subspace projection vectors:

1. Eigen-Separation Transform (EST): The projection vectors are the eigenvectors associated with the highest eigenvalues of the covariance difference matrix. This method achieved the best detection results.
2. Principal Component Analysis (PCA): The projection vectors are the eigenvectors associated with the highest eigenvalues of the covariance matrix of the IWR or the OWR.
3. Fisher Linear Discriminant (FLD): The projection vector is selected as the linear projection operator which yields the maximum ratio of between-class scatter to within-class scatter [14] for the IWR and OWR classes. This method achieved the worst detection results.

4. RX Algorithm: The resulting statistical spectral difference is the Mahalanobis distance of the IWR with respect to the OWR.

The detectors were employed directly on hyper-spectral images and the spectral vectors were assumed to follow the multivariate Gaussian distribution. Only qualitative detection results were provided. The DW-EST was shown to achieve the best results. However, this method exploits differences in second-order data structures and therefor should perform poorly when used for detecting additive anomalous targets in low Signal to Noise Energy Ratio (SNER) conditions. Furthermore, the sample covariance estimation is performed using a small set of data and therefor is not accurate. The main limitation of these methods is that they neglect potentially valuable spatial correlation information of the clutter in each hyper-spectral image and only spectral information is being used for detecting anomalous targets.

Torrione *et.al.*, 2006 and Song *et.al.*, 2006

Torrione *et.al.* in [63] and Song *et.al.* in [57] have formulated detection algorithms for detecting land-mines in Ground-Penetrating Radar (GPR) images. Both employed the following pre-screening methods on processed GPR data:

1. A normalized energy detector, which is basically the Mahalanobis distance from the background clutter under the assumption that the samples are uncorrelated.
2. A 2-D LMS detector: A detector which is based on the residual error of an RFM with constantly adapted weight coefficients. The weight coefficients that are used with the next data point are adapted using the residual error from the current data point and the data in neighboring points. Detection is performed

by applying a threshold to the residual error without assuming a statistical model.

The purpose of these screening methods was to reduce introduced false alarms of post-classification algorithms. Typical raw GPR signatures of both metallic and plastic land-mines, as presented in [57], suggest that our proposed algorithms (Chapter 3 and Chapter 4) could be utilized for land-mines detection without pre-screening and pre-processing stages.

2.5 Summary

We have presented two common statistical models for texture modeling which are relevant to our work - the GMRF and the GSM. We have discussed recently published texture classification and segmentation schemes and possible applications of these schemes to anomaly detection. We have presented two common detection schemes which are relevant to our work - the SHT and the MSD. Finally, we gave a brief overview on recently published anomaly detection algorithms which have been reported to perform well in various applications.

Chapter 3

Anomaly Detection Using Multi-Resolution Gaussian Textural Features

3.1 Introduction

Multi-resolution decompositions, such as the wavelet transform, are often employed in anomaly detection algorithms for feature extraction. However, the extracted features may be unreliable for anomaly detection in textures due to inconsistencies between the assumed background model and the true data. In this chapter we present an anomaly detection scheme which relies on a statistical model of textures and is specifically designed for detection of anomalies in textures, utilizing spatial correlation rather than just energy measures. Motivated by recent work on texture segmentation and texture classification, we introduce a multi-resolution feature space that facilitates anomaly

detection with constant false alarm rate (CFAR) for a wide range of textures. Experimental results demonstrate that the proposed algorithm, when applied to images containing background texture, achieves improved detection results and lower false alarm rate than a competitive anomaly detection scheme. We further develop a texture classification scheme based on the introduced multi-resolution feature space and demonstrate improved classification results compared to a competitive texture classification method.

The organization of this chapter is as follows. In Section 3.2, we formulate the detection problem. In Section 3.3, we present the proposed anomaly detection algorithm. In Section 3.4, we analyze the performance of the proposed anomaly detection algorithm and demonstrate the application of the proposed algorithm to automatic target detection in both synthesized and real imagery. In Section 3.5, we present a texture classification approach which is based on the proposed anomaly detection algorithm. In Section 3.6, we compare the performance of the proposed texture classification approach to those obtained by using competing methods. In Section 3.7, we formulate a normalized feature space which voids energy from the detection scheme, resulting in a more robust detection algorithm.

3.2 Problem Formulation - Detached Anomaly

Let Ω be the support lattice for $\{y(\mathbf{s})\}_{\mathbf{s} \in \Omega}$ - the observations of an image containing a background natural texture with rare anomalous target signals scattered around in the image, denoted as $x(\mathbf{s})$ and $n(\mathbf{s})$ respectively. The target signals are assumed to be much smaller than the support lattice of the background image and therefore can

be regarded as transients. We define two possible hypotheses for each pixel $\mathbf{s} \in \Omega$:

$$\begin{aligned} H_0 : \quad y(\mathbf{s}) &= x(\mathbf{s}), \\ H_1 : \quad y(\mathbf{s}) &= n(\mathbf{s}), \end{aligned} \tag{3.1}$$

where H_0 and H_1 represent the absence and presence of an anomaly in the image respectively. The problem at hand is to define an anomaly detection algorithm that achieves:

$$\begin{aligned} P_D &\triangleq P(H_1|H_1), \quad P_D \geq 1 - \epsilon_1, \\ P_{FA} &\triangleq P(H_1|H_0), \quad P_{FA} \leq \epsilon_2, \end{aligned} \tag{3.2}$$

for given values of ϵ_1 and ϵ_2 .

3.3 Anomaly Detection Algorithm

A block diagram of the proposed algorithm is presented in Figure 3.1.

Let $\{y_j(\mathbf{s})\}_{j=1,\dots,m}$ denote the j th layer wavelet coefficients obtained from the mean normalized image observations $y(\mathbf{s})$ using an RDWT with $(m - 1)/3$ levels. Let $\{t_j(\mathbf{s})\}_{j=1,\dots,m}$ denote the logarithm of the GSM hidden multipliers estimate, given by:

$$t_j(\mathbf{s}) = \log \left(\frac{\sum_{\mathbf{r} \in \mathcal{R}_1} y_j^2(\mathbf{s} + \mathbf{r})}{|\mathcal{R}_1|} \right), \tag{3.3}$$

where \mathcal{R}_1 denotes a given set of indices representing the $N \times N$ local neighborhood of a pixel. Let $\{v_j(\mathbf{s})\}_{j=1,\dots,m}$ denote the proposed feature space, given by:

$$v_j(\mathbf{s}) = \frac{\sum_{\mathbf{r} \in \mathcal{R}_2} t_j(\mathbf{s} + \mathbf{r})}{|\mathcal{R}_2|}, \tag{3.4}$$

where \mathcal{R}_2 denotes a given set of indices representing the $M \times M$ local neighborhood of a pixel. Let $\mathbf{v}(\mathbf{s}) = [v_1(\mathbf{s}), v_2(\mathbf{s}), \dots, v_m(\mathbf{s})]^T$ denote the feature vector representing

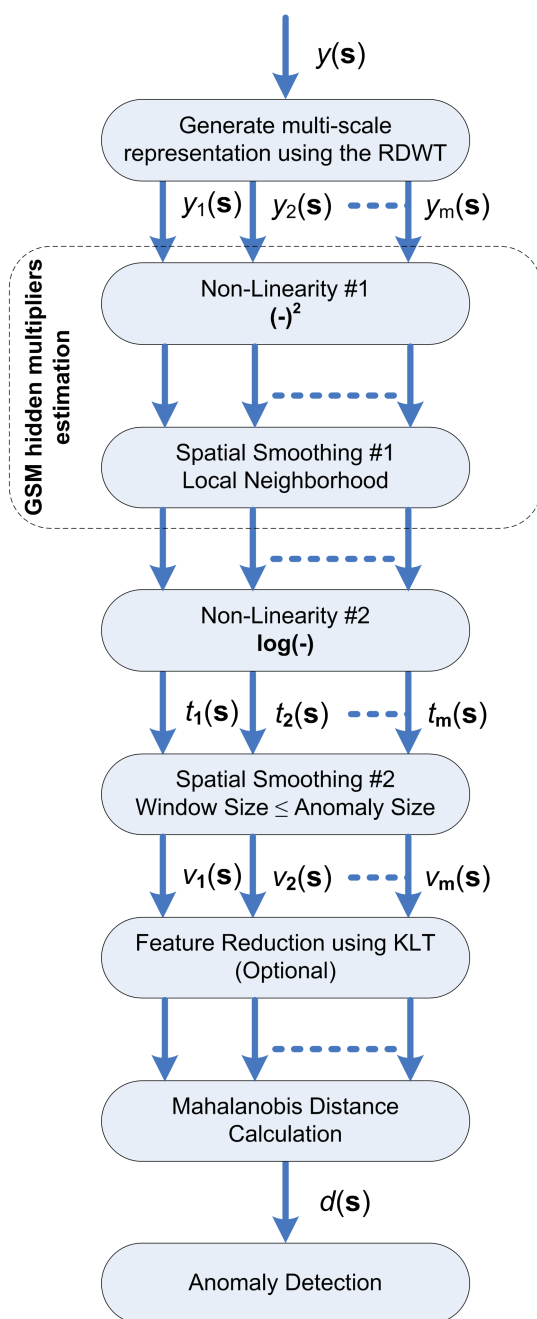


Figure 3.1: Block diagram of the proposed anomaly detection algorithm.

pixel $\mathbf{s} \in \Omega$. Let $\boldsymbol{\mu}_0$ and $\boldsymbol{\mu}_1$ denote the expectancy of the random feature vector $\mathbf{v}(\mathbf{s})$ under hypotheses H_0 and H_1 respectively. Let $\boldsymbol{\Sigma}_0$ and $\boldsymbol{\Sigma}_1$ denote the covariance matrix of the random feature vector $\mathbf{v}(\mathbf{s})$ under hypotheses H_0 and H_1 respectively. Following the assumption that the anomalous targets are rare and can be regarded as transients:

$$\begin{aligned}\hat{\boldsymbol{\mu}}_0 &\approx E[\mathbf{v}(\mathbf{s})] \\ \hat{\boldsymbol{\Sigma}}_0 &\approx E[(\mathbf{v}(\mathbf{s}) - \hat{\boldsymbol{\mu}}_0)(\mathbf{v}(\mathbf{s}) - \hat{\boldsymbol{\mu}}_0)^T].\end{aligned}\quad (3.5)$$

The Mahalanobis distance of the feature vector $\mathbf{v}(\mathbf{s})$ from $\boldsymbol{\mu}_0$ at pixel $\mathbf{s} \in \Omega$ is then given by [14]:

$$d(\mathbf{s}) = (\mathbf{v}(\mathbf{s}) - \boldsymbol{\mu}_0)^T \boldsymbol{\Sigma}_0^{-1} (\mathbf{v}(\mathbf{s}) - \boldsymbol{\mu}_0). \quad (3.6)$$

Following the SHT scheme, the decision rule for pixel $\mathbf{s} \in \Omega$ is defined as follows:

$$d(\mathbf{s}) \underset{H_0}{\overset{H_1}{\gtrless}} \eta, \quad (3.7)$$

where η is the threshold that determines if a given pixel $\mathbf{s} \in \Omega$ is regarded as an anomaly or background clutter. This decision rule is based on the statistics of the background clutter alone. Some *a priori* information regarding the minimum expected size of the targets can be utilized to determine M , thus improving the performance of the algorithm. The feature vector $\mathbf{v}(\mathbf{s})$ is a linear combination of Gaussian random vectors with dimension m [35, 43] and as such, it is also a Gaussian random vector. Since the covariance matrix $\boldsymbol{\Sigma}_0$ is a positive definite matrix, equation (3.6) can be formulated as follows:

$$d(\mathbf{s}) = \mathbf{z}(\mathbf{s})^T \mathbf{z}(\mathbf{s}), \quad (3.8)$$

where $\mathbf{z}(\mathbf{s}) \triangleq \boldsymbol{\Sigma}_0^{-1/2} (\mathbf{v}(\mathbf{s}) - \boldsymbol{\mu}_0)$. The random vector $\mathbf{z}(\mathbf{s})$ is distributed according to:

$$\begin{aligned} \mathbf{z}(\mathbf{s})|_{H_0} &\sim \mathcal{N}(\mathbf{0}, \mathbf{I}), \\ \mathbf{z}(\mathbf{s})|_{H_1} &\sim \mathcal{N}\left(\boldsymbol{\Sigma}_0^{-1/2}(\boldsymbol{\mu}_1 - \boldsymbol{\mu}_0), \boldsymbol{\Sigma}_0^{-1}\boldsymbol{\Sigma}_1\right). \end{aligned} \quad (3.9)$$

As such, the Mahalanobis distance under hypothesis H_0 is chi-square distributed with m degrees of freedom, regardless of the background clutter:

$$d(\mathbf{s})|_{H_0} \sim \chi_m^2(0). \quad (3.10)$$

The false alarm, as formulated in equation (3.2) is then given by:

$$P_{FA} = 1 - P(\chi_m^2(0) \leq \eta). \quad (3.11)$$

A special case is when under hypothesis H_1 the observations are assumed to be a linear combination of the target signature and the background clutter. The statistical distributions of the two hypotheses are therefore Gaussian with common covariance matrices (*i.e.*, $\boldsymbol{\Sigma}_0 = \boldsymbol{\Sigma}_1$) and different means. This yields a detection scheme similar to the RX algorithm [47]. In particular:

$$d(\mathbf{s})|_{H_1} \sim \chi_m^2(\lambda), \quad (3.12)$$

where $\lambda = (\boldsymbol{\mu}_1 - \boldsymbol{\mu}_0)^T \boldsymbol{\Sigma}_0^{-1} (\boldsymbol{\mu}_1 - \boldsymbol{\mu}_0)$. The detection rate, as formulated in equation (3.2) is then given by:

$$P_D = 1 - P(\chi_m^2(\lambda) \leq \eta). \quad (3.13)$$

When M is increased, the expectancies $\boldsymbol{\mu}_0$ and $\boldsymbol{\mu}_1$ remain the same. However, the variances of the marginal distributions under both hypotheses are reduced. The reduction factor is approximately equal for both background clutter and target anomaly whenever the size of the averaging window is greater than the maximum distance over which pixels are significantly correlated [65]. As a result, we expect that the detection

rate will be a monotone increasing function with the averaging window size M . Since a parametric form for P_D is not available for the general case, we have verified this on various Brodatz like textures [1]. An example is given in section 3.4.

3.4 Anomaly Detection Experimental Results

3.4.1 Performance Analysis

We have tested the proposed feature space on 40 Brodatz-like textures [1] using various averaging window sizes $1 \leq M \leq 40$ in order to verify the theory which states that the proposed feature space follows the Gaussian distribution and therefore conform to kurtosis value of 3. We have examined the influence of the averaging window size M on the performance of the proposed algorithm. We have observed that given any two textures from the Brodatz-like database [1], higher values of M leads to a better detection rate at a pre-determined false alarm rate. This is shown in Figure 3.2, using background and anomaly textures which appear different. Concurrent Receiver Operation Characteristics (ROC) curves are shown in Figure 3.3 (a). Figure 3.2 shows that the Mahalanobis distance indeed follows the chi-square distribution under hypotheses H_0 . Figure 3.3 (b) shows ROC curves for various window sizes, derived from background and anomaly textures having evident visual resemblance. This implies that M should be increased in order to achieve better performance, where the upper bound value is derived from the *a priori* information of the minimal expected size of the targets. This is demonstrated in Figure 3.6 using the image from Figure 3.7 (a).

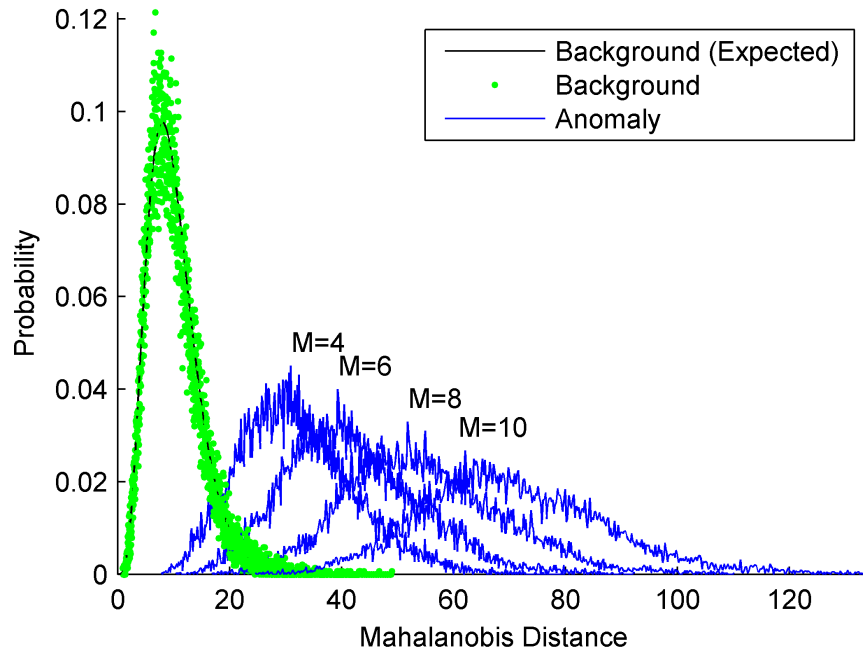
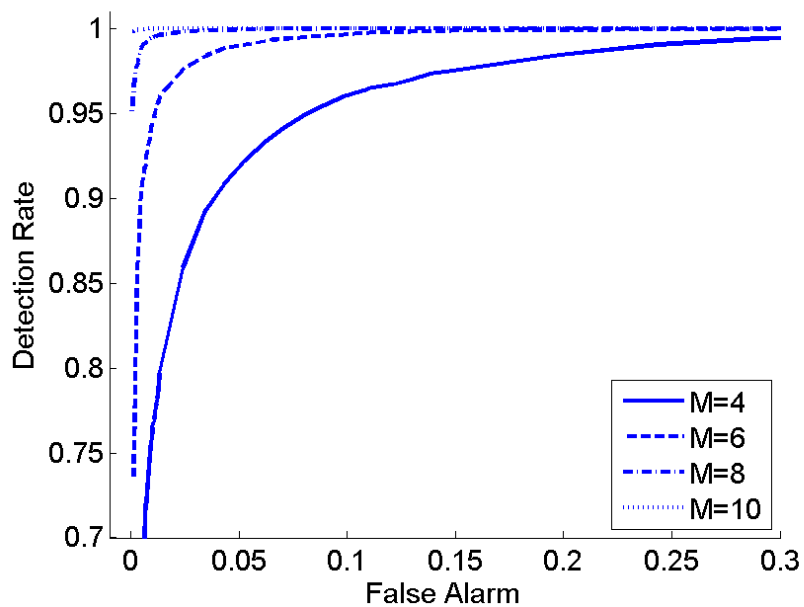


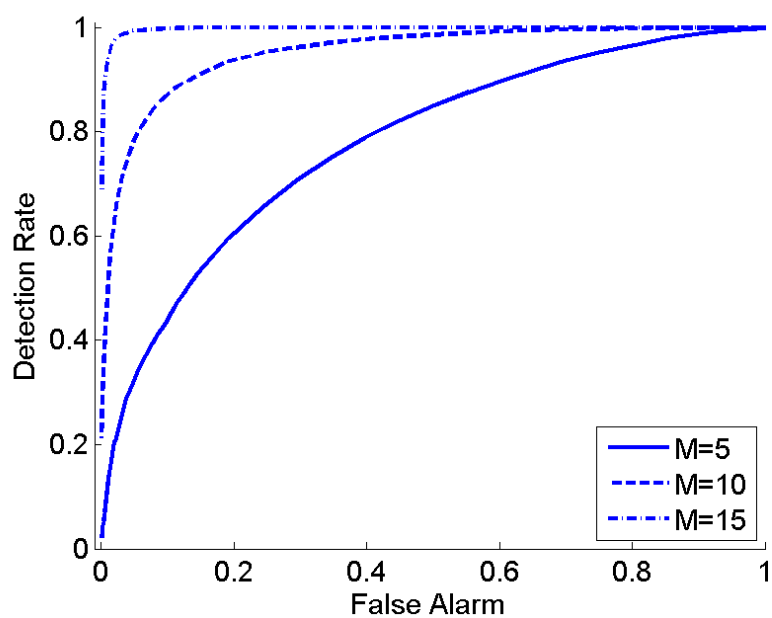
Figure 3.2: Mahalanobis distance calculation using a background clutter image and an anomaly image, both Brodatz like, for various values of M .

3.4.2 Anomaly Detection Examples

We have performed extensive testings of the proposed algorithm, using both real and synthesized images. Typical images are shown in Figure 3.7. The synthesized images were created using a set of Brodatz-like textures [1] that were used for both background clutter and anomalous targets. The anomalous targets were scaled to the same grey levels of the background clutter prior to insertion, rendering energy based detectors ineffective. In particular, we have studied two interesting cases: anomalous targets taken from textures which appear different from the background clutter and anomalous targets taken from textures which have evident visual resemblance to the background clutter. These cases are demonstrated in Figure 3.7 (a-b) with corresponding detection results in Figure 3.7 (d-e). It can be seen that the proposed algorithm detected the anomalies in both cases, in spite of the difficulty to locate



(a)



(b)

Figure 3.3: Calculated ROC curves using various values of M for: (a) Background and anomaly textures with no evident visual resemblance, presented in Figure 3.4. (b) Background and anomaly textures with evident visual resemblance, presented in Figure 3.5.

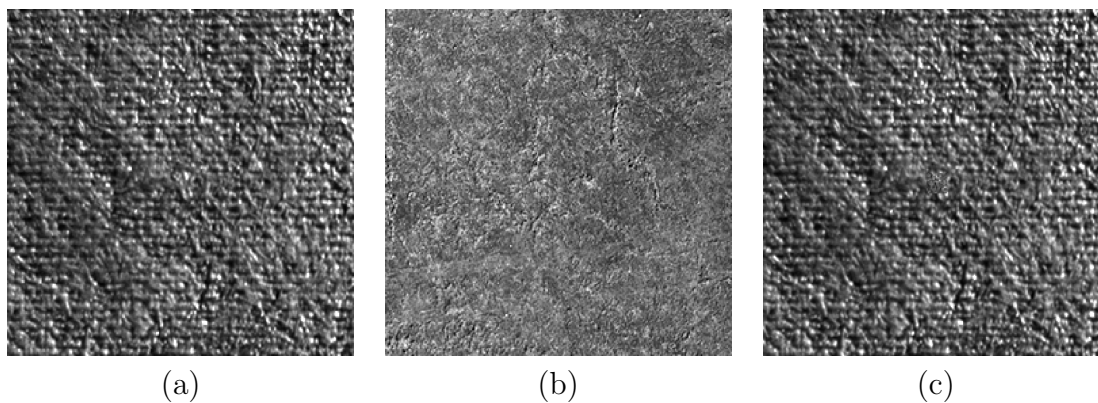


Figure 3.4: Background and anomaly textures with no evident visual resemblance. (a) Background texture. (b) Texture for anomaly. (c) Typical texture with anomaly. The anomaly is placed at the center of the background texture.

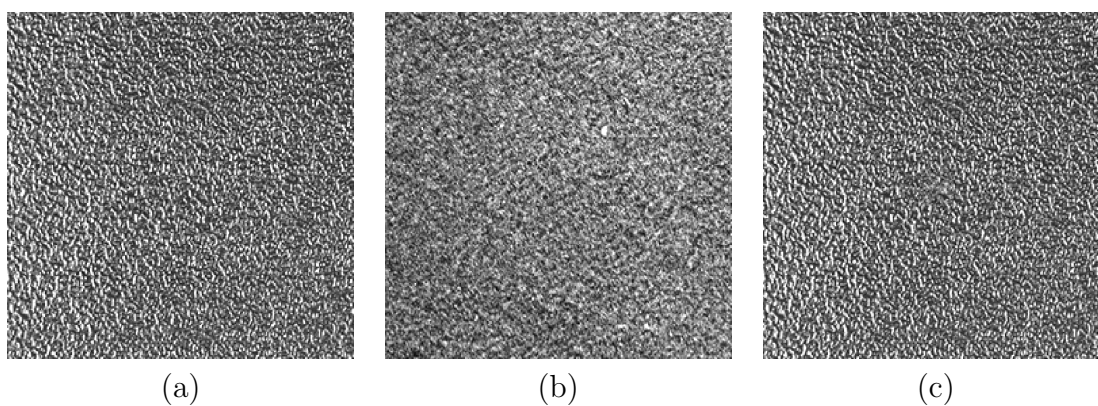


Figure 3.5: Background and anomaly textures with evident visual resemblance. (a) Background texture. (b) Texture for anomaly. (c) Typical texture with anomaly. The anomaly is placed at the center of the background texture.

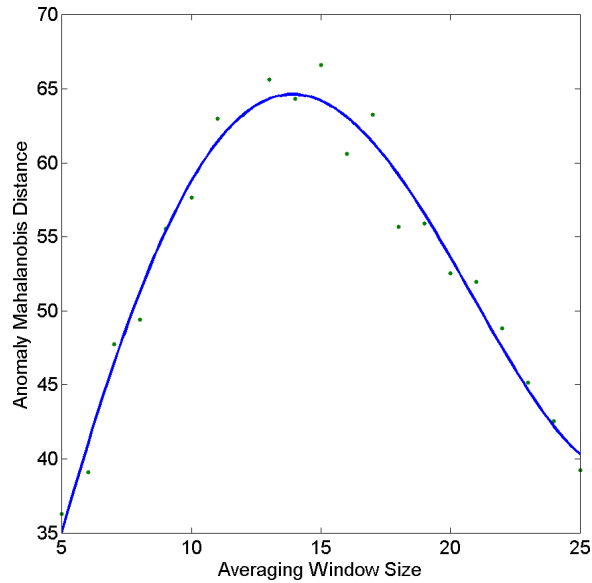


Figure 3.6: Mahalanobis distance under hypothesis H_1 for various values of the averaging window dimension M . The anomaly size is 15×15 pixels.

them when observing the images with the naked eye. For real image data, we have used the same set of sonar images that were used in [21]. The image shown in Figure 3.7 (c) is a good example for the volatility clustering phenomena that follows multi-resolution decompositions [39]. Nevertheless, it can be seen in Figure 3.7 (f) that this does not affect the detection of the sea-mine and produces no false alarms with proper thresholding of the calculated distance.

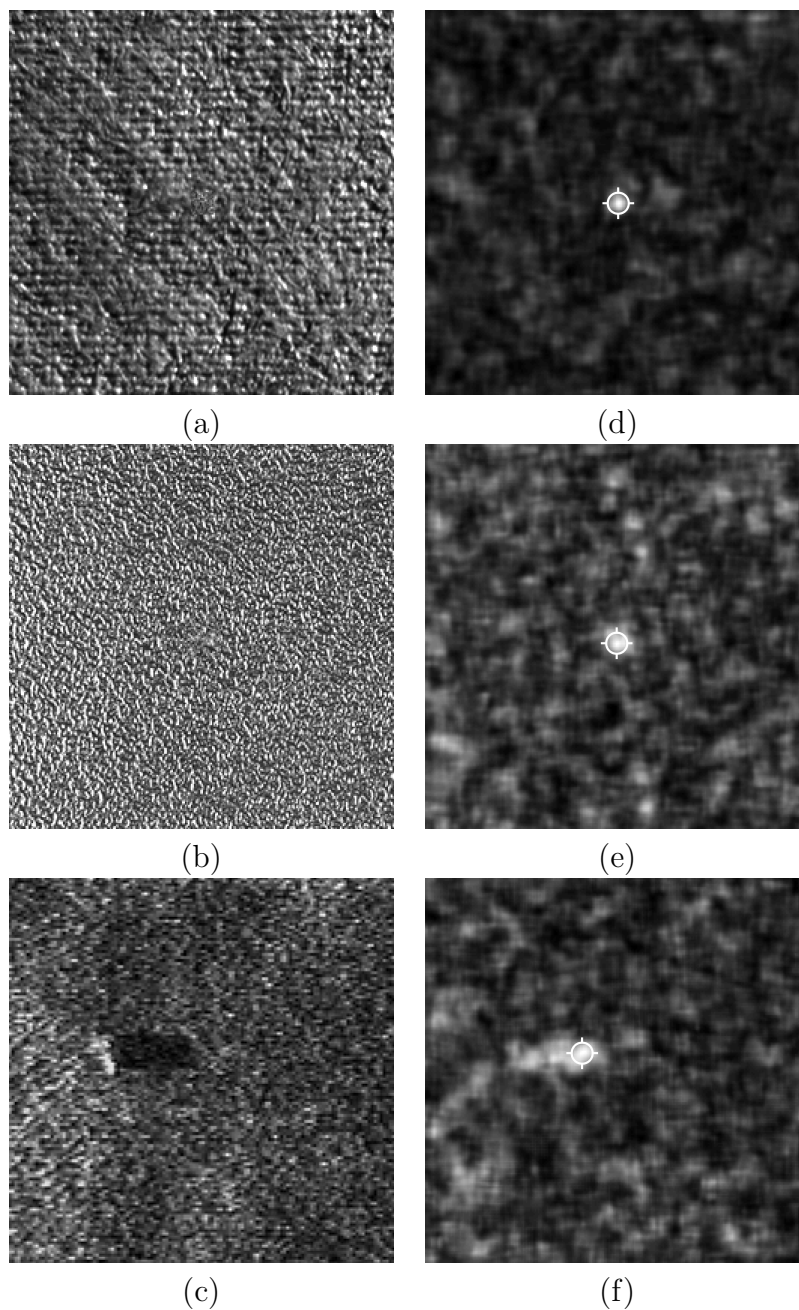


Figure 3.7: Anomaly detection examples. (a) Synthesized image with anomaly in its center, using textures not having evident visual resemblance. (b) Synthesized image with anomaly in its center, using textures having evident visual resemblance. (c) Real sonar image containing a sea-mine. (d)-(f) Corresponding detection results using $m = 10$, $N = 3$, $M = 15$. The white target mark is attached only to the highest value in each detection image.

3.5 Application to Texture Classification

The marginal variance $E[y_j(\mathbf{s})]$ is defined based on the multi-resolution decomposition filters and the spatial covariance associated with a given texture [65]. As such, different textures result in different variance values under the same multi-resolution decomposition. Therefore, the expectancy and covariance of the features $\mathbf{v}(\mathbf{s})$ (equation 3.5) provide a unique signature of the texture that was used to derive them. The Mahalanobis distance measure (equation 3.6) can then be used as a similarity measure from pre-trained textural signatures. A block diagram of the proposed classification algorithm is presented in Figure 3.8. We derive a set of textural signatures from a set of given distinct training textures. The Mahalanobis distance of a test texture can then be calculated from each training texture using the set of textural signatures. The test texture is then classified based on the minimal calculated distance. The performance of the proposed scheme was compared to recently published texture classification algorithm [36], as presented in Section 3.6.

3.6 Texture Classification Experimental Results

In [36], Mittelman and Porat used the MLE of the GSM hidden multipliers of wavelet coefficients in a texture classification scheme. Their algorithm was based on comparing the marginal distribution approximations (via spectral histograms) between different texture chips using a logarithmic scale of the histogram bin centers. The decision between several given textures was based upon the χ^2 similarity measure [30]. This measure was used to calculate the distance from pre-trained spectral histograms for each texture. In order to evaluate the ability of our proposed algorithm to distinguish between various textures, we have repeated the exact test scheme that is

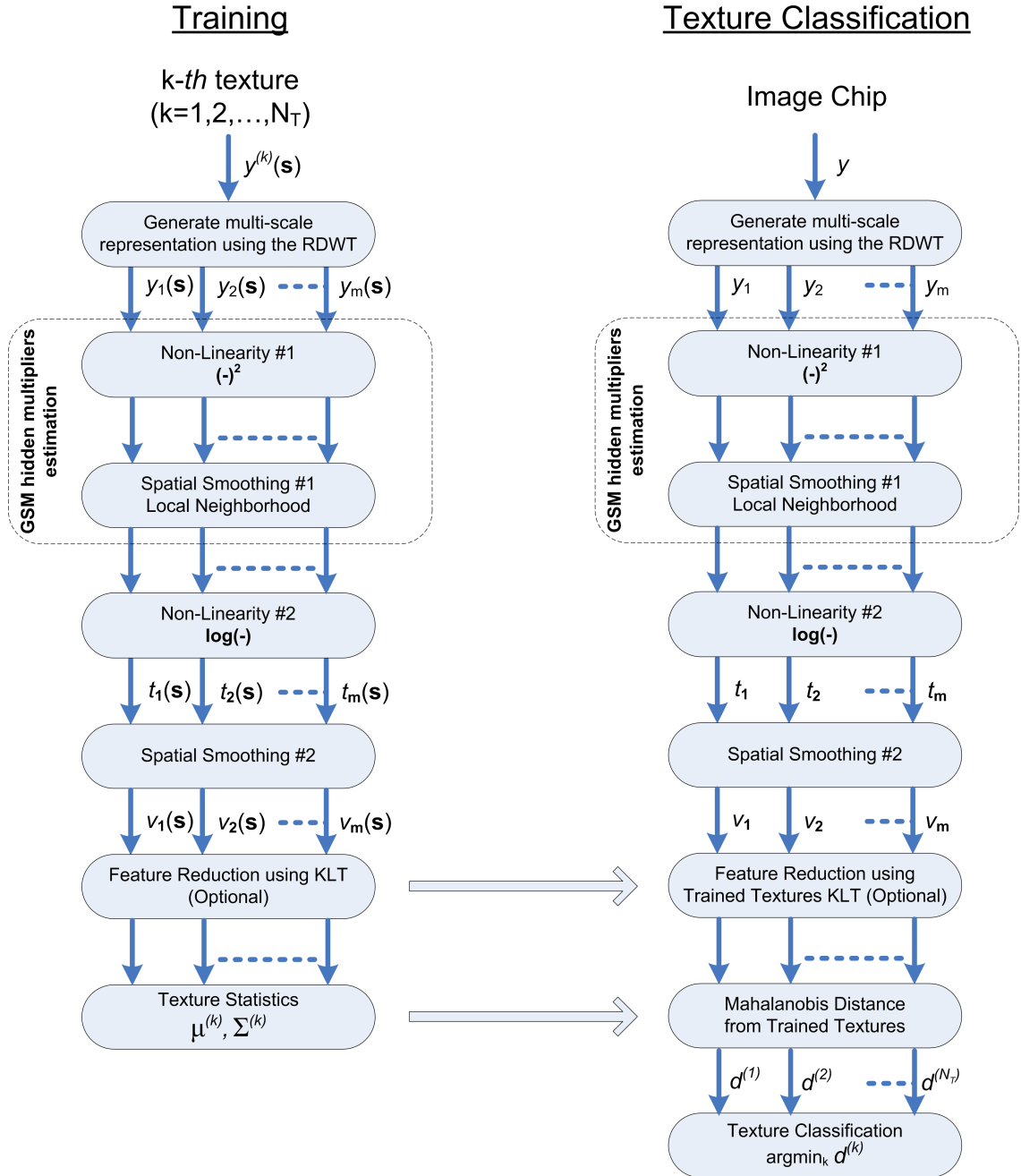


Figure 3.8: Block diagram of the proposed texture classification algorithm.

Table 3.1: Comparison of texture classification results

	Average [%]	Worst [%]	Best [%]	Std
Proposed	99.94	99.22	100.00	0.13
Mittelman & Porat	93.39	91.33	94.45	0.53
Mittelman & Porat [36]	93.74	92.03	95	NA
Liu & Wang [36]	92.5	NA	NA	NA

presented in [36] using both algorithms. The test was conducted using 40 Brodatz like textures [1] and was repeated 100 times to avoid the biasing of the results. We have set $m = 10$, $N = 3$, $M = 32$ and used only the top 5 principal components of the feature space of each texture. The results are summarized in table 3.1, showing that our proposed algorithm achieves better classification results. The results suggest that a better segmentation scheme could be achieved using a fusion of the presented textural features and Mittelman and Porat unsupervised segmentation algorithm [35, 37].

3.7 Enhancement of Detection

Based on equations (3.3) and (3.4), the resulting feature space of a scaled texture with scaling factor δ is given by:

$$v_j(\mathbf{s})^{(scaled)} = \log \delta^2 + v_j(\mathbf{s}) \quad (3.14)$$

and the additive bias $\log \delta^2$ is the same in all the feature space layers. Consequently, the expectancy follows:

$$E [v_j(\mathbf{s})^{(scaled)}] = \log \delta^2 + E [v_j(\mathbf{s})], \quad (3.15)$$

resulting in a chi-square distributed Mahalanobis distance:

$$d(\mathbf{s})|_{scaled} \sim \chi_m^2(\boldsymbol{\rho}^T \boldsymbol{\Sigma}_0^{-1} \boldsymbol{\rho}), \quad (3.16)$$

where $\boldsymbol{\rho} = [\log \delta^2, \log \delta^2, \dots, \log \delta^2]^T$. This implies that a scaled texture can be detected as an anomaly in an anomaly detection scheme or even misclassified in a texture classification scheme which are based on derived statistics from the unscaled version of the same texture. This issue can be overcome, if needed, in the following way. We define the normalized feature space $\mathbf{q}(\mathbf{s}) = [q_1(\mathbf{s}), q_2(\mathbf{s}), \dots, q_{m-1}(\mathbf{s})]^T$ as follows:

$$q_j(\mathbf{s}) = v_{j+1}(\mathbf{s}) + ([\boldsymbol{\mu}_0]_1 - v_1(\mathbf{s})), \quad (3.17)$$

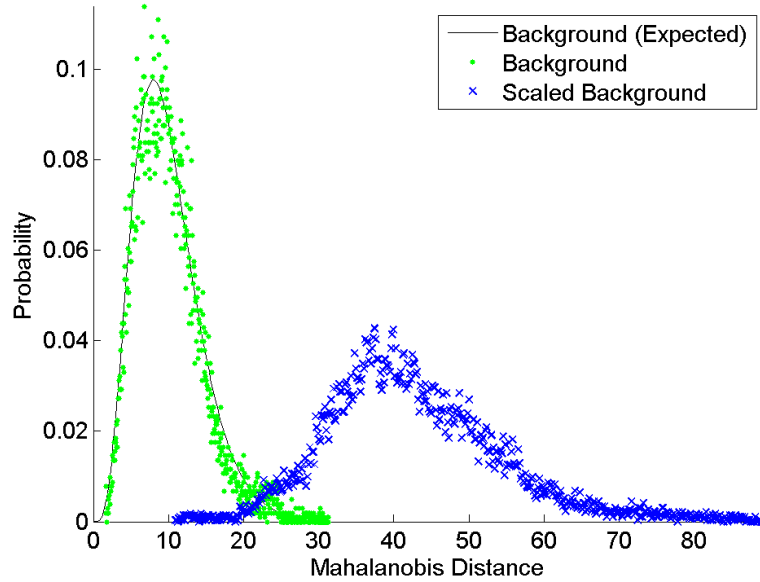
where $[\cdot]_1$ denotes the first element in a vector. In addition we define:

$$\begin{aligned} \boldsymbol{\mu}'_0 &= E[\mathbf{q}(\mathbf{s})] \\ \boldsymbol{\Sigma}'_0 &= E[(\mathbf{q}(\mathbf{s}) - \boldsymbol{\mu}'_0)(\mathbf{q}(\mathbf{s}) - \boldsymbol{\mu}'_0)^T]. \end{aligned} \quad (3.18)$$

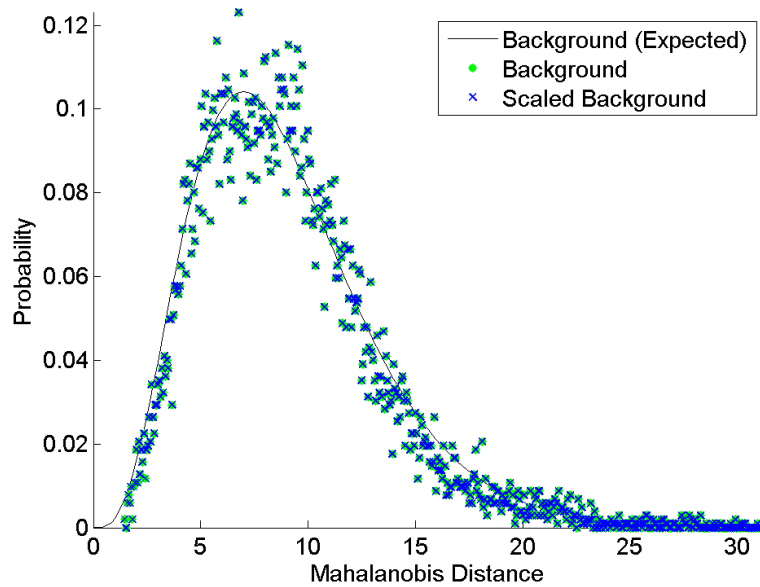
Based on equation (3.6), the Mahalanobis distance for pixel $\mathbf{s} \in \Omega$ is then given by:

$$d(\mathbf{s}) = (\mathbf{q}(\mathbf{s}) - \boldsymbol{\mu}'_0)^T \boldsymbol{\Sigma}'_0^{-1} (\mathbf{q}(\mathbf{s}) - \boldsymbol{\mu}'_0) \quad (3.19)$$

and the decision rule is defined in equation (3.7). Figure 3.9 demonstrates the Mahalanobis distance distribution of a scaled texture prior and after to the use of the proposed normalization, using the same texture as in Figure 3.4 (a). Prior to the use of the proposed normalization, the scaled texture would have been detected as an anomaly whether after the use of the proposed normalization the scaling is overlooked. To conclude, the proposed normalization allows for the detection of anomalous textures, taking into consideration the spatial structure of the texture rather than just derived energy measures.



(a)



(b)

Figure 3.9: Mahalanobis distance calculation using a background clutter image and an anomaly image. The anomaly image is a scaled version of the background image with a scale factor of $\delta = 2$. (a) Without normalization; The scaled background image is regarded as an anomaly. (b) With normalization; The scaled background image is not regarded as an anomaly. Calculation was performed using $m = 10$, $N = 3$, $M = 15$.

3.8 Summary

We have introduced a multi-resolution feature space and a corresponding unsupervised anomaly detection method. The proposed feature space is well modeled by the Gaussian distribution and therefore is appropriate for use with Bayesian classifiers. Our detection method is based on the SHT, thus it is not restricted to targets which follow a uniform model or reside in a characterizing subspace. The proposed scheme yields a detection algorithm which achieves improved detection results with CFAR. The proposed scheme can be applied to texture classification, achieving improved classification results.

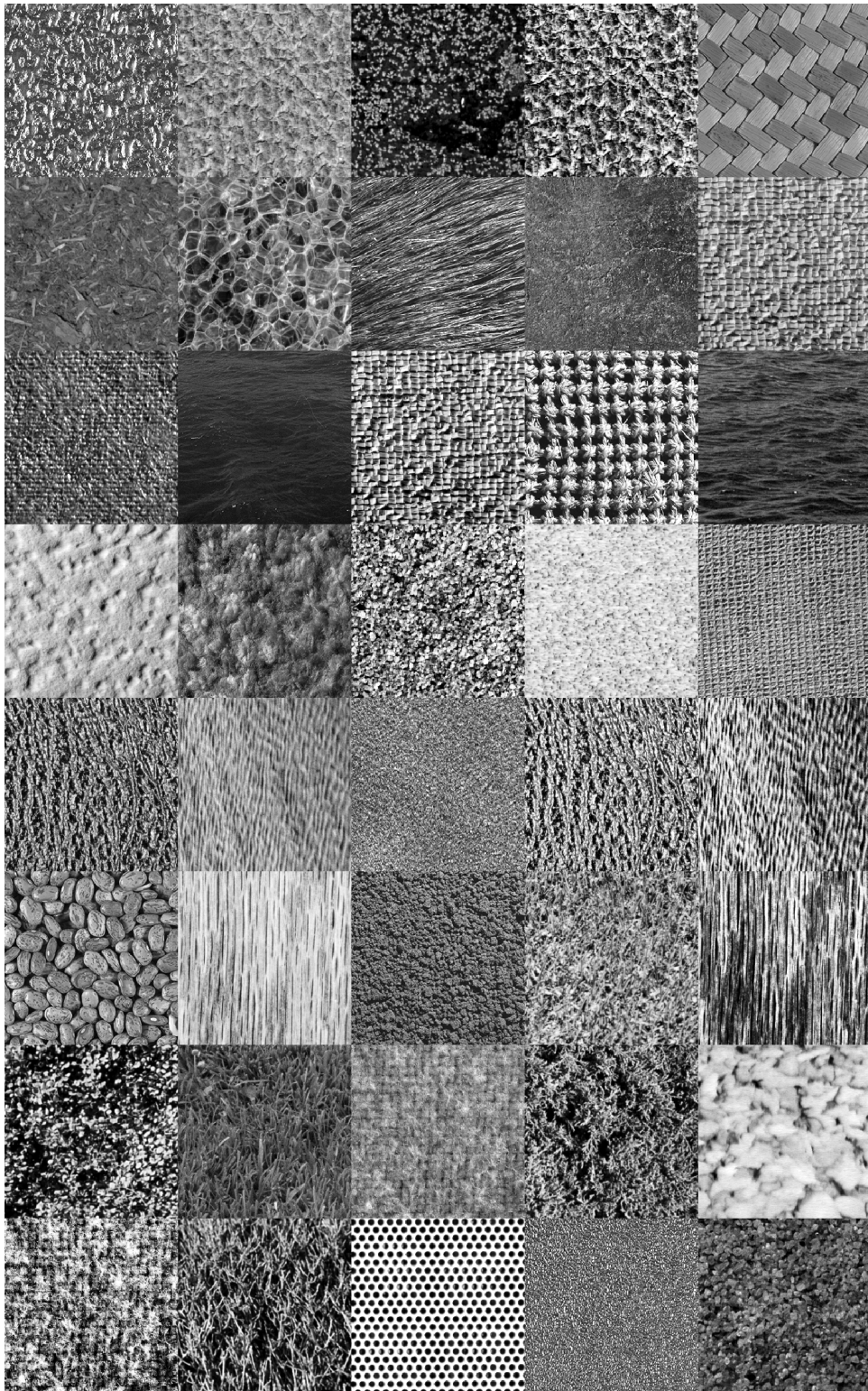


Figure 3.10: The Brodatz like textures that were used in our experiments.

Chapter 4

Anomaly Subspace Detection

Using Multi-Resolution Textural

Features

4.1 Introduction

Random field models, such as the Simultaneous Auto-Regressive (SAR) and the Gaussian Markov Random Field (GMRF), are widely employed in Bayesian frameworks for texture classification and anomaly detection. However, the consistency between these models and the true data is highly affected by the used neighborhood, which can differ between textures. This necessitate a proper selection of a neighbor set prior to texture modeling, affecting the robustness of GMRF based detection algorithms. The matched subspace detector (MSD) is a Bayesian classifier which assumes a multi-variate Gaussian model. The Gaussian assumption is a necessity since the theoretical

development and analysis of detection algorithms for arbitrary non-normal distributions, although highly desirable, is not mathematically traceable. Despite the fact that this assumption is rarely true when considering real data, MSD based detectors work well in many practical applications [32]. As an example, we consider the GMRF based algorithm presented in [22], where the MSD is performed on GMRF innovations that are derived from a multi-resolution representation of an image. Noibar and Cohen have shown in [39] that the GMRF normality assumption is inconsistent with the multi-resolution representation that was used in [22], leading to higher false alarms. Even when the MSD is employed upon the appropriate feature space, its theoretical detection performance is highly affected by two main parameters: target subspace dimensionality and signal to noise ratio (SNR). The detection performance improves with increasing SNR and decreasing subspace dimensionality.

We aim to formulate an MSD based anomaly detector, designated to detect additive anomalies in harsh environments where signal to noise energy ratio (SNER¹) values are very low. Obviously, the detector should account for and overcome these issues. For that purpose we introduce a non-casual random field model (RFM) that accounts for correlation between pixels which are not included in the neighbor set, moderating the need for proper choice of a neighborhood for each background texture. The proposed RFM captures the highly correlated spatial nature of the background clutter. We formulate a multi-resolution RFM, based on a multi-resolution representation of the image followed by a squaring non-linearity. Each layer is then modeled as an RFM with different sets of parameters, resulting in improved segregation of

¹The SNR and SNER definitions are not the same. Formulations are given in Section 4.5.

additive anomalies from their background surrounding. We then formulate an appropriate multi-resolution MSD for detecting additive subspace target signals in a background multi-resolution RFM noise environment with possible additive subspace interference signals. The proposed MSD takes into consideration the interaction between the background image and the *a priori* subspaces; a necessity due to the feature space that is being used. The MSD utilizes the correlation both within and between layers, allowing the detection process to be based on feature space data from adjacent layers of the multi-resolution representation. Since not all layers contribute evenly to the detection process, the multi-resolution MSD allows for a selection of the layers that shall be used. This selection can be made *a priori* or after some processing has been performed and intermediate results of the detection process are available. We have implemented the proposed algorithm and tested it on a large set of scenes containing Brodatz like background textures [1] in order to verify that our objectives are indeed fulfilled. The proposed algorithm outperformed two recently published competing methods [22, 55], achieving better detection results.

The organization of this chapter is as follows. In Section 4.2, we formulate the detection problem. In Section 4.3, we introduce an RFM which better describes a given image and a corresponding multi-resolution feature space. In Section 4.4, we present the proposed anomaly subspace detection algorithm. In Section 4.5, we analyze the performance of the proposed anomaly detection algorithm and compare the detection results to those obtained by using competing methods. We then demonstrate the application of the proposed algorithm to automatic target detection in both synthesized and real imagery. In Section 4.6, we define a scaling requirement for reducing the RFM prediction error, resulting in a better image representation than the

GMRF model. In Section 4.7, we define a scaling requirement for SNR improvement, resulting in a better detection scheme.

4.2 Problem Formulation - Additive Anomaly

Let $\Omega = \{\mathbf{v} : 1 \leq v_1 \leq M_1, 1 \leq v_2 \leq M_2\}$ be the support lattice for $\{y(\mathbf{v})\}_{\mathbf{v} \in \Omega}$ - the observations of an image containing a background natural texture, denoted as $x(\mathbf{v})$, with rare target and interference additive signals scattered around in the image, denoted as $h(\mathbf{v})$ and $g(\mathbf{v})$ respectively. The target and interference signals are assumed to be much smaller than the support lattice of the background image and therefor can be regarded as transients. We define two possible hypotheses for each pixel $\mathbf{v} \in \Omega$:

$$\begin{aligned} H_0 : \quad y(\mathbf{v}) &= x(\mathbf{v}) + g(\mathbf{v}), \\ H_1 : \quad y(\mathbf{v}) &= x(\mathbf{v}) + g(\mathbf{v}) + h(\mathbf{v}), \end{aligned} \tag{4.1}$$

where H_0 and H_1 represent the absence and presence of an anomalous target in the image respectively. The decision between H_0 and H_1 for every pixel $\mathbf{v} \in \Omega$ allows for the detection of target signals in the image observations $y(\mathbf{v})$, a process which can be regarded as the detection of undesired anomalies in a given image. The problem at hand is therefor to define an anomaly detection algorithm that achieves:

$$\begin{aligned} P_D &\triangleq P(H_1|H_1), \quad P_D \geq 1 - \epsilon_1, \\ P_{FA} &\triangleq P(H_1|H_0), \quad P_{FA} \leq \epsilon_2, \end{aligned} \tag{4.2}$$

for given values of ϵ_1 and ϵ_2 .

4.3 Statistical Model Formulation

4.3.1 Segregation Enhancement

Multi-resolution decompositions, such as the wavelet transform, are often used for feature extraction, better characterizing a given image than a single resolution analysis. These decompositions use a set of multi-scale bandpass oriented filters for decomposing the image, a process which is effective at decoupling high-order statistical features of natural images. In addition, it efficiently represents the visually relevant features of images [44]. The undecimated discrete wavelet transform is preferable to the standard decimated wavelet decomposition, mainly because it tends to decrease the variability of the estimated texture features, hence improving texture classification performance [64]. The undecimated discrete wavelet transform also results in a texture characterization invariant under texture translation. Here we utilize the RDWT for the purpose of generating a multi-resolution feature space. The RDWT, which is essentially an undecimated version of the discrete wavelet transform, was given tight energy bounds in [17] for 1-D signals:

$$2\|x\|^2 \leq \|X^{(J)}\|^2 \leq 2^J\|x\|^2, \quad (4.3)$$

where $x \in \ell^2(\mathbb{Z})$ is a $1 \times n$ 1-D signal and $X^{(J)}$ is the J-scale RDWT of x . When considering 2-D images, the bounding relationship between the image and its RDWT decomposition becomes:

$$4 \|\text{col}[x]\|^2 \leq \|\text{col}[X^{(J)}]\|^2 \leq 4^J \|\text{col}[x]\|^2, \quad (4.4)$$

where $x \in \ell^2(\mathbb{Z})$ is a $n \times n$ image, $X^{(J)}$ is the J-scale RDWT of x and $\text{col}[\cdot]$ stands for the column stack representation. The left part of the inequality in (4.4) implies

that additive energy in the RDWT domain will result in less additive energy in the original signal domain. This motivates image de-noising algorithms which operate in the RDWT domain, since the inverse RDWT provides substantial reduction of the noise variance. However, this also implies that improving the segregation between additive anomalies and a background image is better off in the RDWT domain rather than in the original image domain.

Unser and Eden explored in [65] several non-linearities and their effects on texture segmentation schemes. They have concluded that squaring, followed by averaging and then by a logarithm function, improves segmentation results. Mittelman and Porat [36] argued that those non-linearities, when applied to wavelet coefficients, result in a normally distributed feature space. Motivated by their work, we have formulated in [55] an RDWT based multi-resolution feature space and a corresponding single hypothesis testing anomaly detection scheme. We have used the same non-linearities, but with additional averaging step, which improved detection performance considerably. The multi-resolution feature space in [55] follows the multivariate Gaussian distribution. This suggests that it is suitable for use with an MSD, closely achieving theoretical detection performance. However, in practice, it degrades the segregation between additive anomalies and background clutter. This is due to the averaging stages and the influence of the logarithm on the variance of the feature space. Furthermore, the use of the logarithm limits the MSD in a way that makes it behave like a matched signal detector for a finite number of target signals.

The use of the squaring non-linearity by itself allows for a better segregation of additive anomalous targets from the background clutter. Furthermore, the use of the

squaring non-linearity results in a background clutter which can be modeled using an RFM more accurately. Appropriate subspaces for target and interference signals can be carefully formulated to be used with the MSD, which is linear by definition. We shall use the RDWT along with the squaring non-linearity in our feature space, as formulated in Section 4.3.3. Appropriate subspace formulation is given in Section 4.4.

4.3.2 Single Layer 2-D Random Field Model

The SAR and GMRF random field models, the later referred also as the conditional Markov (CM) model, are widely used in the literature for texture modeling and texture classification. These models were previously used for the purpose of anomaly detection [6, 22, 25, 48, 54], utilizing the anomalous appearance of target signals in a background clutter image with respect to the random field model which is tuned to best describe the image. Both models represent each pixel in a given image as a weighted sum of pixels at nearby locations and an additive prediction error, where the additive prediction error is often referred as the innovations process. The innovations process variance is smaller than the variance of the image. Both models assume a marginal Gaussian distribution for the derived innovations. However, under the SAR model those innovations are assumed to be uncorrelated, whereas under the GMRF model a specific correlation is defined in accordance with the Markovian assumption and the used weights. The Gaussian assumption allows these models to be used within a Bayesian classification framework.

In practice, the covariance of innovations which are derived from natural textures or from natural textures' wavelet coefficients does not necessarily follow the SAR or the GMRF models. This is mainly the result of inappropriate choice of neighborhood

to be used with a given image. Chellappa and Kashyap have shown in [10,26] that the quality of an image which is synthesized from its SAR or GMRF models varies considerably depending on the use of appropriate neighbor set, since different neighbor sets account for different textural patterns. Furthermore, correlation between image pixels is prone to change when a non-linearity is employed on the image, rendering it difficult to choose the appropriate set of neighboring pixels. The squaring non-linearity achieves an RFM with lower prediction error variance whenever a proper scaling of the modeled image is fulfilled (see Section 4.6). Yet, the resulting GMRF covariance differs from the actual covariance of the innovations. We demonstrate this in Figure 4.1, using the stone texture from Figure 1.1 (a). We observe that the GMRF covariance exhibits better resemblance to the actual innovations covariance when the squaring non-linearity is applied. In order to overcome this inconsistency, we formulate and use a more generic RFM, taking into consideration introduced correlation between pixels which are not accounted for in the GMRF model. This moderates the need for a proper choice of neighborhood for each background texture and yields a more robust detection algorithm when combined with the proposed squaring non-linearity.

The infinite lattice RFM for a stationary image $y(\mathbf{v})$ with a zero mean is given by:

$$y(\mathbf{v}) = \sum_{\mathbf{r} \in \mathcal{R}} \theta(\mathbf{r})y(\mathbf{v} + \mathbf{r}) + \varepsilon(\mathbf{v}), \quad (4.5)$$

where \mathcal{R} denotes a given set of indices representing the neighborhood of a pixel, $\theta(\mathbf{r})$ denotes the weight coefficient of a neighbor $\mathbf{r} \in \mathcal{R}$ and $\varepsilon(\mathbf{v})$ is an additive spatially correlated Gaussian noise sequence with zero mean and covariance $\mathbf{\Lambda}$. The weight coefficients $\{\theta(\mathbf{r})\}_{\mathbf{r} \in \mathcal{R}}$ and the innovations covariance $\mathbf{\Lambda}$ are unknown parameters that

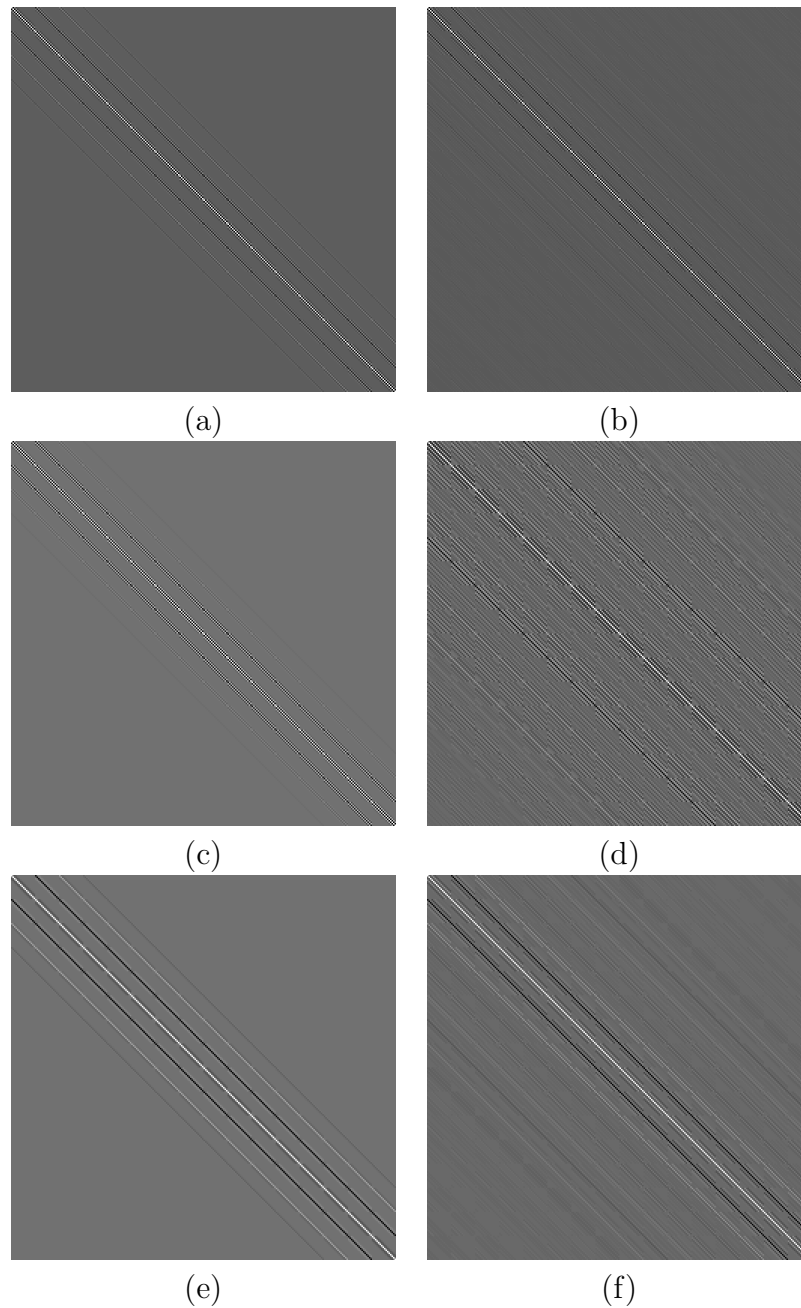


Figure 4.1: Innovations covariance example. GMRF (left column) vs. actual (right column). (a-b) Derived directly from the background texture. (c-d) Derived from a layer of wavelet coefficients. (e-f) Derived from the same layer of wavelet coefficients after applying the squaring non-linearity.

need to be estimated.

Let $\{y(\mathbf{v})\}_{\mathbf{v} \in \Omega}$ denote a finite stationary image, defined on a $M \times M$ toroidal lattice Ω . Equation (4.5) can then be rewritten as follows:

$$\mathbf{B}(\boldsymbol{\theta})\mathbf{y} = \boldsymbol{\varepsilon}, \quad (4.6)$$

where:

$$\begin{aligned} \mathbf{y} &= \text{col}[y(\mathbf{v}), \mathbf{v} \in \Omega], \\ \boldsymbol{\varepsilon} &= \text{col}[\boldsymbol{\varepsilon}(\mathbf{v}), \mathbf{v} \in \Omega], \\ \boldsymbol{\theta} &= \text{col}[\boldsymbol{\theta}(\mathbf{r}), \mathbf{r} \in \mathcal{R}] \end{aligned} \quad (4.7)$$

and $\text{col}[\cdot]$ stands for the column stack representation. The toroidal lattice determines the boundaries of the image such $y(\mathbf{v} + (M, M)) = y(\mathbf{v})$. The $M^2 \times M^2$ matrix $\mathbf{B}(\boldsymbol{\theta})$ is a block-circulant matrix which contains the weight coefficients. The neighborhood \mathcal{R} can be arbitrary as long as $(0, 0) \notin \mathcal{R}$ and the resulting block-circulant matrix $\mathbf{B}(\boldsymbol{\theta})$ is not singular. As such, we require:

$$\lambda(\mathbf{v}, \boldsymbol{\theta}) = 1 - \sum_{\mathbf{r} \in \mathcal{R}} \theta(\mathbf{r}) \cos\left(r_1 \frac{2\pi v_1}{M} + r_2 \frac{2\pi v_2}{M}\right) \neq 0, \quad \forall \mathbf{v} \in \Omega, \quad (4.8)$$

where $\lambda(\mathbf{v}, \boldsymbol{\theta})$ denote the eigenvalues of matrix $\mathbf{B}(\boldsymbol{\theta})$ [9, 23], $\mathbf{v} = (v_1, v_2)$ and $\mathbf{r} = (r_1, r_2)$. A symmetric neighborhood \mathcal{R} results in a symmetric matrix $\mathbf{B}(\boldsymbol{\theta})$ as well.

The problem of estimating the parameters of the SAR and the GMRF models was previously addressed in the literature [22, 24–26, 35, 53] and various solutions were proposed. A computationally efficient method for estimating the weight coefficients is derived using the LS approach. The weight coefficients LSE is given by [26, 53]:

$$\hat{\boldsymbol{\theta}} = \left[\sum_{\mathbf{v} \in \Omega} \mathbf{w}(\mathbf{v})\mathbf{w}(\mathbf{v})^T \right]^{-1} \left[\sum_{\mathbf{v} \in \Omega} y(\mathbf{v})\mathbf{w}(\mathbf{v}) \right], \quad (4.9)$$

where:

$$\mathbf{w}(\mathbf{v}) = \text{col} [y(\mathbf{v} + \mathbf{r}), \mathbf{r} \in \mathcal{R}]. \quad (4.10)$$

Based on equation (4.9), the estimated weight coefficients are not affected by the marginal variance of the image, but rather on the spatial interaction between neighboring pixels. The covariance $\mathbf{\Lambda}$ is then given by:

$$\mathbf{\Lambda} = E [\boldsymbol{\varepsilon}\boldsymbol{\varepsilon}^T] \approx \mathbf{B}(\hat{\boldsymbol{\theta}})\boldsymbol{\Sigma}\mathbf{B}(\hat{\boldsymbol{\theta}})^T, \quad (4.11)$$

where $\boldsymbol{\Sigma} = E [\mathbf{y}\mathbf{y}^T]$.

Conventional random field models, such as the SAR, GMRF and the proposed RFM, are intended to be used with micro-textures. As such, these models may not sufficiently describe the background clutter in images with periodical patterns of period lengths larger than the neighborhood \mathcal{R} . However, they should be appropriate for most, if not all, multi-resolution decomposition layers of such images [22].

4.3.3 Multi-Resolution Feature Space

Let Ω be the $M \times M$ support lattice for a mean normalized image $\{y(\mathbf{v})\}_{\mathbf{v} \in \Omega}$. Let $\{y_j(\mathbf{v})\}_{j=1, \dots, m}$ denote the j th layer wavelet coefficients obtained from the image using an RDWT with $(m-1)/3$ levels. Let $\mathbf{y}(\mathbf{v})$ denote the resulting multi-resolution image with m layers. The multi-resolution image $\mathbf{y}(\mathbf{v})$ is defined over the same support as image $y(\mathbf{v})$ and is given by:

$$\mathbf{y}(\mathbf{v}) = [y_1(\mathbf{v}), y_2(\mathbf{v}), \dots, y_m(\mathbf{v})]^T. \quad (4.12)$$

The wavelet coefficients at different layers are nearly de-correlated for most images and the transform can be thought of as an approximation for the Karhunen-Loéve

transform (KLT) [31]. We utilize the KLT as a mean for reducing the feature space, using only relevant layers in the detection scheme. Let \mathbf{K} denote a matrix whose columns are p eigenvectors taken from the covariance matrix of $\mathbf{y}(\mathbf{v})$, $\forall \mathbf{v} \in \Omega$. The KLT result, denoted as $\mathbf{t}(\mathbf{v})$, is given by:

$$\mathbf{t}(\mathbf{v}) = \mathbf{K}^T \mathbf{y}(\mathbf{v}) = [t_1(\mathbf{v}), t_2(\mathbf{v}), \dots, t_p(\mathbf{v})]^T, \quad 1 \leq p \leq m, \quad (4.13)$$

where $\{t_k(\mathbf{v})\}_{k=1, \dots, p}$ denote the generated uncorrelated image layers. The resulting local energy measures, denoted as $\mathbf{z}(\mathbf{v})$, are given by:

$$\mathbf{z}(\mathbf{v}) = [z_1(\mathbf{v}), z_2(\mathbf{v}), \dots, z_p(\mathbf{v})]^T, \quad (4.14)$$

where:

$$z_k(\mathbf{v}) = t_k^2(\mathbf{v}), \quad k = 1, \dots, p. \quad (4.15)$$

We assume that each layer in $\mathbf{z}(\mathbf{v})$ is statistically homogeneous and follows the 2-D RFM. Therefore, the k th layer satisfies (equation 4.5):

$$z_k(\mathbf{v}) - \mu_{z_k} = \sum_{\mathbf{r} \in \mathcal{R}} \theta_k(\mathbf{r}) [z_k(\mathbf{v} + \mathbf{r}) - \mu_{z_k}] + \varepsilon_k(\mathbf{v}), \quad (4.16)$$

where \mathcal{R} denotes the neighborhood, $\theta_k(\mathbf{r})$ denote the weight coefficients, μ_{z_k} denotes the expectancy of $z_k(\mathbf{v})$ and $\varepsilon_k(\mathbf{v})$ denotes the resulting innovations process. By applying the 2-D RFM to all layers, using model parameters which are estimated for each layer separately, we produce a multi-resolution RFM. The multi-resolution RFM innovations, denoted as $\boldsymbol{\varepsilon}(\mathbf{v})$, are then given by:

$$\begin{aligned} \boldsymbol{\varepsilon}(\mathbf{v}) &= [\varepsilon_1(\mathbf{v}), \varepsilon_2(\mathbf{v}), \dots, \varepsilon_p(\mathbf{v})]^T \\ &= \left(\mathbf{z}(\mathbf{v}) - \sum_{\mathbf{r} \in \mathcal{R}} \boldsymbol{\Theta}(\mathbf{r}) \mathbf{z}(\mathbf{v} + \mathbf{r}) \right) - \left(\mathbf{I} - \sum_{\mathbf{r} \in \mathcal{R}} \boldsymbol{\Theta}(\mathbf{r}) \right) \boldsymbol{\mu}, \end{aligned} \quad (4.17)$$

where:

$$\boldsymbol{\mu} \triangleq [\mu_{z_1}, \mu_{z_2}, \dots, \mu_{z_p}]^T, \quad (4.18)$$

$$\boldsymbol{\Theta}(\mathbf{r}) \triangleq \text{diag}(\theta_1(\mathbf{r}), \theta_2(\mathbf{r}), \dots, \theta_p(\mathbf{r})). \quad (4.19)$$

We shall use the multi-resolution RFM innovations, formulated in equation (4.17), as the feature space of the proposed anomaly detection algorithm.

4.4 Anomaly Detection Algorithm

In [52], Scharf and Friedlander introduced the MSD, formulating a class of problems for detecting subspace signals in subspace interference and broadband white Gaussian noise and laying the framework for detecting anomalies which are assumed to lie within a known subspace. Kraut *et. al.* [28] formulated an MSD for detecting subspace signals in colored Gaussian noise with a known covariance structure. Goldman and Cohen [22] have further improved the MSD scheme and formulated a multi-resolution MSD for the detection of subspace signals in subspace interference and colored Gaussian noise with a known covariance structure, corresponding to the GMRF innovations. Here we develop a multi-resolution MSD for detecting subspace signals in subspace interference and colored Gaussian noise, corresponding to the multi-resolution RFM innovations that were presented in Section 4.3.3.

A block diagram of the proposed algorithm is presented in Figure 4.2. Let $\{y(\mathbf{v}, \mathbf{s})\}_{\mathbf{s} \in \Omega_0}$ denote a $N \times N$ image chip, taken from image $\{y(\mathbf{v})\}_{\mathbf{v} \in \Omega}$ around the spatial location \mathbf{v} . Each image chip is comprised differently under hypotheses H_0 and

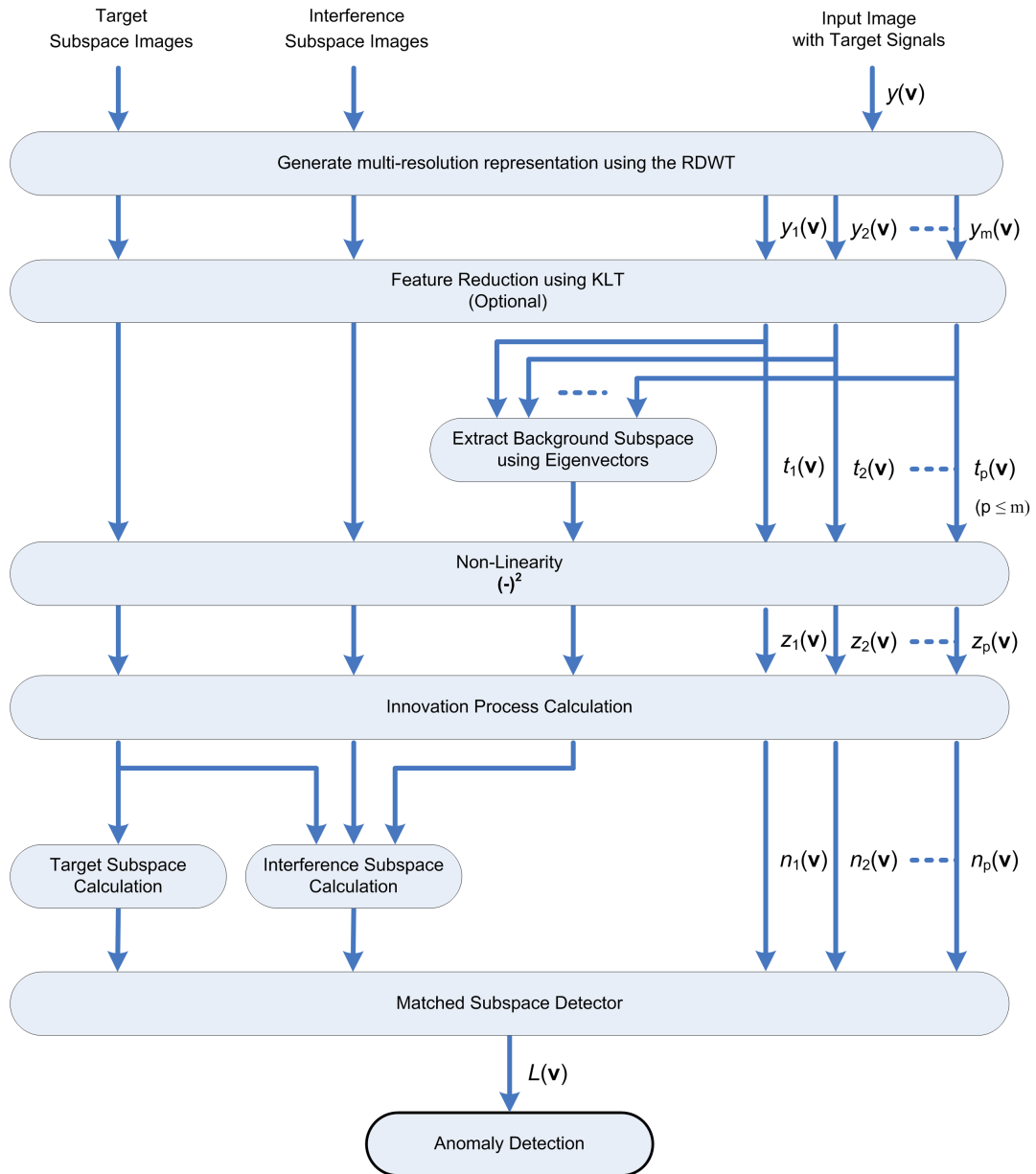


Figure 4.2: Block diagram of the proposed anomaly detection algorithm.

H_1 as follows:

$$\begin{aligned} H_0 : \quad y(\mathbf{v}, \mathbf{s}) &= x(\mathbf{v}, \mathbf{s}) + g(\mathbf{v}, \mathbf{s}), \\ H_1 : \quad y(\mathbf{v}, \mathbf{s}) &= x(\mathbf{v}, \mathbf{s}) + g(\mathbf{v}, \mathbf{s}) + h(\mathbf{v}, \mathbf{s}), \end{aligned} \tag{4.20}$$

where $x(\mathbf{v}, \mathbf{s})$, $g(\mathbf{v}, \mathbf{s})$ and $h(\mathbf{v}, \mathbf{s})$ are the image chips of the background clutter, interference signal and target signal respectively, around the spatial location \mathbf{v} . We assume that the chip $x(\mathbf{v}, \mathbf{s})$ conforms to a multi-resolution RFM with model parameters that were derived from the whole image. We further assume that the chip size is sufficient for containing the innovations of shapes which span the target and interference signals, taking into consideration RDWT and RFM margins. Therefore, the multi-resolution chip decomposition, denoted as $\mathbf{y}(\mathbf{v}, \mathbf{s})$, is comprised differently under hypotheses H_0 and H_1 as follows:

$$\begin{aligned} H_0 : \quad \mathbf{y}(\mathbf{v}, \mathbf{s}) &= \mathbf{x}(\mathbf{v}, \mathbf{s}) + \mathbf{g}(\mathbf{v}, \mathbf{s}), \\ H_1 : \quad \mathbf{y}(\mathbf{v}, \mathbf{s}) &= \mathbf{x}(\mathbf{v}, \mathbf{s}) + \mathbf{g}(\mathbf{v}, \mathbf{s}) + \mathbf{h}(\mathbf{v}, \mathbf{s}), \end{aligned} \tag{4.21}$$

where $\mathbf{x}(\mathbf{v}, \mathbf{s})$, $\mathbf{g}(\mathbf{v}, \mathbf{s})$ and $\mathbf{h}(\mathbf{v}, \mathbf{s})$ are the multi-resolution chip decompositions of the background clutter, interference signal and target signal respectively. Let $z_k(\mathbf{v}, \mathbf{s})$ denote the chip's k th layer local energy measures. $z_k(\mathbf{v}, \mathbf{s})$ is comprised differently under hypotheses H_0 and H_1 as follows:

$$\begin{aligned} H_0 : \quad z_k(\mathbf{v}, \mathbf{s}) &= t_k^2(\mathbf{x}(\mathbf{v}, \mathbf{s})) + t_k^2(\mathbf{g}(\mathbf{v}, \mathbf{s})) + 2 t_k(\mathbf{x}(\mathbf{v}, \mathbf{s})) t_k(\mathbf{g}(\mathbf{v}, \mathbf{s})), \\ H_1 : \quad z_k(\mathbf{v}, \mathbf{s}) &= t_k^2(\mathbf{x}(\mathbf{v}, \mathbf{s})) + t_k^2(\mathbf{g}(\mathbf{v}, \mathbf{s})) + 2 t_k(\mathbf{x}(\mathbf{v}, \mathbf{s})) t_k(\mathbf{g}(\mathbf{v}, \mathbf{s})) \\ &\quad + t_k^2(\mathbf{h}(\mathbf{v}, \mathbf{s})) + 2 t_k(\mathbf{x}(\mathbf{v}, \mathbf{s})) t_k(\mathbf{h}(\mathbf{v}, \mathbf{s})) + 2 t_k(\mathbf{g}(\mathbf{v}, \mathbf{s})) t_k(\mathbf{h}(\mathbf{v}, \mathbf{s})), \end{aligned} \tag{4.22}$$

where $t_k(\cdot) = [\mathbf{t}(\cdot)]_k$ and:

$$\begin{aligned}\mathbf{t}(\mathbf{x}(\mathbf{v}, \mathbf{s})) &= \mathbf{K}^T \mathbf{x}(\mathbf{v}, \mathbf{s}), \\ \mathbf{t}(\mathbf{g}(\mathbf{v}, \mathbf{s})) &= \mathbf{K}^T \mathbf{g}(\mathbf{v}, \mathbf{s}), \\ \mathbf{t}(\mathbf{h}(\mathbf{v}, \mathbf{s})) &= \mathbf{K}^T \mathbf{h}(\mathbf{v}, \mathbf{s}).\end{aligned}\tag{4.23}$$

Let $\mathbf{n}_k(\mathbf{v})$ denote the column stack representation of the chip's k th layer RFM innovations. Let $\mathbf{z}_k(\mathbf{v})$ denote the column stack representation of $z_k(\mathbf{v}, \mathbf{s})$, the chip's k th layer local energy measures. Based on equations (4.6), (4.7) and (4.16), $\mathbf{n}_k(\mathbf{v})$ is given by:

$$\mathbf{n}_k(\mathbf{v}) = \mathcal{D}_k \mathbf{z}_k(\mathbf{v}) - \mu_{z_k} \left(1 - \sum_{\mathbf{r} \in \mathcal{R}} \theta_k(\mathbf{r}) \right),\tag{4.24}$$

where $\mathcal{D}_k \triangleq \mathbf{B}(\theta_k(\mathbf{r}))$. Based on equation (4.22), $\mathbf{z}_k(\mathbf{v})$ and consequently $\mathcal{D}_k \mathbf{z}_k(\mathbf{v})$ contain derived components from the background texture, interference signals, target signals and the interaction among them. Hence, proper formulation of an MSD will allow the detection of target signals within $\mathbf{n}_k(\mathbf{v})$.

Let $\{h^{(l)}(\mathbf{s})\}_{s \in \Omega_0, l=1, \dots, u_h}$ and $\{g^{(l)}(\mathbf{s})\}_{s \in \Omega_0, l=1, \dots, u_g}$ denote sets of orthogonal image chips which span the target and interference signals respectively.

Let $\{x_j^{(l)}(\mathbf{s})\}_{s \in \Omega_0, l=1, \dots, u_x}$ denote a set of image chips which characterize the j th layer of the background natural texture multi-resolution decomposition; we have used u_x significant eigenvectors, derived from the estimated covariance matrix of a j th layer chip. Let $\mathbf{h}^{(l)}(\mathbf{s})$ and $\mathbf{g}^{(l)}(\mathbf{s})$ denote the multi-resolution chip decomposition of $h^{(l)}(\mathbf{s})$ and $g^{(l)}(\mathbf{s})$ respectively and let $\mathbf{x}^{(l)}(\mathbf{s}) = [x_1^{(l)}(\mathbf{s}), x_2^{(l)}(\mathbf{s}), \dots, x_m^{(l)}(\mathbf{s})]^T$. We define $\langle \mathcal{A}_k \rangle$ and $\langle \mathcal{B}_k \rangle$ as the k th layer MSD subspaces, each spanned by the columns of the full-rank matrices \mathcal{A}_k and \mathcal{B}_k respectively [52]. We define $\boldsymbol{\gamma}_k(\mathbf{v})$ as the whitened measurements,

derived from $\mathbf{n}_k(\mathbf{v})$ as follows:

$$\boldsymbol{\gamma}_k(\mathbf{v}) = \boldsymbol{\Lambda}_k^{-1/2} \mathbf{n}_k(\mathbf{v}), \quad (4.25)$$

where under the assumption of sparsely placed target signals and interfering signals:

$$\boldsymbol{\Lambda}_k \approx E [\mathbf{n}_k(\mathbf{v}) \mathbf{n}_k(\mathbf{v})^T]. \quad (4.26)$$

Based on equations (4.24) and (4.25), $\boldsymbol{\gamma}_k(\mathbf{v})$ is formulated under hypotheses H_0 and H_1 as follows:

$$\begin{aligned} H_0 : \quad \boldsymbol{\gamma}_k(\mathbf{v}) &= \mathcal{A}_k \boldsymbol{\phi}_k(\mathbf{v}) + \boldsymbol{\varepsilon}_k(\mathbf{v}), \\ H_1 : \quad \boldsymbol{\gamma}_k(\mathbf{v}) &= \mathcal{B}_k \boldsymbol{\psi}_k(\mathbf{v}) + \mathcal{A}_k \boldsymbol{\phi}_k(\mathbf{v}) + \boldsymbol{\varepsilon}_k(\mathbf{v}), \end{aligned} \quad (4.27)$$

where $\boldsymbol{\varepsilon}_k(\mathbf{v})$ denotes the whitened RFM innovations which are derived from the chip's background texture and $\boldsymbol{\phi}_k(\mathbf{v})$ and $\boldsymbol{\psi}_k(\mathbf{v})$ are the coordinates of the interference and target signals components with respect to subspaces \mathcal{A}_k and \mathcal{B}_k respectively.

Based on equations (4.22) and (4.27), the interfering subspace \mathcal{A}_k should account for the interfering signals, the interaction among them and the interaction between them and the background clutter. Therefore, subspace \mathcal{A}_k is comprised of:

$$\begin{aligned} [& \boldsymbol{\Lambda}_k^{-1/2} \mathcal{D}_k \boldsymbol{\alpha}_k(\mathbf{g}^{(1)}(\mathbf{s})), & \dots & \boldsymbol{\Lambda}_k^{-1/2} \mathcal{D}_k \boldsymbol{\alpha}_k(\mathbf{g}^{(u_g)}(\mathbf{s})), \\ & \boldsymbol{\Lambda}_k^{-1/2} \mathcal{D}_k \boldsymbol{\beta}_k(\mathbf{g}^{(1)}(\mathbf{s}), \mathbf{g}^{(2)}(\mathbf{s})), & \dots & \boldsymbol{\Lambda}_k^{-1/2} \mathcal{D}_k \boldsymbol{\beta}_k(\mathbf{g}^{(1)}(\mathbf{s}), \mathbf{g}^{(u_g)}(\mathbf{s})), \\ & \vdots & & \vdots \\ & \boldsymbol{\Lambda}_k^{-1/2} \mathcal{D}_k \boldsymbol{\beta}_k(\mathbf{g}^{(u_g-2)}(\mathbf{s}), \mathbf{g}^{(u_g-1)}(\mathbf{s})), & \dots & \boldsymbol{\Lambda}_k^{-1/2} \mathcal{D}_k \boldsymbol{\beta}_k(\mathbf{g}^{(u_g-2)}(\mathbf{s}), \mathbf{g}^{(u_g)}(\mathbf{s})), \\ & \boldsymbol{\Lambda}_k^{-1/2} \mathcal{D}_k \boldsymbol{\beta}_k(\mathbf{g}^{(u_g-1)}(\mathbf{s}), \mathbf{g}^{(u_g)}(\mathbf{s})), & & \\ & \boldsymbol{\Lambda}_k^{-1/2} \mathcal{D}_k \boldsymbol{\beta}_k(\mathbf{g}^{(1)}(\mathbf{s}), \mathbf{x}^{(1)}(\mathbf{s})), & \dots & \boldsymbol{\Lambda}_k^{-1/2} \mathcal{D}_k \boldsymbol{\beta}_k(\mathbf{g}^{(u_g)}(\mathbf{s}), \mathbf{x}^{(1)}(\mathbf{s})), \\ & \vdots & & \vdots \\ & \boldsymbol{\Lambda}_k^{-1/2} \mathcal{D}_k \boldsymbol{\beta}_k(\mathbf{g}^{(1)}(\mathbf{s}), \mathbf{x}^{(u_x)}(\mathbf{s})), & \dots & \boldsymbol{\Lambda}_k^{-1/2} \mathcal{D}_k \boldsymbol{\beta}_k(\mathbf{g}^{(u_g)}(\mathbf{s}), \mathbf{x}^{(u_x)}(\mathbf{s})) &], \end{aligned} \quad (4.28)$$

where $\boldsymbol{\alpha}_k(\cdot)$ is the column stack representation of $\alpha_k(\cdot)$, given by:

$$\boldsymbol{\alpha}_k(\mathbf{g}^{(l)}(\mathbf{s})) = [\boldsymbol{\alpha}_k(\mathbf{g}^{(l)}(\mathbf{s}))]_{\mathbf{s}} \triangleq t_k^2(\mathbf{g}^{(l)}(\mathbf{s})), \quad (4.29)$$

$\boldsymbol{\beta}_k(\cdot, \cdot)$ is the column stack representation of $\beta_k(\cdot, \cdot)$, given by:

$$\begin{aligned} \beta_k(\mathbf{g}^{(l_1)}(\mathbf{s}), \mathbf{g}^{(l_2)}(\mathbf{s})) &= [\boldsymbol{\beta}_k(\mathbf{g}^{(l_1)}(\mathbf{s}), \mathbf{g}^{(l_2)}(\mathbf{s}))]_{\mathbf{s}} \triangleq t_k(\mathbf{g}^{(l_1)}(\mathbf{s})) t_k(\mathbf{g}^{(l_2)}(\mathbf{s})), \\ \beta_k(\mathbf{g}^{(l_1)}(\mathbf{s}), \mathbf{x}^{(l_2)}(\mathbf{s})) &= [\boldsymbol{\beta}_k(\mathbf{g}^{(l_1)}(\mathbf{s}), \mathbf{x}^{(l_2)}(\mathbf{s}))]_{\mathbf{s}} \triangleq t_k(\mathbf{g}^{(l_1)}(\mathbf{s})) t_k(\mathbf{x}^{(l_2)}(\mathbf{s})) \end{aligned} \quad (4.30)$$

and $t_k(\cdot)$ is defined in equations (4.22) and (4.23).

The target subspace \mathcal{B}_k should account for the target signals, the interaction among them, the interaction between them and the background clutter and the interaction between them and the interfering signals. However, this formulation of the target subspace \mathcal{B}_k increases dramatically its dimensionality. We recall that the MSD detection performance is adversely affected by the dimensionality of its target subspace [32, 59]. Therefore, we assume that the interaction among target signals, the interaction between them and the background clutter and the interaction between them and the interfering signals are negligible, searching only for a particular signature under hypothesis H_1 . Hence, subspace \mathcal{B}_k is comprised of:

$$[\boldsymbol{\Lambda}_k^{-1/2} \mathcal{D}_k \boldsymbol{\alpha}_k(\mathbf{h}^{(1)}(\mathbf{s})), \dots, \boldsymbol{\Lambda}_k^{-1/2} \mathcal{D}_k \boldsymbol{\alpha}_k(\mathbf{h}^{(u_h)}(\mathbf{s}))], \quad (4.31)$$

where $\boldsymbol{\alpha}_k(\cdot)$ is defined in equation (4.29). We note that under this formulation of subspaces, scaled image sets can be used for the purpose of characterizing the target and interference signals in spite of the introduced non-linearity that is used in the process of feature space creation.

Based on equation (4.27) and subspace formulations (4.28) and (4.31), we formulate the detection problem as a likelihood ratio test (LRT) between hypotheses H_0

and H_1 . The likelihood ratio (LR) is given by:

$$L_k(\mathbf{v}) \triangleq 2 \log \frac{P(\boldsymbol{\varepsilon}_k(\mathbf{v})|H_1)}{P(\boldsymbol{\varepsilon}_k(\mathbf{v})|H_0)}. \quad (4.32)$$

We assume that the whitened innovations $\boldsymbol{\varepsilon}_k(\mathbf{v})$ follow the 2-D RFM and therefore $\boldsymbol{\varepsilon}_k(\mathbf{v}) \sim \mathcal{N}(\mathbf{0}, \mathbf{I})$. We derive the generalized LR (GLR) from equation (4.32) using the maximum likelihood (ML) estimates of $\boldsymbol{\varepsilon}_k(\mathbf{v})$ under hypotheses H_0 and H_1 . Let $\mathbf{P}_{\mathcal{A}_k}$ and $\mathbf{P}_{\mathcal{A}_k\mathcal{B}_k}$ denote the projection operators onto subspaces $\langle \mathcal{A}_k \rangle$ and $\langle \mathcal{A}_k, \mathcal{B}_k \rangle$ respectively. Subspace $\langle \mathcal{A}_k \rangle$ is spanned by the columns of matrix \mathcal{A}_k and subspace $\langle \mathcal{A}_k, \mathcal{B}_k \rangle$ is spanned by the columns of the concatenated matrix $[\mathcal{A}_k, \mathcal{B}_k]$. The projection operators $\mathbf{P}_{\mathcal{A}_k}$ and $\mathbf{P}_{\mathcal{A}_k\mathcal{B}_k}$ are given by [32, 52]:

$$\begin{aligned} \mathbf{P}_{\mathcal{A}_k} &= [\mathcal{A}_k] \left[[\mathcal{A}_k]^T [\mathcal{A}_k] \right]^{-1} [\mathcal{A}_k]^T, \\ \mathbf{P}_{\mathcal{A}_k\mathcal{B}_k} &= [\mathcal{A}_k, \mathcal{B}_k] \left[[\mathcal{A}_k, \mathcal{B}_k]^T [\mathcal{A}_k, \mathcal{B}_k] \right]^{-1} [\mathcal{A}_k, \mathcal{B}_k]^T. \end{aligned} \quad (4.33)$$

Let $\widehat{\boldsymbol{\varepsilon}}_k^{H_0}(\mathbf{v})$ and $\widehat{\boldsymbol{\varepsilon}}_k^{H_1}(\mathbf{v})$ denote the ML estimates of $\boldsymbol{\varepsilon}_k(\mathbf{v})$ under hypotheses H_0 and H_1 respectively. These estimates are obtained by subtracting the components which lie in the target and interference derived subspaces from the sample vector $\boldsymbol{\gamma}_k(\mathbf{v})$ as follows:

$$\begin{aligned} \widehat{\boldsymbol{\varepsilon}}_k^{H_0}(\mathbf{v}) &= (\mathbf{I} - \mathbf{P}_{\mathcal{A}_k})\boldsymbol{\gamma}_k(\mathbf{v}) \triangleq \mathbf{P}_{\mathcal{A}_k}^\perp \boldsymbol{\gamma}_k(\mathbf{v}), \\ \widehat{\boldsymbol{\varepsilon}}_k^{H_1}(\mathbf{v}) &= (\mathbf{I} - \mathbf{P}_{\mathcal{A}_k\mathcal{B}_k})\boldsymbol{\gamma}_k(\mathbf{v}) \triangleq \mathbf{P}_{\mathcal{A}_k\mathcal{B}_k}^\perp \boldsymbol{\gamma}_k(\mathbf{v}), \end{aligned} \quad (4.34)$$

where \perp denotes the projection operator to the orthogonal complement subspace, *i.e.*, $(\mathbf{P}_{\mathcal{A}_k}\boldsymbol{\gamma}_k(\mathbf{v}))^T (\mathbf{P}_{\mathcal{A}_k}^\perp \boldsymbol{\gamma}_k(\mathbf{v})) = 0$. Based on equations (4.32), (4.33) and (4.34), the k th layer GLR is given by:

$$L_k(\mathbf{v}) = \widehat{\boldsymbol{\varepsilon}}_k^{H_0}(\mathbf{v})^T \widehat{\boldsymbol{\varepsilon}}_k^{H_0}(\mathbf{v}) - \widehat{\boldsymbol{\varepsilon}}_k^{H_1}(\mathbf{v})^T \widehat{\boldsymbol{\varepsilon}}_k^{H_1}(\mathbf{v}) \quad (4.35)$$

and can be regarded as the difference between the Mahalanobis distances under each

hypotheses. We develop equation (4.35) as follows:

$$\begin{aligned}
L_k(\mathbf{v}) &= \|\widehat{\boldsymbol{\varepsilon}}_k^{H_0}(\mathbf{v})\|^2 - \|\widehat{\boldsymbol{\varepsilon}}_k^{H_1}(\mathbf{v})\|^2, \\
&= \boldsymbol{\gamma}_k(\mathbf{v})^T (\mathbf{P}_{\mathcal{A}_k}^\perp - \mathbf{P}_{\mathcal{A}_k\mathcal{B}_k}^\perp) \boldsymbol{\gamma}_k(\mathbf{v}), \\
&= \boldsymbol{\gamma}_k(\mathbf{v})^T (\mathbf{P}_{\mathcal{A}_k\mathcal{B}_k} - \mathbf{P}_{\mathcal{A}_k}) \boldsymbol{\gamma}_k(\mathbf{v}).
\end{aligned} \tag{4.36}$$

We define the MSD's k th layer SNR as the ratio between the energy of the signal which does not lie in the interference subspace and the background innovations covariance in the k th layer. Therefor:

$$\begin{aligned}
\text{SNR}(k, \mathbf{v}) &\triangleq [\mathcal{B}_k \boldsymbol{\psi}_k(\mathbf{v})]^T \mathbf{P}_{\mathcal{A}_k}^\perp [\mathcal{B}_k \boldsymbol{\psi}_k(\mathbf{v})], \\
&= [\mathcal{B}_k \boldsymbol{\psi}_k(\mathbf{v})]^T (\mathbf{I} - \mathbf{P}_{\mathcal{A}_k}) [\mathcal{B}_k \boldsymbol{\psi}_k(\mathbf{v})].
\end{aligned} \tag{4.37}$$

The quadratic form of the k th layer GLR may be thought of as the norm-squared of $(\mathbf{P}_{\mathcal{A}_k\mathcal{B}_k} - \mathbf{P}_{\mathcal{A}_k})\boldsymbol{\gamma}_k(\mathbf{v})$. Therefor, $L_k(\mathbf{v})$ is chi-square distributed with r degrees of freedom [32, 41, 52]:

$$L_k \sim \begin{cases} \chi_r^2(0) & , \text{ under } H_0 \\ \chi_r^2(\text{SNR}(k, \mathbf{v})) & , \text{ under } H_1 \end{cases}, \tag{4.38}$$

where $r = u_h$ and $\text{SNR}(k, \mathbf{v})$ is the non-centrality parameter of the chi-square distribution under hypothesis H_1 . The number of degrees of freedom r is also the rank and trace of the idempotent operator $(\mathbf{P}_{\mathcal{A}_k\mathcal{B}_k} - \mathbf{P}_{\mathcal{A}_k})$ [46].

We define the GLR for image chip $y(\mathbf{v}, \mathbf{s})$, derived using all layers, as follows:

$$\begin{aligned}
L(\mathbf{v}) &= \sum_{k=1}^p L_k(\mathbf{v}), \\
&= \sum_{k=1}^p \boldsymbol{\gamma}_k(\mathbf{v})^T (\mathbf{P}_{\mathcal{A}_k\mathcal{B}_k} - \mathbf{P}_{\mathcal{A}_k}) \boldsymbol{\gamma}_k(\mathbf{v}).
\end{aligned} \tag{4.39}$$

It was previously mentioned that the wavelet coefficients at different layers are nearly de-correlated for most images [31]. Therefor, the GLR is the sum of p independent

chi-square distributions. As such, it is also chi-square distributed with q degrees of freedom as follows:

$$L(\mathbf{v}) \sim \begin{cases} \chi_q^2(0) & , \text{ under } H_0 \\ \chi_q^2 \left(\sum_{k=1}^p \text{SNR}(k, \mathbf{v}) \right) & , \text{ under } H_1 \end{cases}, \quad (4.40)$$

where $q = p \cdot u_h$. The non-centrality parameter of the chi-square distribution is hypotheses dependent; under hypotheses H_0 the parameter equals zero whereas under hypotheses H_1 the parameter equals $\sum_{k=1}^p \text{SNR}(k, \mathbf{v})$. The detection statistic will be maximized when a target is centrally located in the processed image chip.

We define the decision rule for distinguishing between the two hypotheses as a threshold criterion, converting the GLR grayscale image into a binary image. The GLRT is given by:

$$L(\mathbf{v}) \underset{H_0}{\overset{H_1}{\gtrless}} \eta. \quad (4.41)$$

The threshold parameter η determines both the probability of detection P_D and the probability of false alarm P_{FA} . Based on equations (4.40) and (4.41), the detection rate in equation (4.2) is given for each image chip $y(\mathbf{v}, \mathbf{s})$ by:

$$P_D(\mathbf{v}) = 1 - P \left(\chi_q^2 \left(\sum_{k=1}^p \text{SNR}(k, \mathbf{v}) \right) \leq \eta \right). \quad (4.42)$$

The appropriate false alarm is given by:

$$P_{FA}(\mathbf{v}) = 1 - P(\chi_q^2(0) \leq \eta). \quad (4.43)$$

The false alarm rate in equation (4.43) is uniquely defined by the threshold η and the dimensionality q . The detection rate in equation (4.42) is a monotonically increasing function of the GLR non-centrality parameter for a given false alarm rate

and dimensionality q . This is expected since the GLR non-centrality parameter is defined as the sum of the MSD's layers SNR and high SNR values represent a better segregation of the anomalous targets. The detection rate in equation (4.42) is also a monotonically decreasing function of the dimensionality q for a given false alarm rate and MSD's layers SNR values. This is also expected since the dimensionality represents the available *a priori* information about the targets and this information decreases as we increase the rank of the subspace [32]. We note that the detection and false alarm rates cannot be easily found for the general case due to possible statistical dependency between the different layers and inconsistency with the Gaussian assumption. However, the detector performance can be evaluated using extensive computer simulations, as we present in Section 4.5. Since not all layers of the feature space usually contribute the same amount of information to the detection process, it may be beneficial to use only a subset of those layers [39], aiming for the reduction of false alarms and dimensionality. Criterion for selecting the subset of layers is application dependent. This selection can be made *a priori*, thus reducing the computational complexity of the proposed method, or it can be made based on in-process data such as layers with highest average SNR, highest point SNR, *etc.*, in which case the decision can only be made after some calculations have been made. A SNR based criterion is given in Section 4.7. Nevertheless, even when utilizing all layers, the proposed scheme outperforms other recently published algorithms, as we present in Section 4.5.

4.5 Anomaly Detection Experimental Results

In this section we study the performance of the proposed algorithm using a large set of genuine background textures. We first explore the effects of the KLT on the

performance of the proposed algorithm. We then explore the GLR non-centrality parameter of the proposed algorithm, compared to its RDWT equivalent. We investigate the receiver operating characteristics (ROC) curves and the MSD performance of the proposed algorithm, compared to recently published work [22, 55]. Finally, we demonstrate the performance of the proposed algorithm on a set of side scan sonar images.

4.5.1 Performance Analysis

We have qualitatively investigated the performance of the proposed algorithm using synthesized anomalous targets, randomly placed in a set of 40 Brodatz like textures [1]. The synthesized targets were randomly created in a subspace spanned by the image chips in Figure 4.3 and were scaled to achieve desired SNR values. Actual performance statistics were derived using 250 synthesized anomalous targets for each of the 40 Brodatz like textures. No interference subspace is assumed. The background textures were scaled to values within $[0, 1]$ and then normalized to a zero mean, prior to anomaly insertion. We have used the following algorithm parameters:

- A neighbor set concurrent with N_{S7} in [10], given by $\mathcal{R} = \{-\mathcal{R}_h, \mathcal{R}_h\}$, where $\mathcal{R}_h = \{(0, 1), (1, 0), (1, -1), (1, 1), (0, 2), (2, 0), (-2, 1), (2, 1), (1, 2), (-1, 2), (2, 2), (-2, 2), (3, 0), (0, 3), (1, 3), (3, 1), (-1, 3), (-3, 1)\}$.
- An image lattice size of $M \times M$, where $M = 160$.
- A chip size of $N \times N$, where $N = 16$.
- A RDWT decomposition with 2 levels, using the Symlet wavelets with 8 taps.

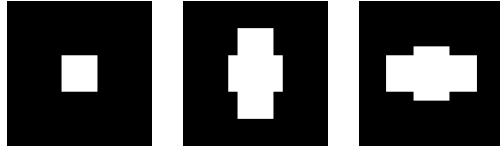


Figure 4.3: Image chips used for the target subspace. Each chip has 16×16 pixels.

The image lattice size and chip size are adequate for assuming $\widehat{\Lambda}_k \simeq \Lambda_k$ when using the maximum likelihood estimator for the innovations covariance [50]. RFM parameters were estimated as described in Section 4.3.3. Anomaly detection was then performed using information from all layers, as detailed in Section 4.4.

We begin by defining the SNR and SNER of a single resolution analysis, providing a reference point for investigating the performance of multi-resolution algorithms. We define the SNR as the ratio between the energy of the anomalous target signal and the energy of the background clutter with respect to the background clutter covariance. Based on equation (4.20), the SNR around the spatial location \mathbf{v} is given by:

$$\text{SNR}(\mathbf{v}) = \|\Gamma^{-1/2}\mathbf{h}(\mathbf{v})\|^2, \quad (4.44)$$

where $\mathbf{h}(\mathbf{v})$ denotes the column stack representation of the target chip $h(\mathbf{v}, \mathbf{s})$ and Γ denotes the background clutter covariance of a background image chip. We define the SNER as the ratio between the energy of the anomalous target signal and the energy of the background clutter. Based on equation (4.20), the SNER around the spatial location \mathbf{v} is given by:

$$\text{SNER}(\mathbf{v}) = \|\mathbf{h}(\mathbf{v})\|^2 / \|\mathbf{x}(\mathbf{v})\|^2, \quad (4.45)$$

where $\mathbf{x}(\mathbf{v})$ denotes the column stack representation of the background chip $x(\mathbf{v}, \mathbf{s})$. Under the framework of synthesized anomalous targets and Brodatz like textures,

using the algorithm parameters as stated above, the resulting averaged SNER value for a given SNR value is: $\text{SNER} \approx \text{SNR} - 26.3$ [dB]. This is the outcome of the correlation between pixels in the background clutter, indicating that the use of a random field model, such as the proposed RFM, is in place. The proposed detection scheme utilizes this spatial information of both anomalous targets and background clutter, further improving the SNR. Therefore, the proposed detection scheme should outperform energy based detectors which ignore available spatial information.

The criterion for choosing the p eigenvectors of the KLT matrix \mathbf{K} and the resulting effects on detection performance is inconclusive in the literature when considering additive anomalies. In [22], it was argued that the use of eigenvectors concurrent with the highest eigenvalues yields better detection results whereas in [8, 54] it was argued that rare anomalous targets reside in eigenvectors concurrent with the lowest eigenvalues. Chang and Chiang have shown in [8] that the RX detector [47] is mainly affected by data associated with smaller eigenvalues. Since both the RX detector and the MSD use a similar Bayesian framework, we have expected similar results. Figure 4.4 shows averaged ROC curves of the proposed algorithm for various KLT configurations and SNR values. We achieved better averaged detection performance using eigenvectors concurrent with the lowest eigenvalues rather than the highest eigenvalues when considering a minimum required value for the detection rate. Furthermore, it is clear that the use of additional layers improves the detection performance. This improvement is due to additional information which is concealed in each layer. The best averaged detection performance was achieved without applying the KLT and when all layers were used. Therefore, we have not used the KLT in the rest of our analysis.

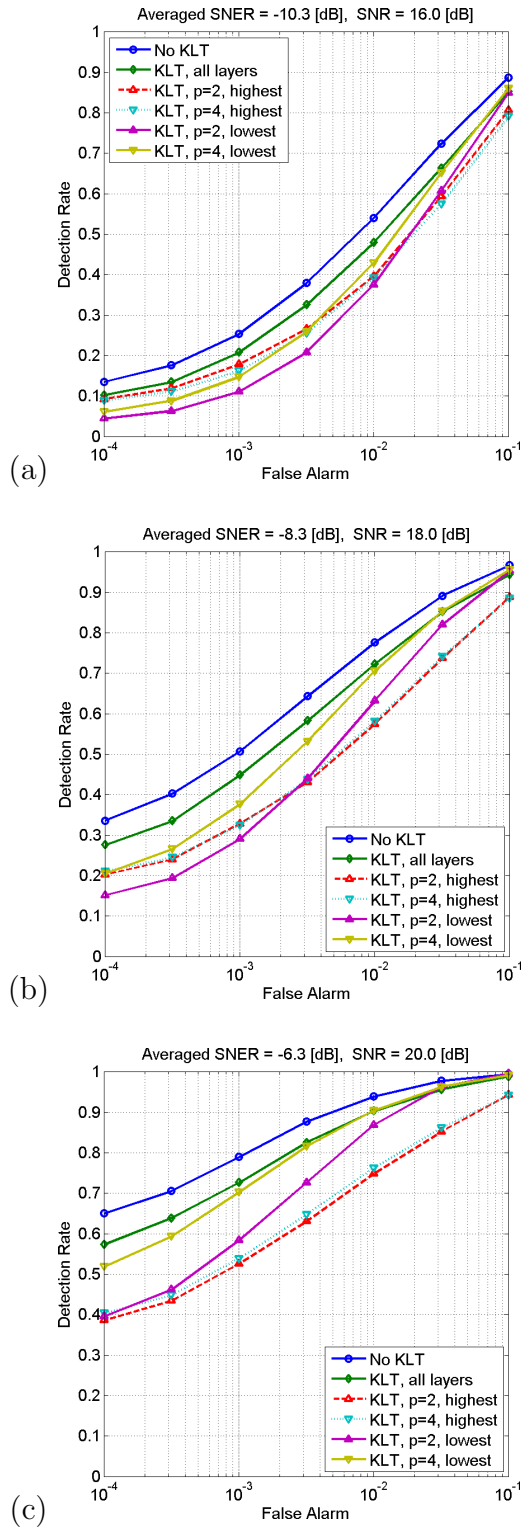


Figure 4.4: ROC curves of the proposed algorithm for various values of p - number of layers after KLT, averaged over a set of 40 Brodatz like textures. Results are given for various SNR values: (a) 16[dB]. (b) 18[dB]. (c) 20[dB].

Theoretical MSD performance is highly affected by the MSD's GLR non-centrality parameter, as can be seen in equation (4.42). Figure 4.5 shows the averaged GLR non-centrality parameter for various SNR values along with the RDWT equivalent of a multi-resolution MSD framework which is employed directly on the RDWT coefficients. We observe that the GLR non-centrality parameter exceeds single resolution analysis SNR values for SNR values larger than approximately 15[dB]. Furthermore, the GLR non-centrality parameter exceeds its RDWT equivalent values for SNR values larger than approximately 22[dB]. Therefore, we could expect for improved detection results whenever a certain minimum SNR threshold is assured. This is demonstrated in Figure 4.6 using theoretical curves for single resolution and multi resolution (MR) analyses. The theoretical curves were calculated using equations (4.42) and (4.43) and the averaged GLR non-centrality parameter values, as given in Figure 4.5. The minimum SNR threshold is both anomaly and background texture dependent. We formulate the desired minimum SNR threshold for each layer in Section 4.7. A layer which contains a dim target signal contributes to the GLR less than a layer with a clear target signal and might even introduce undesired false alarms to the detector. Although this can be resolved by applying a proper threshold to the GLR, the use of such layers affects the robustness of the algorithm. We note that a larger GLR non-centrality parameter is achieved when defining the target subspace to contain interaction between target signals. However, as a result, the target subspace dimensionality is increased from $q = p \cdot u_h$ to $q = p \cdot u_h (u_h - 1) / 2$, degrading the overall achieved performance. Therefore, we have omitted interaction between target signals in the rest of our analysis.

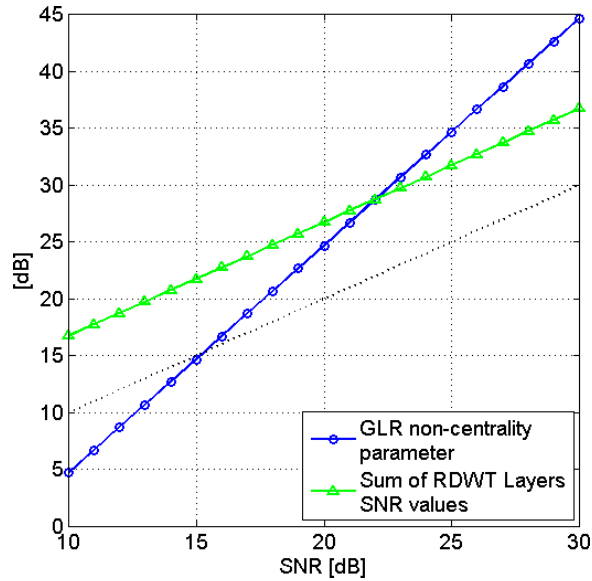


Figure 4.5: GLR non-centrality parameter vs. the sum of RDWT layers SNR values, given for hypothesis H_1 . Results are averaged over a set of 40 Brodatz like textures.

We have tested the performance of the proposed anomaly detection algorithm against two competing algorithms that were recently published in the literature [22, 55]; both have been reported to yield good results. The algorithm in [22] is based on a multi-resolution GMRF and a MSD. The algorithm in [55] is presented in Section 3 and is based on a multi-resolution feature space and single hypothesis testing using the Mahalanobis distance, not utilizing any available information on the target signals. The three algorithms were tested under the same conditions, using the parameters that are described in the beginning of Section 4.5.1. Figure 4.6 shows plots of the averaged probability of detection as a function of the SNR for fixed values of false alarm. Figure 4.7 shows ROC curves for fixed values of SNR. As expected, the detection rate increases with the SNR. The proposed algorithm outperformed the other algorithms, demonstrating an averaged improvement of up to approximately 2[db] when compared to the algorithm presented in [22]. This improvement is crucial in

low SNR environments, as can be seen in Figure 4.8 using the same anomalous target and background clutter from Figure 1.1, but with SNR of 24[dB] rather than 30[dB]. Still, there is a margin between the theoretical detection rate and the experimental results. This margin results from inconsistency between the Gaussian assumption and the actual distribution of the innovations, which exhibits heavier tails. As such, the background innovations should follow an elliptical multivariate t-distribution and the k th layer GLR (equation 4.36) then follows a univariate F-distribution [38]. The resulting GLR (equation 4.39) then follows a mixture of p F-distributions and a new threshold η can be derived to ensure a required false alarm rate. We demonstrate this in Figure 4.9 using the stone texture from Figure 1.1 (a). A possible enhancement for achieving closely Gaussian distributed feature space is the use of a non-stationary local mean [47]. Under this approach, equation (4.16) becomes:

$$z_k(\mathbf{v}) - \mu_{z_k}(\mathbf{v}) = \sum_{\mathbf{r} \in \mathcal{R}} \theta_k(\mathbf{r}) [z_k(\mathbf{v} + \mathbf{r}) - \mu_{z_k}(\mathbf{v} + \mathbf{r})] + \varepsilon_k(\mathbf{v}), \quad (4.46)$$

where:

$$\mu_{z_k}(\mathbf{v}) = \frac{\sum_{\mathbf{r} \in \mathcal{R}_z} z_k(\mathbf{v} + \mathbf{r})}{|\mathcal{R}_z|} \quad (4.47)$$

and the window \mathcal{R}_z is optimized to achieve:

$$E [(z_k(\mathbf{v}) - \mu_{z_k}(\mathbf{v}))^3] = 0. \quad (4.48)$$

However, this approach is useful only when the window \mathcal{R}_z is much larger than the size of the inherent anomalous targets. The margin can also be explained by the use of semi-homogenous genuine textures as a background clutter, which affects the covariance calculation. Nevertheless, the proposed algorithm yields superior detection results, implying that the proposed statistical model better suites the underlying background texture when considering natural textures.

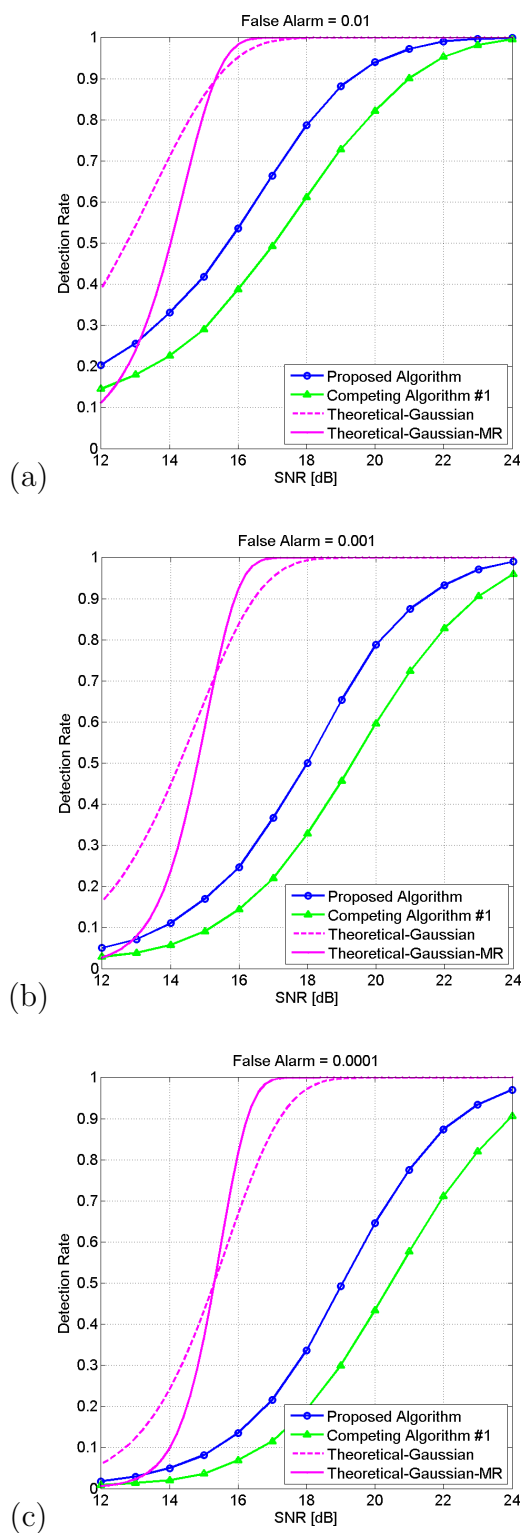


Figure 4.6: MSD performance. Proposed algorithm vs. competing algorithm [22] and theoretical results with equal target subspace dimensionality, averaged over a set of 40 Brodatz like textures. Results are given for various false alarm values: (a) 10^{-2} . (b) 10^{-3} . (c) 10^{-4} .

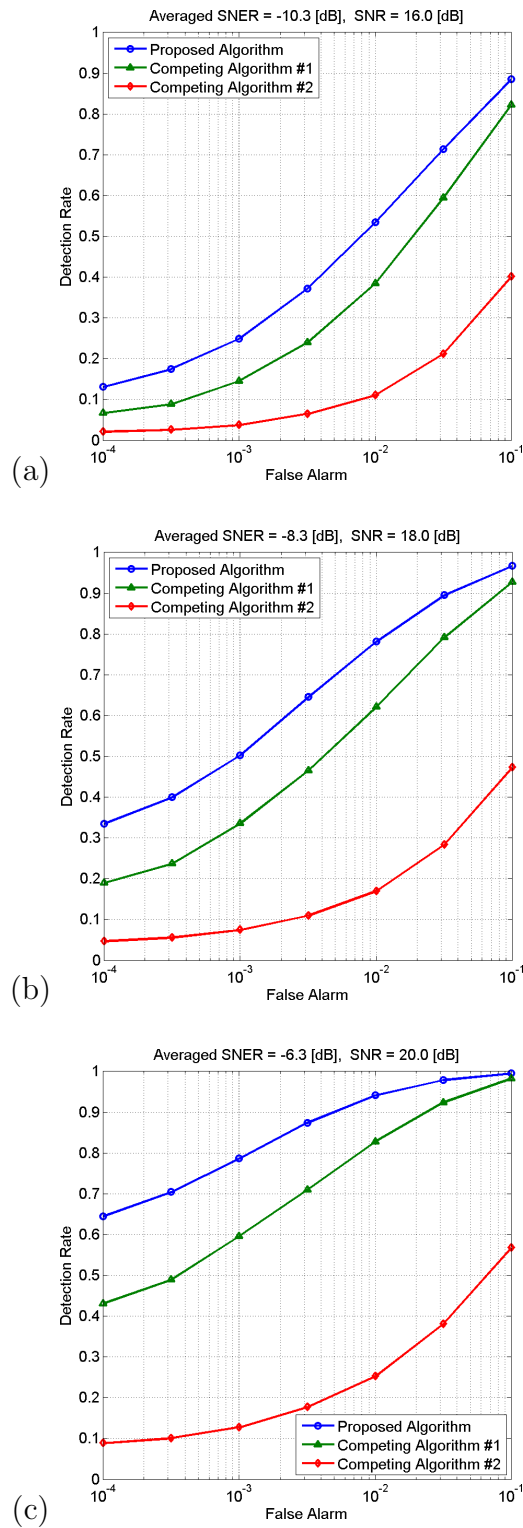


Figure 4.7: ROC curves of the proposed algorithm vs. competing algorithms [22, 55], averaged over a set of 40 Brodatz like textures. Results are given for various SNR values: (a) 16[dB]. (b) 18[dB]. (c) 20[dB].

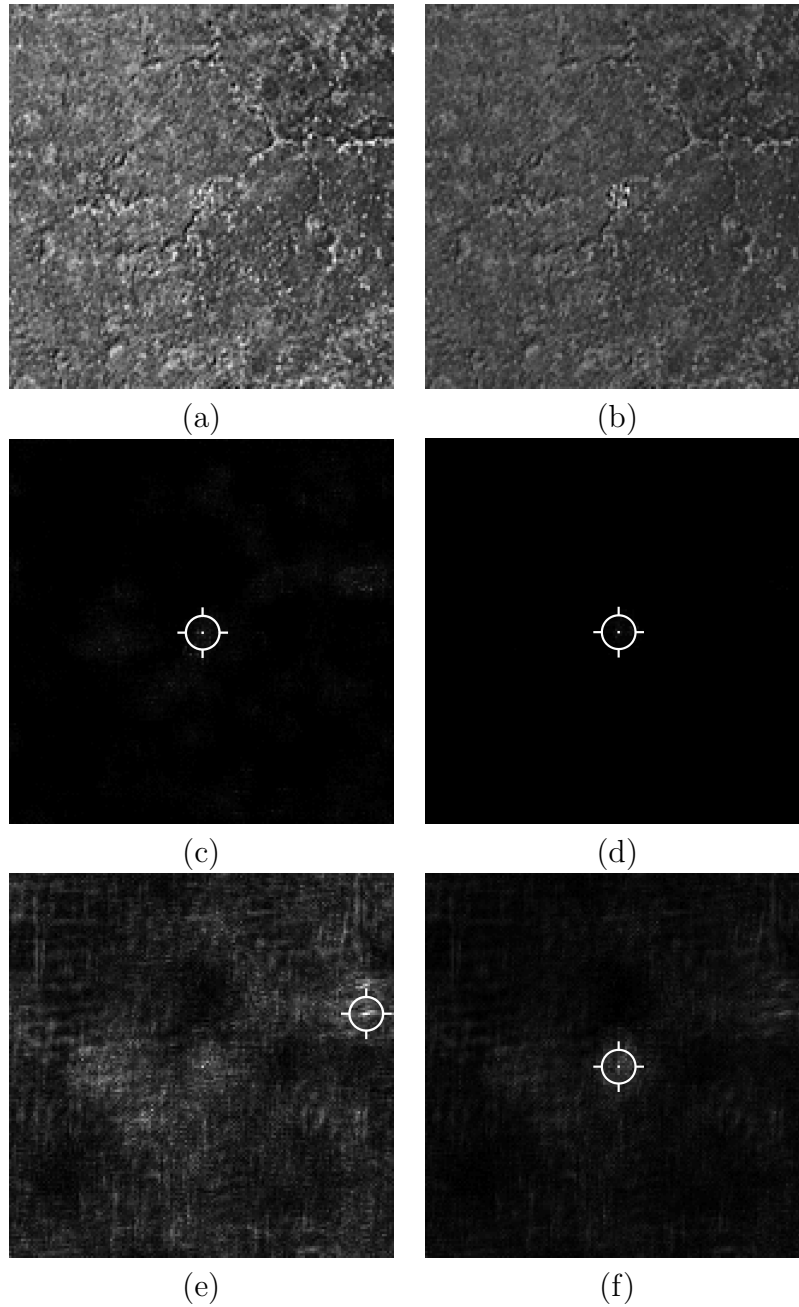


Figure 4.8: An example of detection improvement in low SNER environment using a background natural texture of a stone with an additive squared shaped synthetic anomaly in its center. The synthetic anomaly was created using image chips taken from a texture of metal, not having evident visual resemblance to the stone texture. The anomaly was scaled to achieve: (a) $\text{SNR} = 24[\text{dB}]$. (b) $\text{SNR} = 30[\text{dB}]$. Corresponding anomaly detection results using various methods: (c-d) Proposed algorithm (Section 4). (e-f) Goldman and Cohen [22]. In both methods the detection was performed using a target subspace which was created from the same image chips that were used for synthesizing the anomaly. The white target mark is attached only to the highest value in each detection image.

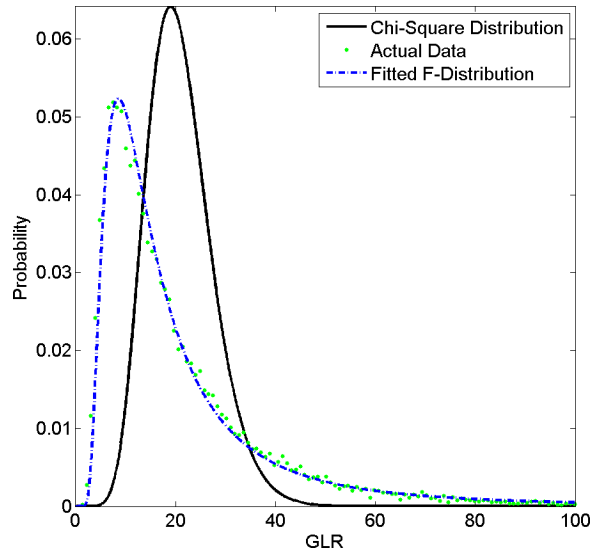


Figure 4.9: GLR distribution example using the stone texture from Figure 1.1-(a).

4.5.2 Anomaly Detection Examples

Side scan sonar is a method of underwater imaging which uses narrow beams of transmitted acoustic energy (sound waves). The reflected sound waves are used for creating a reverberation image. An Object which resides in the path of the sound wave reflects more energy, causing a bright signal in the image. The absence of sound, such as shadows behind objects, appear as dark areas in the image. Goldman and Cohen have demonstrated the robustness and simplicity of their anomaly detection algorithm on side scan sonar images of sea-mines [20,22]. Here, we demonstrate the robustness and simplicity of the proposed algorithm on a set of side scan sonar images containing different types of targets: an airplane, a small boat, a freighter and a tree trunk. No real signature examples are used for defining the target signal subspace. Each image contains one target on a highly cluttered sea-bottom background image. The background patterns are diverse. Figure 4.10 shows the set of side scan sonar images and the detection results, which enhance the visibility of the desired targets. We have

used the same generic subspace for all sonar images. The subspace is presented in Figure 4.11. All the anomalous targets can be detected by applying a proper threshold to the resulting GLR images. The boat in Figure 4.10 (b) is detected without false alarms in spite of the evident background pattern diversity within the image. The freighter in Figure 4.10 (c) is detected with false alarms due to another anomalous target in the image which conforms to the used subspace. These detection results demonstrate the robustness of the proposed model and detection algorithm, allowing for the detection of various anomalies in various background textures using the same set of subspace images, multi-resolution decomposition and neighbor set of pixels.

4.6 Image Scaling for Reduced Prediction Error

Let \mathbf{x} denote a column stack representation of an image with zero mean. Let δ denote a scaling adjustment factor. Let \mathbf{y} denote the scaled image $\mathbf{y} = \delta\mathbf{x}$. Let $\boldsymbol{\theta}_{\mathbf{x}}$ denote the RFM weight coefficients of image \mathbf{x} and $\mathbf{B}(\boldsymbol{\theta}_{\mathbf{x}})$ denote the appropriate RFM matrix. Based on equations (4.6) and (4.9), the RFM innovations are given by:

$$\boldsymbol{\varepsilon}_{\mathbf{y}} = \mathbf{B}(\boldsymbol{\theta}_{\mathbf{x}})\mathbf{y} = \delta\mathbf{B}(\boldsymbol{\theta}_{\mathbf{x}})\mathbf{x} = \delta\boldsymbol{\varepsilon}_{\mathbf{x}}. \quad (4.49)$$

We define $\mathbf{z}_{\mathbf{y}}$ and $\mathbf{z}_{\mathbf{x}}$ as follows:

$$\begin{aligned} [\mathbf{z}_{\mathbf{x}}]_i &= [\mathbf{x}]_i^2 - E[[\mathbf{x}]_i^2], \\ [\mathbf{z}_{\mathbf{y}}]_i &= [\mathbf{y}]_i^2 - E[[\mathbf{y}]_i^2] = \delta^2 [\mathbf{z}_{\mathbf{x}}]_i, \end{aligned} \quad (4.50)$$

where $[\cdot]_i$ denotes the vector element in the i th row.

Let $\boldsymbol{\theta}_{\mathbf{z}_{\mathbf{x}}}$ denote the RFM weight coefficients of image $\mathbf{z}_{\mathbf{x}}$ and $\mathbf{B}(\boldsymbol{\theta}_{\mathbf{z}_{\mathbf{x}}})$ denote the appropriate RFM matrix. Based on equations (4.6), (4.9) and (4.50), the RFM innovations are given by:

$$\boldsymbol{\varepsilon}_{\mathbf{z}_{\mathbf{y}}} = \mathbf{B}(\boldsymbol{\theta}_{\mathbf{z}_{\mathbf{x}}})\mathbf{z}_{\mathbf{y}} = \delta^2\mathbf{B}(\boldsymbol{\theta}_{\mathbf{z}_{\mathbf{x}}})\mathbf{z}_{\mathbf{x}} = \delta^2\boldsymbol{\varepsilon}_{\mathbf{z}_{\mathbf{x}}}. \quad (4.51)$$

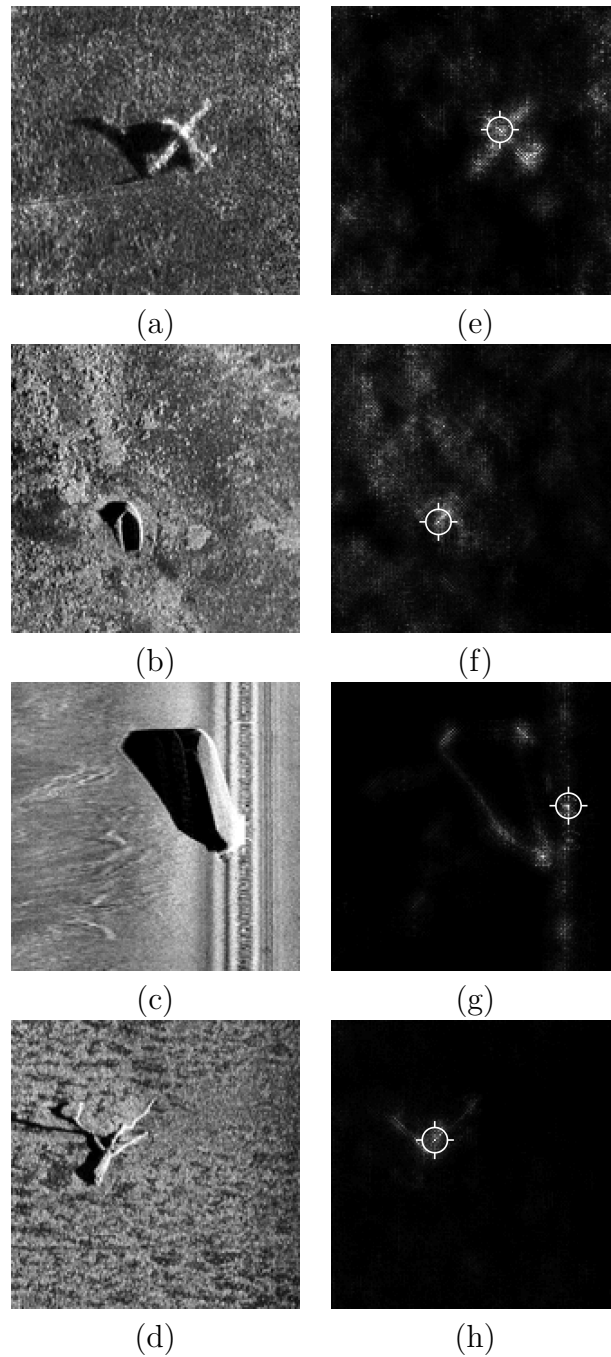


Figure 4.10: Side scan sonar images [2,3] and corresponding anomaly detection results. (a) Cessna airplane. (b) Small boat. (c) The "Isaac M. Scott" freighter. (d) Tree trunk. (e)-(h) Corresponding detection results. The white target mark is attached only to the highest value in each GLR image.

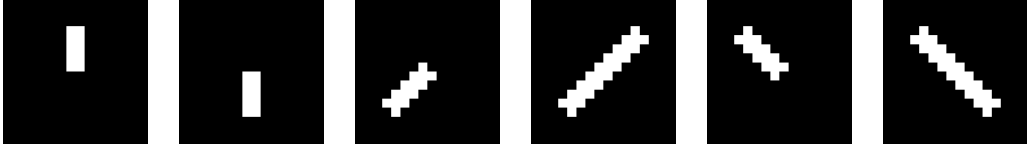


Figure 4.11: Image chips used for the target subspace in the sonar detection examples. Each chip has 16×16 pixels.

The innovations covariances follow:

$$\begin{aligned} \text{cov}[\boldsymbol{\varepsilon}_y] &= \mathbf{B}(\boldsymbol{\theta}_x)\text{cov}[\mathbf{y}]\mathbf{B}(\boldsymbol{\theta}_x)^T = \delta^2\mathbf{B}(\boldsymbol{\theta}_x)\text{cov}[\mathbf{x}]\mathbf{B}(\boldsymbol{\theta}_x)^T = \delta^2\text{cov}[\boldsymbol{\varepsilon}_x], \\ \text{cov}[\boldsymbol{\varepsilon}_{z_y}] &= \mathbf{B}(\boldsymbol{\theta}_{z_x})\text{cov}[\mathbf{z}_y]\mathbf{B}(\boldsymbol{\theta}_{z_x})^T = \delta^4\mathbf{B}(\boldsymbol{\theta}_{z_x})\text{cov}[\mathbf{z}_x]\mathbf{B}(\boldsymbol{\theta}_{z_x})^T = \delta^4\text{cov}[\boldsymbol{\varepsilon}_{z_x}]. \end{aligned} \quad (4.52)$$

In order to achieve smaller prediction error, we require $[\text{cov}[\boldsymbol{\varepsilon}_{z_y}]]_{i,i} \leq [\text{cov}[\boldsymbol{\varepsilon}_y]]_{i,i}$, where $[\cdot]_{i,j}$ denotes the matrix element in the i th row and the j th column. This results in the following requirement:

$$|\delta| \leq \sqrt{\frac{[\text{cov}[\boldsymbol{\varepsilon}_x]]_{i,i}}{[\text{cov}[\boldsymbol{\varepsilon}_{z_x}]]_{i,i}}}. \quad (4.53)$$

Based on equation (4.53), the squaring non-linearity achieves a random field model with lower prediction error variance whenever a proper scaling of the modeled image is performed and the same neighbor set is being used.

4.7 SNR Criterion for Improved Performance

A simple SNR criterion can be applied on each RDWT layer for determining whether or not the proposed algorithm yields improved detection results when compared to a multi-resolution analysis without the introduced squaring non-linearity. The criterion is given for a specific set of anomalous targets and a background clutter. Decomposition layers which do not conform to this criterion might degrade the performance of the proposed algorithm. This allows for an *a priori* selection of layers that shall be

used for computing the GLR. Other anomaly detection algorithms might be employed on the remaining layers, followed by a fusion process of detection results.

Let ψ denote the target subspace coefficients vector. Let ρ denote a SNR adjustment factor. Let \mathcal{A} denote the target subspace in an RDWT layer. Let Σ denote the background clutter covariance in an RDWT layer. The SNR of a target signal vector $\mathbf{y} = \rho(\mathcal{A}\psi)$ in an RDWT layer is then given by:

$$\mathbf{y}^T \Sigma^{-1} \mathbf{y} = \rho^2 (\psi^T \mathcal{A}^T \Sigma^{-1} \mathcal{A} \psi). \quad (4.54)$$

We define subspace \mathcal{B} using the squaring non-linearity such $[\mathcal{B}]_{i,j} = [\mathcal{A}]_{i,j}^2$, where $[\cdot]_{i,j}$ denotes the matrix element in the i th row and the j th column. We define the signal vector \mathbf{z} using the squaring non-linearity such $[\mathbf{z}]_i = [\mathbf{y}]_i^2$, where $[\cdot]_i$ denotes the vector element in the i th row. We define the coefficients vector ϕ using the squaring non-linearity such $[\phi]_i = [\psi]_i^2$, where $[\cdot]_i$ denotes the vector element in the i th row. Therefore:

$$\mathbf{z} = \rho^2 (\mathcal{B}\phi) + \rho^2 (\text{residual}). \quad (4.55)$$

Let \mathcal{D} denote the RFM operator. Let $\boldsymbol{\varepsilon}$ denote the RFM innovations vector. Let Λ denote the background clutter RFM innovations covariance in an RDWT layer. Therefore:

$$\boldsymbol{\varepsilon} = \mathcal{D}\mathbf{z} = \rho^2 (\mathcal{D}\mathcal{B})\phi + \rho^2 \mathcal{D}(\text{residual}). \quad (4.56)$$

The MSD's layer SNR is then given by:

$$(\mathbf{P}_{\mathcal{D}\mathcal{B}} \boldsymbol{\varepsilon})^T \Lambda^{-1} (\mathbf{P}_{\mathcal{D}\mathcal{B}} \boldsymbol{\varepsilon}) \approx \rho^4 \left(\phi^T (\mathcal{D}\mathcal{B})^T \Lambda^{-1} (\mathcal{D}\mathcal{B}) \phi \right), \quad (4.57)$$

where $\mathbf{P}_{\mathcal{D}\mathcal{B}}$ denotes the projection operator into the subspace spanned by the columns

of $[\mathcal{D}\mathcal{B}]$. We define the criterion as follows:

$$\mathbf{y}^T \Sigma^{-1} \mathbf{y} \leq (\mathbf{P}_{\mathcal{D}\mathcal{B}} \boldsymbol{\varepsilon})^T \Lambda^{-1} (\mathbf{P}_{\mathcal{D}\mathcal{B}} \boldsymbol{\varepsilon}). \quad (4.58)$$

The criterion is fulfilled as long as:

$$|\rho| \geq \sqrt{\frac{\boldsymbol{\psi}^T \mathcal{A}^T \Sigma^{-1} \mathcal{A} \boldsymbol{\psi}}{\boldsymbol{\phi}^T (\mathcal{D}\mathcal{B})^T \Lambda^{-1} (\mathcal{D}\mathcal{B}) \boldsymbol{\phi}}}. \quad (4.59)$$

Based on equation (4.59), the proposed algorithm will achieve improved detection results whenever a certain minimum SNR threshold is assured. This threshold is dependent upon the type of anomalous target, the background clutter and the multi-resolution layer.

4.8 Summary

We have introduced a multi-resolution feature space and a corresponding unsupervised anomaly detection method. The proposed feature space is based on a multi-resolution RFM which better describes the background clutter in natural images than other models such as the SAR and the GMRF. The introduced multi-resolution RFM is less susceptible to the choice of neighbors, achieving a smaller prediction error and therefor improved SNR. Our detection method is based on a multi-resolution MSD classifier, achieving improved detection when compared to SHT schemes whenever *a priori* information on the target and interference characterizing subspaces is available. The proposed MSD can incorporate *a priori* information on multi-resolution layers which are most significant to the detection process for reducing false alarms. We have performed extensive testings of the proposed algorithm, using real textures and real and synthesized anomalous targets. The proposed algorithm demonstrates superior performance compared to recently published detection methods.

Chapter 5

Conclusion

5.1 Summary

We have introduced a multi-resolution feature space and a corresponding unsupervised anomaly detection method. The proposed feature space is well modeled by the Gaussian distribution and thus is appropriate for use with Bayesian classifiers. Our detection method is based on the SHT and therefore is not restricted to targets which follow a uniform model or reside in a characterizing subspace. The proposed scheme yields a detection algorithm which achieves improved detection results with CFAR. The proposed scheme can be applied to texture classification, achieving improved classification results. In addition, we have introduced a multi-resolution feature space and a corresponding unsupervised anomaly detection method. The multi-resolution feature space is based on the RDWT and a proposed multi-resolution RFM which better describes the background clutter in natural images than other models such as the SAR and the GMRF. Our detection method is based on an MSD, formulated for detecting subspace targets in multi-resolution RFM innovations. The MSD enables the

incorporation of *a priori* information into the detection process. Mandatory *a priori* information includes the target and interference characterizing subspaces. Optional *a priori* information includes a selection of multi-resolution layers which are most significant to the detection process, thus reducing false alarms. We have presented a comprehensive performance analysis, investigating the influence of different parameters on the detection performance and comparing the performance of the proposed method to those of recently published competing methods. The performance analysis was performed using a large set of genuine background textures. We have demonstrated the robustness of the proposed algorithm when used for automatic target detection in side scan sonar images; a challenging task due to the high variability of targets and sea-bottom sonar representations. The results show the capability of the proposed method to detect a variety of targets in diverse background clutter patterns using the same set of subspace images, multi-resolution decomposition and neighbor set of pixels. A rigorous procedure for defining the target and interference subspaces may improve the detection performance even more, aiming for detecting a specific set of targets. An image with various types of anomalies can be processed using a bank of subspace detectors of the proposed algorithm, each best formulated for detecting a specific anomaly type [59]. The proposed algorithm can be used in conjunction with texture segmentation algorithms, allowing for the detection of anomalous targets in pre-segmented stationary textures in a given scene.

5.2 Future Research

The methods that we have introduced in this work facilitate several topics and applications for future study:

1. The GMRF model has the advantage of providing a direct parametric form of the inverse of the clutter covariance. However, the GMRF model is highly affected by the choice of the neighbor set. To overcome this, Kashyap and Chellapa [26] suggested a Bayesian scheme for selecting the most appropriate neighbor set from a group of neighbor sets, requiring the estimation of model parameters for each set in the process. Yet, their scheme is still limited to the initial group that was used. Future research can address optimal selection of the neighbor set as an inherent part of the RFM model parameters estimation. Possible approach could be the use of a large initial neighbor set along with carefully derived thresholds that determine whether each neighbor in the set is relevant to the model.
2. Hyper-spectral sensor data provides both spatial and spectral features about the targets and backgrounds in sensor imagery [54]. The proposed algorithms can be modified to perform detection using a set of hyper-spectral images rather than a set of multi-resolution layers which are derived from a single image. Another approach can utilize both hyper-spectral images and their multi-resolution decompositions, assuming correlation among the same multi-resolution layers of different hyper-spectral images, utilizing 3-D fields. Future research can focus on the formulation of such algorithms along with a comparative study against recently published anomaly detectors in hyper-spectral sensor data.
3. The multi-resolution Gaussian feature space that was presented in Section 3 can be incorporated into Mittelman & Porat unsupervised segmentation algorithm [37], eliminating the need for using the GMRF in the process. Future research can present a revised segmentation scheme along with performance analysis.

4. A post-classification scheme can be applied on detected anomalies, separating them into different target classes. Such schemes were presented in [8, 11] for classifying anomalies in hyper-spectral imagery. Future research can focus on the usage of these schemes with multi-resolution representation of a single image rather than with the spectral bands of a given scene.

References

- [1] Brodatz like textures.
<http://www-dbv.cs.uni-bonn.de/image/texture.tar.gz>.
- [2] Side scan sonar images.
<http://www.l-3klein.com>.
- [3] Side scan sonar images.
<http://oceanexplorer.noaa.gov>.
- [4] E. A. Ashton. Detection of subpixel anomalies in multispectral infrared imagery using an adaptive bayesian classifier. *IEEE Transactions on Geoscience and Remote Sensing*, 36(2):506–517, March 1998.
- [5] A. Banerji and J. Goutsias. A morphological approach to automatic mine detection problems. *IEEE Transactions on Aerospace and Electronic Systems*, 34(4):1085–1096, October 1998.
- [6] M. G. Bello. A random-field model-based algorithm for anomalous complex image pixel detection. *IEEE Transactions on Image Processing*, 1(2):186–196, April 1992.

-
- [7] F. Berizzi, M. Martorella, G. Bertini, A. Garzelli, F. Nencini, F.D. Acqua, and P. Gamba. Sea sar image analysis by fractal data fusion. In *Proc. IEEE IGARSS*, page 96, September 2004.
- [8] C. I. Chang and S. S. Chiang. Anomaly detection and classification for hyperspectral imagery. *IEEE Transactions on Geoscience and Remote Sensing*, 40(6):1314–1325, June 2002.
- [9] R. Chellappa and R. L. Kashyap. Digital image restoration using spatial interaction models. *IEEE Transactions on Acoustics, Speech and Signal Processing*, ASSP-30(3):461–472, June 1982.
- [10] R. Chellappa and R. L. Kashyap. Texture synthesis using 2-d noncausal autoregressive models. *IEEE Transactions on Acoustics, Speech and Signal Processing*, ASSP-33(1):194–203, Feb. 1985.
- [11] S. S. Chiang and C. I. Chang. Discrimination measures for target classification. In *Proc. IEEE IGARSS*, pages 24–28, Sydney, Australia, July 2001.
- [12] D. A. Clausi and B. Yue. Comparing cooccurrence probabilities and markov random fields for texture analysis of sar sea ice imagery. *IEEE Transactions on Geoscience and Remote Sensing*, 42(1):215–228, Jan. 2004.
- [13] F. S. Cohen, Z. Fan, and M. A. Patel. Classification of rotated and scaled textured images using gaussian markov random field models. *IEEE Transactions on Pattern Analysis and Machine Intelligence*, 13(2):192–202, February 1991.

-
- [14] R. O. Duda, P. E. Heart, and D. G. Stork. *Pattern Classification*. Wiley-Interscience, New York, 2 edition, 2001.
- [15] E. Dura, Z. Yan, L. Xuejun, G. J. Dobeck, and L. Carin. Active learning for detection of mine-like objects in side-scan sonar imagery. *IEEE Journal of Oceanic Engineering*, 30(2):360–371, April 2005.
- [16] K. B. Eom. Long-correlation image models for textures with circular and elliptical correlation structures. *IEEE Transactions on Image Processing*, 10(7):1047–1055, July 2001.
- [17] J. E. Fowler. The redundant discrete wavelet transform and additive noise. *IEEE Signal Processing Letters*, 12(9):629–632, September 2005.
- [18] K. Fukunaga. *Introduction to statistical pattern recognition*. Academic Press, New York, 2 edition, 1990.
- [19] P. Gader, W. H. Lee, and J. N. Wilson. Detecting landmines with ground-penetrating radar using feature-based rules, order statistics, and adaptive whitening. *IEEE Transactions on Geoscience and Remote Sensing*, 42(11):2522–2534, November 2004.
- [20] A. Goldman. Anomaly subspace detection based on a multi-scale markov random field model. Research thesis, Technion - Israel Institute of Technology, August 2004.
- [21] A. Goldman and I. Cohen. Anomaly detection based on an iterative local statistics approach. *Signal Processing*, 84(7):1225–1229, July 2004.

-
- [22] A. Goldman and I. Cohen. Anomaly subspace detection based on a multi-scale markov random field model. *Signal Processing*, 85(3):463–479, March 2005.
- [23] R. M. Gray. Toeplitz and circulant matrices: A review.
- [24] M. Hassner and J. Sklansky. The use of markov random fields as models of textures. *Comput. Graphics Image Proc.*, 12:357–370, Apr 1980.
- [25] G. G. Hazel. Multivariate gaussian mrf for multispectral scene segmentation and anomaly detection. *IEEE Transactions on Geoscience and Remote Sensing*, 38(3):1199–1211, May 2000.
- [26] R. L. Kashyap and R. Chellappa. Estimation and choice of neighbors in spatial-interaction models of images. *IEEE Transactions on Information Theory*, IT-29(1):60–72, January 1983.
- [27] C. Kervrann and F. Heitz. A markov random field model-based approach to unsupervised texture segmentation using local and global spatial statistics. *IEEE Transactions on Image Processing*, 4(6):856 – 862, June 1995.
- [28] S. Kraut, L. L. Scharf, and L. T. McWhorter. Adaptive subspace detectors. *IEEE Transactions on Signal Processing*, 49(1):1–16, Jan. 2001.
- [29] H. Kwon, S. Z. Der, and N. M. Nasrabadi. Adaptive anomaly detection using subspace separation for hyperspectral imagery. *Optical Engineering, Society of Photo-Optical Engineers*, 42(11):3342–3351, November 2003.
- [30] X. Liu and D. Wang. Texture classification using spectral histograms. *IEEE Transactions on Image Processing*, 12(6):661–670, 2003.

-
- [31] S. G. Mallat. A theory for multiresolution signal decomposition: the wavelet representation. *IEEE Transactions on Pattern Analysis and Machine Intelligence*, 11(7):674–693, July 1989.
- [32] D. Manolakis and G. Shaw. Detection algorithms for hyperspectral imaging applications. *IEEE Signal Processing Magazine*, 19(1):29–43, Jan. 2002.
- [33] M. Markou and S. Singh. Novelty detection: a review - part 1 : statistical approaches. *Signal Processing*, 83:2481–2497, July 2003.
- [34] M. Mignotte and C. Collet. Three-class markovian segmentation of high-resolution sonar images. *Computer Vision and Image Understanding*, 76(3):191–204, December 1999.
- [35] R. Mittelman. On multi-resolution statistical models for image processing. Research thesis, Technion - Israel Institute of Technology, August 2005.
- [36] R. Mittelman and M. Porat. A new approach to feature extraction for wavelet-based texture classification. In *ICIP*, pages 1128–1131, September 2005.
- [37] R. Mittelman and M. Porat. A new method for multi-resolution texture segmentation using gaussian markov random fields. In *EUSIPCO*, 2005.
- [38] R. J. Muirhead. *Aspects of Multivariate Statistical Theory*. Wiley, New York, 1982.
- [39] A. Noiboar and I. Cohen. Anomaly detection based on wavelet domain garch random field modeling. *submitted to IEEE Transactions on Geoscience and Remote Sensing*, 2006.

-
- [40] R. Paget, J. Homer, and D. Crisp. (automatic) target detection in synthetic aperture radar imagery via terrain recognition. In *Proc. International Conference on Image Processing*, pages 54–57, October 2001.
- [41] J. K. Patel and C. B. Read. *Handbook of the Normal Distribution*. CRC, 2 edition, 1996.
- [42] B. Porat and B. Friedlander. Performance analysis of a class of transient detection algorithms - a unified framework. *IEEE Transactions on Signal Processing*, 40(10):2536–2546, Oct 1992.
- [43] J. Portilla, V. Strela, M.J. Wainwright, and E.P. Simoncelli. Adaptive wiener denoising using a gaussian scale mixture model in the wavelet domain. In *ICIP*, Thessaloniki, Greece, October 2001.
- [44] J. Portilla, V. Strela, M.J. Wainwright, and E.P. Simoncelli. Image denoising using scale mixtures of gaussians in the wavelet domain. *IEEE Trans. on Image Proc.*, 12(11):1338–1351, 2003.
- [45] T. Randen and J. H. Husoy. Filtering for texture classification: a comparative study. *IEEE Transactions on Pattern Analysis and Machine Intelligence*, 21(4):291–310, April 1999.
- [46] C. R. Rao. *Linear Statistical Inference and Its Applications*. John Wiley and Sons, 2 edition, 1972.
- [47] I. S. Reed and X. Yu. Adaptive multiple-band cfar detection of an optical pattern with unknown spectral distribution. *IEEE Transactions on Acoustics, Speech and Signal Processing*, 38(10):1760–1770, October 1990.

- [48] S. Reed, Y. Petillot, and J. Bell. An automatic approach to the detection and extraction of mine features in sidescan sonar. *IEEE Journal of Oceanic Engineering*, 28(1):90–105, January 2003.
- [49] H. Ren and C. I. Chang. Automatic spectral target recognition in hyperspectral imagery. *IEEE Transactions on Aerospace and Electronic Systems*, 39(4):1232–1249, October 2003.
- [50] C. D. Richmond. Derived pdf of maximum likelihood signal estimator which employs an estimated noise covariance. *IEEE Transactions on Signal Processing*, 44(2):305–315, Feb. 1996.
- [51] A. Sarkar, M. K. Biswas, and K. M. S. Sharma. A simple unsupervised mrf model based image segmentation approach. *IEEE Transactions on Image Processing*, 9(5):801–812, May 2000.
- [52] L. L. Scharf and B. Friedlander. Matched subspace detectors. *IEEE Transactions on Signal Processing*, 42(8):2146–2156, August 1994.
- [53] S. M. Schweizer and J. M. F. Moura. Hyperspectral imagery: clutter adaptation in anomaly detection. *IEEE Transactions on Information Theory*, 46(5):1855–1871, Aug 2000.
- [54] S. M. Schweizer and J. M. F. Moura. Efficient detection in hyperspectral imagery. *IEEE Transactions on Image Processing*, 10(4):584–597, April 2001.
- [55] L. Shadhan and I. Cohen. Detection of anomalies in textures based on multi-resolution features. In *Proc. 24th IEEE Convention of the Electrical and Electronic Engineers in Israel*, Eilat, Israel, 15-17 November 2006.

- [56] O. Smirnov and L. Anselin. Fast maximum likelihood estimation of very large spatial autoregressive models: a characteristic polynomial approach. *Computational Statistics and Data Analysis*, 35:301–319, 2001.
- [57] J. Song, Q. H. Liu, P. Torrione, and L. Collins. Two-dimensional and three-dimensional nufft migration method for landmine detection using ground-penetrating radar. *IEEE Transactions on Geoscience and Remote Sensing*, 44(6):1462–1469, June 2006.
- [58] A. Speis and G. Healey. Feature extraction for texture discrimination via random field models with random spatial interaction. *IEEE Transactions on Image Processing*, 5(4):635–645, April 1996.
- [59] D. W. J. Stein, S. G. Beaven, L. E. Hoff, E. M. Winter, A. P. Schaum, and A. D. Stocker. Anomaly detection from hyperspectral imagery. *IEEE Signal Processing Magazine*, pages 58–69, January 2002.
- [60] V. Strela, J. Portilla, and E. Simoncelli. Image denoising using a local gaussian scale mixture of gaussians in the wavelet domain. In *SPIE*, pages 363–371, 2000.
- [61] R. N. Strickland and H. I. Hahn. Wavelet transform methods for object detection and recovery. *IEEE Transactions on Image Processing*, 6(5):724–735, May 1997.
- [62] P. Torrione and L. Collins. Application of texture feature classification methods to landmine/clutter discrimination in off-lane gpr data. In *Proc. IEEE IGARSS*, pages 1621–1624, September 2004.

-
- [63] P. A. Torrione, C. S. Throckmorton, and L. M. Collins. Performance of an adaptive feature-based processor for a wideband ground penetrating radar system. *IEEE Transactions on Aerospace and Electronic Systems*, 42(2):644–658, April 2006.
- [64] M. Unser. Texture classification and segmentation using wavelet frames. *IEEE Transactions on Image Processing*, 4(11):1549–1560, Nov. 1995.
- [65] M. Unser and M. Eden. Nonlinear operators for improving texture segmentation based on features extracted by spatial filtering. *IEEE Transactions on Systems, Man and Cybernetics*, 20(4):804–815, July-Aug. 1990.
- [66] R. L. De Valois and K. K. De Valois. *Spatial Vision*. Oxford Univ. Press, New York, 1988.
- [67] A. R. Webb. *Statistical Pattern Recognition*. Wiley, West Sussex, U.K., 2 edition, 2002.
- [68] J. W. Woods. Two-dimensional discrete markovian fields. *IEEE Transactions on Information Theory*, IT-18(2):101–109, March 1972.

גילוי אנומליות בתבניות תמונה בהתבסס
על מאפיינים רב-ממדיים

ליאור שדכן

גילוי אנומליות בתבניות תמונה בהתבסס על מאפיינים רב-ממדיים

חיבור על מחקר

לשם מילוי חלקי של הדרישות לקבלת תואר

מגיסטר למדעים

בהנדסת חשמל

ליאור שדכן

הוגש לסנט הטכניון — מכון טכנולוגי לישראל

ינואר 2007

חיפה

שבט תשס"ז

המחקר נעשה בהדרכת פרופ/ח ישראל כהן
בפקולטה להנדסת חשמל

הכרת תודה

אני מבקש להביע את תודתי לפרופ/ח ישראל כהן על הנחייתו המסורה
והדרכתו המקצועית במהלך כל שלבי המחקר.

תודה לבוחני המחקר, דר משה פורת ופרופ' אמיר אורבך, על הערותיהם
והצעותיהם המועילות.

תודה לחבריי לעבודה באלביט מערכות על סבלנותם ותמיכתם.

תודה מיוחדת למשפחתי ולאהבתי קרן על עידודם המתמשך.

אני מודה לטכניון על התמיכה הכספית הנדיבה בהשתלמותי